Charge and energy transport in organic semiconductors

Kimber, Robin

Award date:
2011

Awarding institution:
University of Bath

CHARGE AND ENERGY TRANSPORT IN ORGANIC SEMICONDUCTORS

Robin Geoffrey Edgar Kimber
A thesis submitted for the degree of Doctor of Philosophy
University of Bath
Department of Physics

May 2011

Acknowledgements

My thanks go first and foremost to my supervisor, Alison Walker, for her support, insight and particularly her enthusiasm in finding new projects and collaborations. I am also greatly indebted to both Adrian Hooper and Jess Jones for the IT support they have provided, without which my work would not have been possible. I would like to thank all the members of my research group, and the others who share our office, both past and present, for all their help and for creating a productive and relaxed environment to work in.

All of the work contained herein has been conducted in collaboration with others, all of whom deserve my thanks. Discussions with Chris Groves have been particularly helpful in developing my understanding of Monte Carlo modelling, and his help and ingenuity in evaluating the First Reaction Method has been a great benefit to me as well. The work on triply-periodic bicontinuous morphologies would not have been possible without the input of Gerd Schröder-Turk, who was extremely helpful throughout the project. Finally, my thanks go to James Blakesley, whose work and kind provision of data led to the significant work on quantitative modelling. I would also like to thank Simon O'Kane for the optical modelling he did on my behalf, and Joanna Yorke and Luke McMenemy for producing some particularly stylish morphology plotting tools, used in this thesis.

I will always be indebted to my A-level physics teacher, Mr. Singh, and my Masters supervisor, Bruce Sinclair, for helping build my confidence in my ability to understand physics. I would like to thank my family and all the friends who have helped me get through my studies, especially the other postgraduates at Bath University. Finally, I am incredibly grateful to those who helped get me through the last few months of my studies, particularly my housemates, and especially Elena Gordeeva.

For my parents, Geoff and Gill.

Abstract

This work describes the application of Kinetic Monte Carlo (KMC) modelling technique to organic photovoltaic (OPV) devices. Such devices are an exciting and relatively new form of photovoltaic (PV) technology, which can help bring solar power to the mass market using low energy processing methods, and materials that are cheap, and have several novel characteristics, such as being lightweight, flexible, and potentially even translucent. The modelling technique and many of the results found here are also applicable to other organic devices, such as organic light-emitting displays (OLEDs), as the underlying device physics is very similar.

Following an introduction and discussions on the theoretical basis of the work and its computational implementation, the work described in the thesis falls into three main sections:

Firstly, an evaluation is performed as to the accuracy of the First Reaction Method (FRM), a means of reducing the computational complexity of KMC simulations. Although this method is widely used, its accuracy when used to model OPV devices has never been satisfactorily evaluated, leading it to be questioned by some authors. Hence, its accuracy under a range of scenarios relevant for OPV simulations was tested and quantified. The findings presented here confirm its validity within the field and disorder ranges that are applicable to OPV device operation, and also give some insight into low-field geminate separation dynamics.

Secondly, the KMC methodology, with the FRM approximation, is applied to the investigation of the role of device morphology in determining OPV efficiency. Morphology optimisation has frequently been identified as being key to future device design, and the KMC methodology is unique in its ability to examine this. Furthermore, as the popularity of using self-assembled bicontinuous nanostructures in OPVs grows, it is useful to evaluate their potential impact on OPV efficiency, using the insight gained from investigating morphology in general. Among the main conclusions reached from this work, it was determined that one of the key limiting factors in the efficiency of devices is the

angle of the heterojunctions to the field, which is a feature of the device morphology. It was also found that, because of this, bicontinuous structures are unlikely to greatly improve OPV efficiency.

Thirdly, modelling was performed in an attempt to reproduce the quantitative experimental characteristics of PFB:F8BT devices. This was achieved through first modelling individual charge mobility in the two polymers in question, and quantifying the effects of different forms of disorder. Having found disorder descriptions that could reproduce the single carrier mobility of both PFB and F8BT, as deduced by Blakesley *et. al.* using drift-diffusion modelling, this disorder description was applied to single layer devices, in order to deduce the injection barrier. Finally, the disorder and injection barriers deduced were combined with optical modelling to reproduce full photovoltaic behaviour. This was generally found to be successful, and therefore potentially gives some real insight into the nature of polymer disorder, whilst also validating the KMC model used in this thesis. An additional implication of this work is that the KMC model can, in the future, be applied to experimental data which cannot be satisfactorily modelled using drift-diffusion simulations.

Summary of contents

Contents

Chapter 1

Introduction

1.1 The motivation behind this thesis

The climate and energy motivation

'...there is now strong evidence that significant global warming is occurring. The evidence comes from direct measurements of rising surface air temperatures and subsurface ocean temperatures and from phenomena such as increases in average global sea levels, retreating glaciers, and changes to many physical and biological systems. It is likely that most of the warming in recent decades can be attributed to human activities (IPCC 2001). This warming has already led to changes in the Earth's climate.'

This unprecedented statement was issued jointly by the Royal Society, and the national science academies of France, Russia, Germany, the US, Japan, Italy and Canada, Brazil, China and India on 7th June 2005. Although climate change, and the human participation to it, is a controversial issue, with much uncertainty remaining over the details, there is a clear scientific consensus that it is a very real phenomenon that requires immediate action. Failure to act decisively will prove disastrous for future generations, with climate changes potentially rendering parts of the world uninhabitable, or unable to sustain their present human population. An essential part of this action is to develop forms of energy

that do not contribute to climate change, in order to gradually replace those that do. This is also necessary due to the limited remaining resources of fossil fuels, which are likely to run out during our lifetime [1]. Solar power, including organic photovoltaics, is one of these forms of energy, and is likely to play an increasingly important role in the future. It is hoped that the work contained within this thesis will help contribute to the ongoing development of organic photovoltaics.

The scientific motivation

There is also a purely scientific motivation behind the work contained in this thesis. Optoelectronic devices based on organic semiconducting polymers are an exciting and relatively new area of enquiry, with many possible uses including organic photovoltaics, organic light-emitting devices, organic field-effect transistors (OFETs) and organic lasers. Each of these device types has its own unique advantages over existing inorganic technologies. The development of a greater understanding of the physical processes underlying the operation of organic optoelectronic devices is both fascinating and essential for their continued development. The primal motivation of this thesis is to help develop that understanding through the use of Kinetic Monte Carlo device modelling.

1.2 Solar power

1.2.1 The energy need

In the United Kingdom, the average person consumes 125 kWh of energy per day [1]. Some of this is direct, with the most major contributions coming from residential and business heating and electricity; personal car use; and air flight. Some of it is indirect, such as the provision of public services, defence and the transportation of goods. Using current energy sources, the per capita greenhouse gas emissions of this consumption is equivalent to around 11 tons of CO_2 per year [1]. Although climate science may be complex, the fundamental properties of CO_2 molecules show they scatter infrared radiation, and so atmospheric CO_2 will impede the heat flow away from the surface of the earth into space. Although the atmosphere of the earth has always contained large

amounts of CO_2, in an ongoing cycle with the rest of the earth, it is beyond dispute that post-industrial society has vastly increased atmospheric concentrations of CO_2 from their equilibrium values. Atmospheric data shows an exponential rate of increase in the emissions of CO_2 since 1769 - the year James Watt patented the steam engine. Clearly, therefore, there is a great energy demand, which is usually being met through energy sources which produce CO_2 and/or other greenhouse gases. Alternative energy sources need to be developed that can meet this need, whilst also being free of greenhouse gases (clean), not dependent on finite resources (renewable), and ideally based in this country (secure). Furthermore, transition to new technologies will only become widespread if they can be made to be cost effective.

1.2.2 Solar power as a solution

Solar power has the potential to meet many or all of these requirements. Solar thermal power, which is a simple and efficient technology that directly uses the heat produced by the sun, can reduce the need for other fuels for heating water. Solar photovoltaic cells, which convert sunlight into electrical power, can help meet the demand for electricity. The recent incursion into the mass market of cars that run partly on mains electricity, such as the recently announced Jaguar C-X75 hybrid supercar; and of aeroplanes containing large numbers of photovoltaic cells, notably the Solar Impulse HB-SIA; means that solar power can also help replace the energy sources used in transportation. Solar power has many other advantages over other forms of renewable energy. Photovoltaic cells are almost continuously scalable, from miliwatts to megawatts, powering everything from calculators to data centres. They can be installed almost anywhere, and far from being a blight on the landscape, can be integrated into existing building structures in an aesthetically pleasing way, or by simply utilising wasted space on roofs. They also generate no noise, require minimal maintenance and have no moving parts. These innate features of photovoltaics make them extremely appealing as an energy source. Another advantage of photovoltaics is their usefulness in providing energy to non-grid connected regions, especially in less affluent nations. In isolated areas, where connection to the grid is not usually an option, even expensive PV is usually cheaper than extending the grid by more than 5 km (which accounts for up to 40% of the world's population [2]), as well being cheaper and more environmentally friendly than the batteries and diesel generators with which it would compete as a source of energy.

In the UK, the incident sunlight is around 100 Wm^{-2}, or around 110 Wm^{-2} on a South-facing roof. This is averaged across the year, and factors into account the fact that the Sun only shines for around 34% of daylight hours. There is an average of 10 m^{-2} of roofspace per person [1], so if all of this were covered in 20% efficient photovoltaic cells, running for 10 hours a day, it would generate approximately 2 kWh of electricity per person per day. If these were replaced with 50% efficient solar thermal panels, it would rise to 5 kWh per person. Even if large solar farms were to be built, which would have enormous practical difficulties in this country, solar power alone cannot provide for this country's energy needs. However, it can provide an important contribution, especially in the niche market of portable power generation. Outside the UK, solar power may be particularly beneficial in equatorial regions, due to the greater intensity of sunlight and greater number of daylight hours.

1.2.3 A brief history of photovoltaic technology

The first solid-state photovoltaics used Selenium, initially with platinum electrodes. A major breakthrough came with the work of Fritts, who in 1885 created a photovoltaic cell using a semitransparent gold top layer and an iron base plate, a device that was promoted by Siemens as demonstrating, *'for the first time, the direct conversion of the energy of light into electrical energy'*[1]. Such devices had the essential characteristics of all solar cells - a rectifying junction between two dissimilar electrodes [2]. The nursery of modern photovoltaic devices was the early space age of the 1940s and 50s, particularly in Bell Telephone Laboratories. Silicon-based devices were created by Ohl and later Chapin *et. al.*, who in 1954 demonstrated a 6% efficient cell [3, 4]. At the time the production costs were prohibitively high for widespread use, but the low weight and ability to generate power in remote locations made the technology ideal for satellites.

Over the following few decades, many alternative photovoltaic technologies were developed, driven partly by fears over energy supply, security, and ultimately by climate change. Efficient photovoltaics have been created out of other inorganic semiconductors, such as cadmium telluride, gallium arsenide and indium phosphide. However, crystalline Silicon, usually in the form of single junction wafer-sized cells assembled into large area modules, remains the foremost photovoltaic technology. This is largely because it is

[1]The discovery of photovoltaism is often attributed to Becquerel in 1839, who illuminated platinum electrodes covered in silver chloride, which is, strictly speaking, a photoelectrochemical effect

sourced from the waste of the microelectronics industry, and therefore benefits from advances in that industry which have improved the material quality. However, sourcing Si in this way creates an inevitable supply problem as demand for PV grows. Variations on crystalline Silicon cells that have been developed include polycrystalline and amorphous Silicon. Many thin film devices, sometimes referred to as second-generation photovoltaics, have also been developed, in an effort to reduce weight, cost and to ease the demand on the supply of materials. Tandem cells have also been developed, which improve efficiency by capturing a wider band of the solar spectrum. In the last 20 years or so, PV production has increased much more rapidly, driving down costs by exploiting economies of scale. Following on from the initial driving force of the space industry, PV still has its greatest advantages in niche markets. The most familiar example of this is as by subsidising or replacing battery power in calculators, where PV has had widespread implementation since Sharp's EL-8026 in 1976 [5].

1.2.4 Organic photovoltaic technology

Although organic semiconductor technology has been in development since the 1960s [4], it is only more recently that it has been seen as a viable alternative to the inorganic devices described above. A major milestone was reached in 1986, when Tang, working at the Kodak Research Laboratories in New York, created a two layer organic photovoltaic cell with a power conversion efficiency of about 1% [6]. The following year Tang, working with VanSlyke, also created the first significant organic electroluminescent diode, with a luminous efficiency of 1.5 lmW^{-1} [7]. In that paper it was noted that the device, *'...demonstrates that organic materials can indeed be viable alternatives for optoelectronic applications such as displays'.*

Organic photovoltaic devices have several major advantages over their inorganic counterparts. Firstly, the ability to create the devices at low temperatures significantly reduces the energy requirements of the production process, lowering both the cost and the energy payback time, defined as the operating life needed to reproduce the amount of energy invested during the manufacturing, installation and maintenance of the cells [4]. Secondly, the organic materials on which they are based can be produced relatively cheaply, and can have their electronic properties tuned by modifications to their chemical structure. Finally, such devices are flexible and can be fabricated on lightweight flexible substrates,

creating new and novel applications in consumer electronics. They can also be made to be extremely thin, due to the high extinction coefficients in organic semiconductors compared to Silicon [4]. For instance, they can be used to create lightweight, rollable charging pads, or be integrated into textiles such as backpacks and t-shirts [8]. Demand for this is expected to be partly driven by the rapid growth of portable consumer electronics, such as GPS devices, which would benefit from a power supply to supplement the increasing power demand which battery technology is struggling to keep up with. In terms of aesthetics, a unique advantage of polymer PV is the ability to exploit high transmittance polymers and transparent contacts to create translucent solar cells, tinted with different colours depending on the absorption bands of the polymers used [8].

1.2.5 The present state of photovoltaic technology

The most modern solar cell devices are sometimes referred to as third-generation photovoltaics. Alongside inorganic multijunction cells, these include many organic technologies, most notably dye-sensitised cells; hybrid cells which embed inorganic quantum dots or nanorods into a polymer matrix; and all-organic solid-state polymer cells, notably polymer-fullerene and polymer-polymer blends. The entirety of this thesis concentrates on the modelling of the latter, though the KMC methodology is widely applicable to a variety of other systems. Henceforth, the use of the term 'organic photovoltaic', unless otherwise qualified, should be taken to refer to organic polymer blend photovoltaics.

A typical PV cell will have a surface area of approximately 1 cm^2, an open circuit voltage of less than 1 V and a short-circuit current density of a few tens of mA/cm^2. Therefore, individual cells rarely produce the amount of current and voltage required for real-world applications, and instead are joined together to form modules. The total surface area of of a module is arbitrary, but typically in excess of 800 cm^2 [9]. When joining cells to form modules, parallel connections will scale up the current, and series connections the open-circuit voltage. The power conversion efficiencies of modules are always less than those of individual cells, as modules will be limited by the performance of the least efficient cell within them [10]. The manufacturing process naturally creates variations in both individual cell performance and rate of degradation, which may be worsened by any undetected faults, as well as variations in conditions between cells, such as temperature and level of shading. Furthermore, module efficiencies will also be

limited by the resistance in the inter-cell connections, and any other imperfections in the manufacturing.

Two excellent measures of the current state of photovoltaic efficiencies are the *Progress in Photovoltaics: Solar Cell Efficiency Tables*, published by Wiley [11, 12, 9]; and NREL's *Best Research Cell Efficiencies* charts. Between them, these reveal both the present state and the historical rate of development of photovoltaic efficiencies. Inorganic photovoltaics still have by far the best cell efficiencies, such as 32.0% for a GaInP/GaAs/Ge multijunction device; 27.6% for a thin film GaAs cell and 25.0% for crystalline Silicon. However, although all-organic and dye sensitised cells still have some of the lowest efficiencies of all photovoltaic technologies, they are also two of the most recently invented, and the rate of increase of cell efficiency for all-organic devices is currently higher than most other photovoltaic technologies. As of December 2010, the highest recorded efficiency for an organic solar cell was 8.3 $\pm$ 0.3 % (Konarka), which compares with a best efficiency of only 6% two years ago. The highest performing organic cell submodule at the same time had an efficiency of 3.5 $\pm$ 0.3 %. It is generally thought that lab and commercial module efficiencies of 10% and 5% respectively are required in order for organic PV to become commercially competitive [8], efficiencies which are rapidly being approached. The best cell and module efficiencies for dye-sensitised PVs are currently 10.4% and 9.9% respectively. It is this rapid rate of growth, combined with their other innate advantages that have already been described, that makes organic cells one of the most exciting and promising of PV technologies.

1.3 Thesis structure

This thesis describes the modelling of organic PV devices, with the purpose of developing a greater understanding of the underlying physics, and thus potentially enhancing future device design. Chapter 2 outlines the scientific theory governing charge and energy transport in organic devices, and includes the equations used to describe the transport processes. Chapter 3 explains how this theory is implemented in a Kinetic Monte Carlo model. Chapter 4 sets out to test the validity of the First Reaction Method, an approximation made in many KMC models. Chapter 5 then goes on to use the KMC with the FRM approximation to model photovoltaic devices, and explore the role of morphology in determining device efficiency. A particular feature of this work is the modelling of

novel, bicontinuous structures, and their comparison to disordered blend structures. In Chapter 6, this work is extended to quantitative modelling of devices based on PFB and F8BT, using a hierarchical approach to determine photovoltaic device parameters from the modelling of simpler systems. Finally, Chapter 7 summarises future avenues of research.

Chapter 2

Theory

The purpose of the present chapter is to elicit the scientific principles of charge and energy transport in organic semiconductors, specifically with regard to photovoltaics. The fundamental principles of photovoltaic behaviour will first be described, followed by further detail on charge and energy transport in conjugated polymers, and finally a discussion on the energy levels in the system relevant for device behaviour, and the processes of conversion between excitons and charges at the heterojunction.

2.1 Power conversion in photovoltaics

2.1.1 The fundamentals of photovoltaic operation

Photovoltaics function by converting optical power from the sun into electrical power in an external circuit. The simplest type of photovoltaic is formed by sandwiching a layer of semiconductor in-between two electrodes, one of which must be transparent in order for light to be absorbed by the semiconductor. As with metals and insulators, semiconductors contain a large number of energy levels which electrons can occupy, and are characterised by a forbidden band of energies, called the band gap, which has a width E_g. The band of energy states immediately below the band gap is called the valence band, within which electrons are not able to conduct, due to being tightly bound to

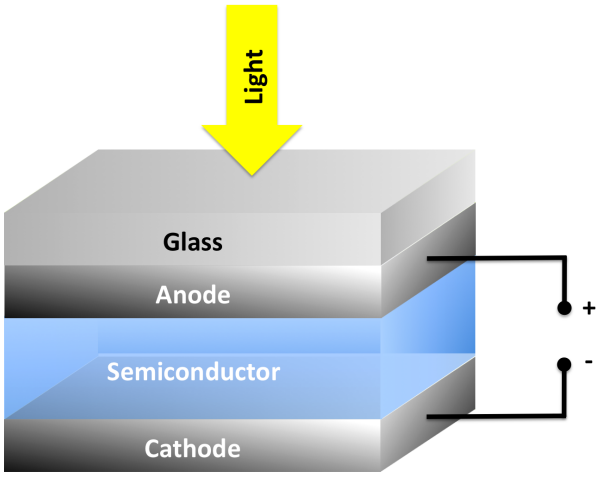

Figure 2.1: Diagram of a simple photovoltaic cell.

their parent atoms. The band of states above the band gap is called the conduction band, within which electrons are able to move, and hence conduct. Energy bands result from the overlap of discrete energy levels from neighbouring atoms. In an intrinsic semiconductor in the dark, the valence band will be full, and the conduction band empty. If a photon is incident with energy $E \geqslant E_g$, it can promote a valence electron into a conduction state, leaving a vacancy in its place. Because valence electrons are able to move in and out of the vacant state, the valence band is effectively conducting this state, just as the conduction band conducts an electron, and as such the vacant state is modelled as a particle called a hole, which has positive charge. Most semiconductors have a bandgap is in the range 1-2 eV, meaning that promotion of an electron to the conduction band can usually be achieved by photons in the IR, visible and UV ranges of the solar spectrum, where sunlight intensity is highest, and also where light emission for optical applications might be desirable. Conventional, inorganic photovoltaics use two layers of semiconductor, forming a p-n junction. In a p-n junction, both layers may be of the same semiconductor type, but one will be doped with foreign donor atoms, and one with acceptor atoms. At room temperature, ionisation of the dopants creates an excess of electrons on one side of the junction, giving it a negative charge; and an excess of holes on the other side, giving it a positive charge. When the two layers are brought together, carrier redistribution near the interface creates a depletion region, which is relatively free of excess carriers, and also leads to built-in potential difference across this region. It is this potential difference that drives excess carriers, created by photon absorption, towards the terminals for collection.

Organic photovoltaics work on many of the same principles, but with a few important differences. Firstly, the n and p-type semiconductor layers are replaced with electron and hole conducting conjugated polymers, or a hole conducting conjugated polymer and an electron conductor, such as fullerene. The organic semiconductors are essentially intrinsic, and not doped with excess carriers as inorganic semiconductors are. And instead of a laminar junction, the polymers will usually be blended together on the nanoscale. Secondly, the absorption of a photon will not lead directly to a free electron and hole, but to an excited state electron-hole pair termed an exciton. This state acts as a single particle with a limited lifetime, during which it will move throughout the polymers. If it reaches an interface between the two polymers during its lifetime, it can dissociate at the electronic heterojunction into its constituent electron and hole, which are then able to be extracted by the electrodes. If not, it will recombine and its energy will be lost from the system as heat. Concomitantly, the nanoscale structure of the device is critical if excitons are to be dissociated within their lifetime, and it is also critical to efficient charge transport. These processes are illustrated in Figure 2.2. Another feature of organic devices is that charges are not transported through broad energy bands, but instead through discrete and disordered molecular orbitals, though still separated by a band gap. Holes are transported in the highest occupied molecular orbital (HOMO) of polymers, and electrons within the lowest unoccupied molecular orbital (LUMO). Finally, the built-in field is not generated by charge distribution across a depletion region, but by the offset in the workfunctions of the electrodes. All of these processes will be examined in more detail presently. First, however, it is essential to outline the general principles that govern the input and output of power in a photovoltaic.

2.1.2 Power input

Incident light

The power density, M, of a light source is defined as the amount of energy passing through unit area in unit time, and as such has units of Wm^{-2}. For a known power density M incident on a solar cell of area A, the incident optical power is then simply $P = MA$.

Monochromatic radiation at a wavelength λ has a photon energy E, where

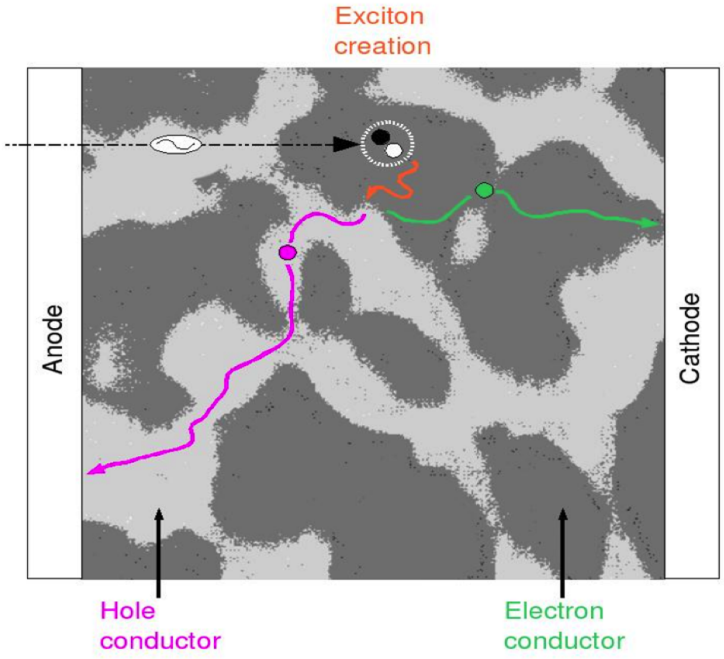

Figure 2.2: Illustration of the working principles of an organic photovoltaic. Photon absorption will create an exciton, which may then migrate to an interface between the electron and hole conductors. Upon reaching an interface, it will dissociate into an electron and a hole, which can then travel through their respective conducting polymers, under the influence of the built-in field, to the electrodes.

$$E = \frac{hc}{\lambda} \tag{2.1}$$

Where h is Planck's constant and c is the speed of light in a vacuum.

The incident flux density of photons, i.e. the number of photons of energy E passing through unit area in unit time, is then $f = \frac{M}{E}$. For example, 460 nm radiation (modelled in Section 6.4) with an intensity of 1 kW m^{-2} has a photon flux of $\approx$ 2313 photons nm^{-2} s^{-1}. In KMC modelling, it is essential to calculate this flux density, as the temporal spacing between photon events is a simulation parameter.

Solar radiation is polychromatic, containing a wide range of wavelengths, each emitted with a different intensity. The extraterrestrial solar spectrum is similar to that of a black body at T = 5760 K, and is strongest in the visible and near-visible wavelengths, 300 -

800 nm. The total power density emitted by a black body of temperature T is given by the Stefan-Boltzmann law,

$$M = \sigma T^4 \tag{2.2}$$

where σ is the Stefan-Boltzmann constant,

$$\sigma = \frac{2\pi^5 k_B^4}{15h^3c^2} = 5.670 \times 10^{-8} W m^{-2} K^{-4} \tag{2.3}$$

k_B being the Boltzmann constant.

Assuming the Sun to be a perfect black body emitter of T = 5760 K, this gives an emitted power density of 62 MW m^{-2}. This is reduced to 1353 Wm^{-2} at a point just outside the Earth's atmosphere [3]. When passing through the atmosphere, gasses scatter much of the incident solar radiation, attenuating the spectrum at wavelengths which are dependent on the particular gas, resulting in Fraunhofer lines (such lines also exist in the extraterrestrial spectrum due to absorption within the Sun). Molecular oxygen, ozone and nitrogen filter out almost all light below $\lambda = 300$ nm (such filtering is essential for life to flourish); H_2O absorbs strongly at 900, 1100, 1400 and 1900 nm; and CO_2 absorbs strongly at 1800 and 2600 nm. The resultant spectrum is characterised by an Air Mass (AMn) factor, where,

$$n = \frac{\text{optical path length to Sun}}{\text{optical path length when Sun is directly overhead}} \tag{2.4}$$

In other words, it is characterised by the amount of atmosphere traversed, of 'standard' thickness and composition. The most commonly used spectrum for evaluating solar cell performance is Air Mass 1.5 (AM 1.5), which corresponds to the Sun being at an elevation of 42° to the horizon. This classifies the extraterrestrial solar spectrum as AM 0. These spectra are plotted, per nanometre of bandwidth, in Figure 2.3 below. Also plotted is the spectrum for a black body at T = 5760 K, from Planck's Radiation Law (Eq. 2.5), which has been reduced by a factor of 4.6 $\times 10^4$, to account for the angular

range of sunlight that reaches the Earth [3].

$$M_\lambda = \frac{2\pi hc^2}{\lambda^5} \frac{1}{\exp \frac{hc}{\lambda k_B T} - 1} \tag{2.5}$$

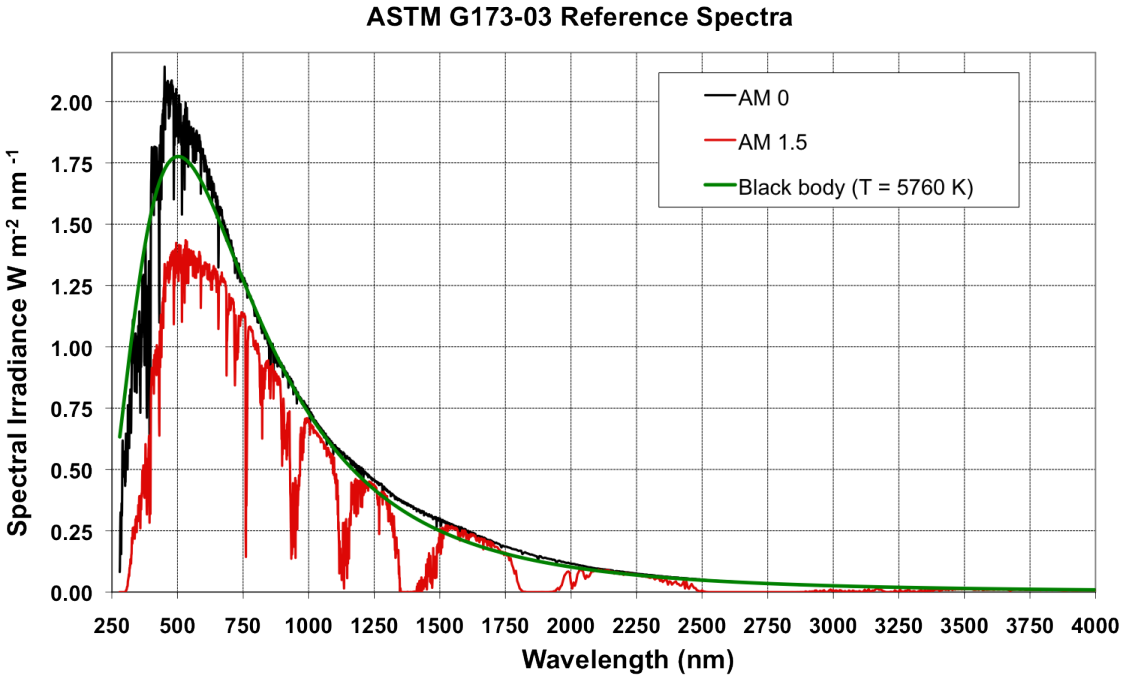

Figure 2.3: American Society for Testing and Materials (ASTM) Terrestrial Reference Spectra (reproduced from [13]), alongside the black body spectrum for T = 5760 K.

The power density of AM 1.5 is defined as being 1 kWm^{-2}, but in actuality the incident light power at the Earth's surface is usually much lower. Global power density, averaged across the year and hence taking into account daily and seasonal variations in elevation of the sun and weather conditions, varies from approximately 100 to 300 Wm^{-2} [3]. The amount of light may be further reduced by the angle of the solar cell to the Sun, which will vary during the day. Solar tracking systems which follow the Sun are sometimes used, but these increase cost, decrease reliability (as the solar cell now has moving parts) and use energy.

For the discrete AM 0 and AM 1.5 spectra, presented in Figure 2.3, the total photon flux density f, can be found simply by summing over the contributions at each wavelength,

f_λ, over the range 280 nm - 4000 nm. The values are $f_{AM0} = 5234$ nm^{-2} s^{-1} and $f_{AM1.5}$ = 3894 nm^{-2} s^{-1}.

Absorbed light

The total amount of the incident light that is usefully absorbed by a photovoltaic will be a function of the thickness of the semiconductor layer(s) between the electrodes (henceforth referred to as the *active layer*), and its absorption spectrum. The absorption spectrum is a complex function of the energy levels within the materials that make up the active layer, particularly the width of the bandgap E_g, and is characterised by various wavelength-dependent optical constants, such as the refractive index, discussed further in Section 6.4.2. The absorption spectrum must be closely matched to the incident spectrum if the cell is to be efficient. For the active layer, the absorbed power density may be expressed as,

$$M_A = \int_0^\infty \eta_A(\lambda) \times f\frac{hc}{\lambda}d\lambda \tag{2.6}$$

Where $\eta_A(\lambda)$ is the fractional absorptance of a given thickness of the active layer at any given wavelength, which is found simply by comparing the incident with the transmitted optical power density at that wavelength. For AM 1.5 radiation incident on a 100 nm thick active layer, consisting of a 1:1 blend of the polymers PFB and F8BT, $M_A \approx 5.8\%$ [14]. This is relatively low, but the PFB:F8BT system is extremely well understood, and as such is ideal for simulation studies, and will be referred to frequently throughout this thesis (further details of this system are given in Section 2.6). Clearly one of the goals of photovoltaic design is to absorb as much of the incident spectrum as possible, and one of the ways to achieve this in polymer blends is to use polymers with complementary absorption spectra.

The total amount of incident light that is absorbed by a photovoltaic cell will not only be a function of the incident and absorption spectra, but also of the physical configuration of the device itself. The device configuration is important because optical interference patterns will form within it, and so the total fraction of incident power that is absorbed, η_A, and the spatial distribution of absorbed power, $Q(x)$, will be a function of the

thicknesses and optical constants of all the layers in the device, including the electrodes and glass layer. Full optical calculations are quite complex, and will be described in Section 6.4.2, with results given for PFB:F8BT systems illuminated at 460 nm.

2.1.3 Power output and efficiency

A photovoltaic will covert the incident light power, quantised as photons, into electrical power, which is quantised as photo-electrons. It operates by doing work on an external load, which will have a resistance, and hence a potential difference across it and a current through it. The ratio of output to input power in a photovoltaic is the **power conversion efficiency (PCE),** η. In the dark, the cell behaves as a diode, and by applying a sufficient bias across the terminals, a dark current will be generated. Applying a reverse bias elicits a much smaller current response, a behavioural feature known as rectifying behaviour. Under illumination, connecting the terminals of a solar cell together (no load resistance) will create a current, termed the **short-circuit current,** I_{SC}, although solar cells are frequently characterised in terms of their **current density,** J, which is the output current divided by the contact area with the electrode, and as such has units of Am^{-2}. The power source that drives the current is the light itself, and it will flow in the opposite direction to the dark current. The voltage across the terminals when they are isolated from each other (infinite load resistance) is termed the **open-circuit voltage** V_{OC}, at which point there is, by definition, no current. At any value of load between these two points, the cell is doing work. The rate at which work is done is the output power, which is equal to the product of the current and the voltage at the operating point, P = IV. When calculated in terms of the current density J, this value becomes the output power density, M = JV.

The performance of a solar cell is characterised by its current-voltage characteristic, i.e. its I-V or J-V response (Figure 2.4). At some point on the J-V curve, the power density delivered to the external load is maximised. This occurs when

$$\frac{d}{dV}VJ(V) = 0 \tag{2.7}$$

The operating point of the cell at which this occurs is termed the **maximum power**

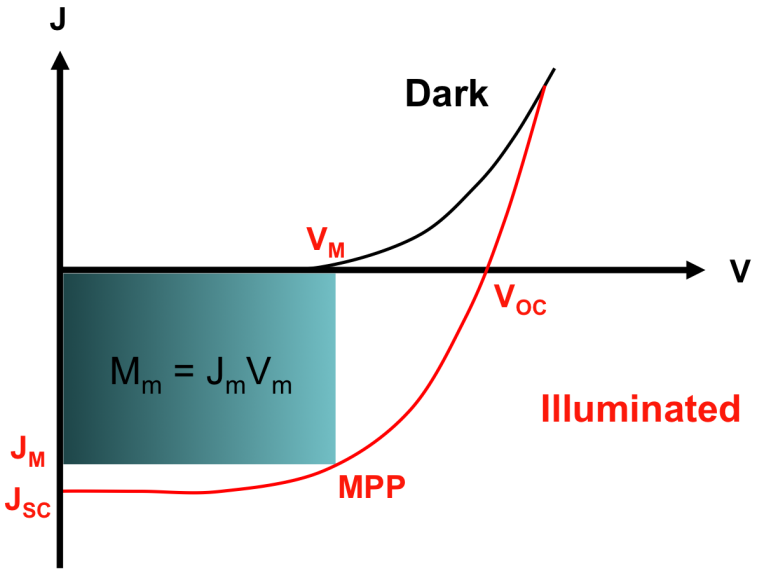

Figure 2.4: J-V characteristics for a simple solar cell, under dark and illuminated conditions. The power density generated at the MPP is equal to the area of the shaded box.

point (MPP), with the current density and voltage at this point denoted J_M and V_M respectively. This leads to a simple definition of the PCE of a cell, in terms of the power delivered density at MPP (M_m), and the incident light power density, M_i:

$$\eta = \frac{M_m}{M_i} \tag{2.8}$$

The shape of the J-V curve is characterised by the **fill factor (FF)**, which is a measure of the 'squareness' of the curve, and is defined as,

$$FF = \frac{J_M V_M}{J_{SC} V_{OC}} \tag{2.9}$$

which leads to an alternative definition of the PCE,

$$\eta = \frac{J_{SC} V_{OC} FF}{M_i} \tag{2.10}$$

At any particular operating voltage, a solar cell converts light into current, and as such a perfect solar cell would extract one charge pair for every incident photon.[1] In practice, efficiency can be lost at multiple stages between the first and final step of power conversion. It has already been shown that not all photons will be absorbed, leading to an absorption efficiency, η_A. Furthermore, in an organic solar cell, charge generation only occurs if the photogenerated exciton reaches an interface during its lifetime, leading to an **exciton dissociation efficiency,** η_{ed}, which will depend on the morphology of the polymer blend. Of the electron-hole pairs that are generated, not all are extracted, the proportion that are being the **charge collection efficiency,** η_{cc}, which will also be morphology dependent. The charge collection efficiency can be further subdivided into the two constituent mechanism by which charge may be lost, geminate and bimolecular recombination. **Geminate recombination** is the process where a dissociated electron-hole pair recombine (see Section 2.6 for further details), and the fraction of charge pairs that are lost in this way is denoted η_{gr} (or alternatively by the geminate separation efficiency, $\eta_{gs} = 1 - \eta_{gr}$). **Bimolecular recombination** is the process where one of the constituent charges of a dissociated electron-hole pair recombines with another charge in the system which is not its original twin. The proportion of dissociated charges that are lost via this mechanism is denoted η_{br}.

These definitions lead to two other measures of solar cell efficiency, the **external quantum efficiency (EQE)**, defined as the proportion of incident photons that lead to extracted charge pairs,

$$EQE = \eta_A \eta_{ed} \eta_{cc} \tag{2.11}$$

and the **internal quantum efficiency (IQE)** is the proportion of absorbed photons that lead to extracted charge pairs,

$$IQE = \eta_{ed} \eta_{cc} \tag{2.12}$$

One of the principle advantages of the Monte Carlo technique over other forms of mod-

[1] This is strictly charge pairs, if the total charge extracted were used, a perfect cell would have an efficiency of 2, which is clearly nonsensical.

elling is that it allows each of the internal processes that contribute to efficiency to be evaluated individually.

Ultimate limiting efficiency

Even with perfect optimisation of the various loss mechanisms in a PV, its power conversion efficiency can still never reach 100%. Instead, photovoltaics will always have a maximum theoretical efficiency, referred to as the ultimate limiting efficiency. Only photons with $E \geqslant E_g$ can be absorbed by a semiconductor, which means that all photons of lower energies will be wasted. Furthermore, the excess energy of any photon above E_g is also wasted (usually as heat). If every photon with $E \geqslant E_g$ is absorbed, and every absorbed photon generates an electron-hole pair that is successfully collected at the electrodes, and the power of every electron is delivered perfectly to the external load, then the efficiency of the device is limited only by its bandgap, E_g, and the incident spectrum. Clearly, if E_g is decreased, then a greater proportion of the incident spectrum will be absorbed, as a greater proportion of the photons will have $E \geqslant E_g$. However, reducing E_g will also reduce the potential energy of the extracted photo-electrons, and so the extracted power density will be reduced. Therefore, for any incident spectrum, there is an optimum value of E_g. Applying the principle of detailed balance, it can be shown that for the AM 1.5 spectrum, this is around 1.4 eV, which produces a power conversion efficiency of around $\eta = 33\%$ [3]. The bandgap of Silicon is 1.1 eV, which has a limiting efficiency of around 29%. Gallium Arsenide and Gallium Phosphide have bandgaps closer to the optimum, of 1.42 eV and 1.35 eV respectively [3]. However, these materials are far rarer and more expensive than Silicon, and material quality does not benefit from the progress of the microelectronics industry. Approximating the AM0 spectrum as that of a black body at T = 5760 K predicts an ultimate limiting efficiency of around 31% at $E_g = 1.3$ eV [15].

2.2 Conjugated polymers

Polymers (from the Greek, meaning 'many parts') are chain-like molecules comprised of repetitions of a unit cell known as a monomer, which are linked by covalent bonds.

In organic polymers, the monomers consist mostly of Carbon atoms. Conjugated polymers are those which contain alternating single and double bonds between neighbouring Carbon atoms. Of the many molecular orbitals in polymers, there are four which are of particular interest here. σ orbitals are parallel to the inter-nuclear axis between neighbouring molecules, in the plane of the polymer chain, also known as the conjugation plane. The electrons in these orbitals, σ electrons, contribute strongly to bonding between adjacent monomers. They are tightly bound, and hence require a large amount of energy to be excited. π orbitals, which result from the overlap of the p orbitals of the constituent Carbon atoms, are perpendicular to the conjugation plane. For both of these orbitals (σ and π), there is an antibonding orbital (σ* and π*). Promotion of an electron from a bonding to an antibonding orbital will weaken the bond, as it raises the energy of the monomer relative to that of the individual atoms [16]. In conjugated polymers, there is a band gap between the filled π orbitals and the unfilled π* orbitals, imparting a semiconducting nature to the system [17]. The most significant states when describing the semiconducting behaviour are the highest occupied molecular orbital (HOMO) in the π-band and the lowest unoccupied molecular orbital (LUMO) in the π*-band.

Overlap of the π orbitals of neighbouring monomers, or through-bond interactions where there is an indirect overlap via an intervening σ framework [18], means that electron wavefunctions can become delocalised over a small length of the polymer chain, allowing an electron to move between monomers. Anything which disrupts the overlap of the relevant orbitals, such as torsional distortion of the chain, will limit the delocalisation range. The result is that charges become localised to small segments of the polymer chain called conjugated segments. Each conjugated segment acts like a quantum well, and hence its length will affect the energy an electron has within it.

Thus the physical disorder of the polymer chain will create a disordered distribution of conjugated segment lengths, and hence an equivalent distribution of electron energy levels between segments. Computation of this disordered energetic distribution is highly complex, and beyond the scope of this thesis. It is also complicated by the fact that the presence of an electron on a chain will further disrupt its structure. However, in general, the recognition that the energy of each electronic state is the result of the combination of a large number of internal coordinates which vary randomly on a small scale means the central limit theorem of statistics holds [19, 20]. The central limit theorem states that the mean of a set of independent random variables will approximate a normal, i.e. Gaussian, distribution. Hence, random fluctuations in conjugation length will create a Gaussian-

distributed disorder in the electronic density of states (DOS). Hulea *et. al.* made use of an electrochemically gated transistor (EGT) to explore the energetics of PPV, and confirmed that the core of the DOS does indeed follow a Gaussian distribution [21]. The energetic disorder, and its origins, as seen by charges is the topic of Section 6.2.

Excitons are also subject to localisation and energetic disorder, although because excitons couple to phonons in different ways to charges, the energetic distribution, and points of localisation will be different. Points of localisation for excitons are termed chromophores, so called because they trap optical excitations. The length of the chromophore is typically 5 to 6 monomers [18, 22]. A localisation radius of typically 10 nm can be expected for singlet excitons in ordered materials [23]. The disruptions in the polymer chain that break the conjugation may be a time-dependent result of interactions between the exciton and nuclear motions, creating a self-trapping effect. Hence, conjugated polymers can be seen as a collection of weakly coupled chromophores with different conjugation lengths, the energy of each being an inverse function of its length [18].

The distribution of chromophore energies within a semiconducting polymer can be experimentally determined using site selective spectroscopy, revealing a Gaussian excitonic absorption band profile [19]. Site selective spectroscopy works by illuminating a sample with monochromatic radiation, creating excitons which will diffuse and eventually radiatively recombine. As the wavelength of an emitted photon is a function of the energy of the chromophore on which the exciton comes to rest (the shorter the chromophore, the higher the energy), the photoluminescence spectrum equates to the distribution of chromophore energies [18]. A similar conclusion can be reached from light absorption spectroscopy, where the spectrum of absorbed light will also be a function of the distribution of chromophore energies, resulting in a Gaussian absorption profile [19] that is blue-shifted compared to the emission profile, due the relaxation of excitons in the DOS prior to emission.

Thus, although the length, and hence energetic distribution of conjugated segments and chromophores will be different, both can reasonably be shown to be Gaussian. For the sake of simplicity, it will be assumed throughout this thesis that both charges and excitons have the same points of localisation and distribution of site energies.

2.3 Energy transport

2.3.1 Photon absorption and exciton formation

Due to the Pauli Exclusion Principal, only two electrons, with antiparallel spins, are allowed to occupy any one energy state. Therefore the total spin (the spin multiplicity) of any filled molecular orbital will be 0 due to the pairing of the electron spins. This is referred to as a singlet state. The absorption of a photon by an electron in a S0 state will promote it from the LUMO to the HOMO, resulting in an excited singlet state S1, a transition which is one-photon allowed [4]. The excited electron in the singlet state can spin flip, creating an excited triplet state T1, where the spins of both the electrons are parallel, creating a total spin of 1. This is highly unlikely to be caused directly by photoexcitation, because spin would not be conserved, as expressed in selection rules. However, it can occur via spin-orbit interaction (inter-system crossing) once the singlet state has been formed. In this case, spin is conserved by interaction with a more deeply bound electron, a process common in rare earth metals. The Pauli Exclusion Principal prevents the excited electron from sharing the same space with its spin-parallel partner in the lower state, reducing coulombic repulsion between the two and giving triplet states lower energy than singlet states [24, 25]. Photon absorption can also form higher singlet states S_n, but collisions with neighbouring molecules will rapidly dissipate the excess energy by momentum transfer, and the state will quickly decay to the lowest excited S1 state [25]. Higher triplet states can be formed by the absorption of another photon by a triplet state [26]. In the semiconducting conjugated polymers used for optoelectronic applications, the dielectric constant is low (typically 3 to 4), with the result that an optically excited electron in the LUMO remains bound to the hole in the HOMO. This coulombically bound excited state is treated as a single quasi-particle, called an exciton. This exciton state is not in thermal equilibrium with its surroundings, and so it will only have a limited lifetime, and in a pure polymer it will eventually recombine, with an accompanied photon emission.

In conjugated polymers, the conjugation length determines absorption and emission characteristics. The ensemble of such chains functions as a mixture of chromophores, broadening absorption and emission spectra. Different chain lengths have different spectra. Evidence of migration between chains can be seen by exciting shorter sequences with short wavelength radiation. The emitted radiation will include longer wavelengths,

and hence emitted from sequences which were not initially excited. As time after initial excitation increases, the emission from other sequences increases, as the result of excitation quenching from the shorter sequences. The longer wavelengths tend not to maintain the polarisation of the exciting radiation, whereas the shorter ones do, suggesting only the short wavelength emissions originate from the original absorbing sites.

2.3.2 Decay and diffusion of excited states

At low temperatures, an excited state can relax via energy transfer to neighbouring chromophores with a lower excitation energy. The excitation of the neighbouring chromophore and de-excitation of the originating one makes it appears at though the excited state has 'hopped', partly justifying why it is modelled as a single particle, the exciton. As the exciton hops to chromophores with progressively lower energy, the mean distance to the next site with a still lower energy will increase , and hence the waiting time for the event to occur will increase. This is termed 'dispersive transport'. Below a threshold energy, the probability of the hop is so low that that it cannot take place during the lifetime of the exciton. Time resolved fluorescence measurements show a time-dependent red-shift in the fluorescence spectrum in accordance with this dispersive relaxation process. At higher temperatures, the possibility of phonon absorption by the exciton can facilitate energetic transfer to states with a higher energy. In either case, intra-chain transfer can also drive excitons towards chain defects which act as quenching sites [22, 27].

The process of exciton transfer involves the de-excitation of the donor chromophore (D), and the excitation of the acceptor chromophore (A). Hence an energy transfer process may be represented by:

$D^* + A \rightarrow D + A^*$

Where (*) indicated an energetically excited state.

This may involve an intermediate photon, known as radiative transfer, or may occur via a virtual transition, when the donor and acceptor interact directly in a radiationless transfer. For the present purposes, it is radiationless transfer which is of interest.

The excited electron and hole form a dipole on the chromophore, though, as with any electron cloud, the location of the electron is smeared out around the chromophore, and so the dipole does not have a fixed orientation. Dipole-dipole interaction mean it can become coupled to other similar chromophores, transferring energy through resonance. The acceptor site becomes excited, and the donor site de-excited, so that the exciton has effectively hopped from one site to the next. This effect was first described quantitatively by Förster, and is usually referred to as Förster Resonance Energy Transfer. It is sometimes referred to as Fluorescence RET when both molecules are fluorescent. However, actually fluorescence does not take place.

2.3.3 Exciton diffusion length

Quantitatively, exciton transport is described by the Miller-Abrahams equation. The rate at which an exciton will hop from the current site, i, to a nearby site j is, [28] [29]

$$w_{ij} = \frac{1}{\tau}\left[\frac{r_f}{r_{ij}}\right]^6 f(E_i, E_j) \tag{2.13}$$

where τ is the exciton lifetime; r_f is the exciton localisation radius (the Förster radius, which is dependent on the spectral overlap of the donor and acceptor chromophores); r_{ij} is the distance between hopping sites i and j, and E_i and E_j are the energies of sites i and j.

$f(E_i, E_j)$ is the energy matching [30] Boltzmann factor, which is only applied to hops upward in energy, denoted 'activated' hops, and thus maintaining detailed balance [28].

$$f(E_i, E_j) = \begin{cases} \exp\left(-\frac{E_j - E_i}{k_B T}\right) & : \quad E_j > E_i \\ 1 & : \quad E_j < E_i \end{cases} \tag{2.14}$$

The accuracy of this simple approach was validated by Athanasopoulos *et. al.* [28], where it was compared to both an analytical model of exciton diffusion and a more exact Monte Carlo model. The more exact MC model used was similar to the one presented

here, but employed transfer rates derived from quantum chemical calculations made for each hop on a realistic chain picture of conjugated polymers. All three models produced similar results over a range of temperatures and disorder levels, and a universal scaling law was discovered between the exciton diffusion length, L_x, and $\hat{\sigma}$ (where $\hat{\sigma} = \frac{\sigma}{k_B T}$, the dimensionless disorder parameter), showing the generality of the results.

The level of detail of the study enabled the calculation of the Förster radius for excitation in conjugated polymers as $r_f = 3.1$ nm, which is also in good agreement with Ref. [31]. Both this value and the value used therin for the exciton lifetime, 500 ps, have been adopted in the work presented here. It was also noted therein that it is essential to include variable range hopping, as restricting exciton hopping to nearest neighbours may force excitons to make energetically unfavourable hops, where hopping to sites outside this range may be more efficient due to reduced energetic barriers. Therefore, both here and in the work presented throughout this thesis, excitons are allowed to hop to sites up to the third nearest neighbour away. This range of 3 nm compares well with the 3.1 nm Förster radius, and is also consistent with the work of Watkins *et. al.* [32].

Testing exciton diffusion modelling

To confirm that the exciton diffusion code written here is accurate, results were compared to the data calculated in [28], which were kindly provided by the author. This was achieved using a simplified version of the KMC model, which models exciton diffusion alone, an analogue to the charge diffusion model described in Section 3.2.3. The model begins with the creation of an exciton at a random location within the lattice, which then hops freely until it recombines. After each hop, a running total of the distance moved in the x, y, and z dimensions is incremented, with periodic boundary conditions applied in all three dimensions. The net distance traversed after n hops is,

$$d = \left[\left(\sum^{n} x \right)^2 + \left(\sum^{n} y \right)^2 + \left(\sum^{n} z \right)^2 \right]^{0.5} \tag{2.15}$$

Over a range of disorder and temperature values, the agreement between this model and the detailed study by Athanasopoulos *et. al.* is greater than 97%, and it most cases

greater than 99%.

2.4 Charge transport

2.4.1 Electron-phonon interactions

Individual charges can enter a polymer photovoltaic either by exciton dissociation or by charge injection from the electrodes. When a charge localises on a particular conjugated segment, its interaction with vibrational modes (quantised as phonons) of the system causes the chain to relax around the charge, and the surrounding chains to also become deformed. The microscopic properties - electronic, optical and transport, of the system are very sensitive to any small displacement of the atoms from their equilibirum positions, and so the presence of the electron changes the properties of the chain on which it lands, an effect referred to as electron-phonon coupling. In organic semiconductors, this coupling is very strong and leads to the formation of quasi-particles, known as polarons. Hence, instead of referring to electron or hole hopping, a more precise nomenclature is to refer to polaron hopping - the movement of both the charge and its associated phonon cloud, which deforms molecules as it arrives and leaves. The induced deformation leads to a polaron binding energy E_p, the amount of energy required for it to be freed from the site it is on. It can therefore be seen as self-trapping.

There are two main rate equations describing polaron hopping in conjugated polymers, derived by Miller and Abrahams [29] and Rudolph A. Marcus [33], respectively. Marcus' vast contribution to the theory of electron transfer reaction was recognised by the awarding of the 1992 Nobel Prize in Chemistry [34]. The Marcus rate results from a full analytical analysis of molecular charge transport, and as such may be considered preferable to the Miller-Abrahams (MA) rate, which is purely empirical, taking no account of the real hopping mechanism at work [14]. However, the MA rate has been highly successful in describing both charge injection and bulk transport. Further details of how these equations have been applied in the work of different research groups can be found in Chapter 6.

2.4.2 Describing polaron transport: the Miller-Abrahams equation

According to the work of Miller and Abrahams, the rate at which a polaron in an energetically disordered landscape will hop from a site i, to a nearby site j is described by [29, 35],

$$k_{ij} = k_0 e^{-2\alpha r} f(E_i, E_j) \tag{2.16}$$

where k_0 the attempt to hop frequency; E_i and E_j are the energies of sites i and j; and r is the distance between them. α is the localisation constant, the inverse of the localisation length of the wavefunction [36, 37], i.e. how much of the polymer chain a charge is localised to. This is not clearly defined, and can be used as a limited range fitting parameter for any system. Scheidler *et. al.* use a value of $1/0.6$ nm $= 1.66$ nm^{-1} [35] and Watkins *et. al.* used $1/0.5$ nm $= 2.0$ nm^{-1} [32]. In the absence of the necessary level of detail in the systems being examined, the same value as Watkins *et. al.* will be used here.

$f(E_i, E_j)$ is the Boltzmann factor:

$$f(E_i, E_j) = \begin{cases} \exp\left(-\frac{E_j - E_i}{k_B T}\right) & : \quad E_j > E_i \\ 1 & : \quad E_j < E_i \end{cases} \tag{2.17}$$

2.4.3 Describing polaron transport: the Marcus equation

The applicable semi-classical version of the Marcus equation is given by [27],

$$k_{ij} = \frac{2\pi}{\hbar} |V_{ij}|^2 \sqrt{\frac{1}{4\pi k_B T \lambda}} \exp\left[-\frac{(\triangle G^0 + \lambda)^2}{4\lambda k_B T}\right] \tag{2.18}$$

(These terms will be defined in Sections 2.4.4 and 2.4.5 below). This expression is factorised into two components: the electronic coupling between states, and the Franck-

Condon factor (FC) due to vibrational coupling between states, so that it can be written as,

$$k_{ij} = \frac{2\pi}{\hbar}|V_{ij}|^2 FC \tag{2.19}$$

A full derivation of this expression and explanation of how the individual parameters are calculated is beyond the scope of this thesis. However, much can be gained by outlining the physical processes which lie behind its constituents.

2.4.4 The electronic coupling

The full electronic coupling matrix element is $|V_{ij}|^2 = |\langle\psi_i|V|\psi_j\rangle|^2$ where ψ_i and ψ_j are the wavefunctions of the two charge localised states (before and after the charge transfer), and V is the electronic Hamiltonian of the system [27]. It is thus related to the spatial overlap of the two atomic orbitals involved in the interaction, which is dependent on site separation, chain angle and chain rotation, and clearly a higher coupling will lead to a higher mobility. The calculation of this value receives much attention in the literature, and the various possible methods are beyond the scope of this thesis. However, as the full chain picture of the polymers is not being modelled anyway, most of the contributions to the electronic coupling which depend on this full chain picture can be taken as constant, allowing a more facile approach to be adopted. As the conjugated segments to which charges are localised are modelled simply as sites on a Cartesian lattice, the only variable aspect of the electronic coupling that needs to be taken into account in the calculation of the hopping rates is the distance between the sites. The simple distance dependency $e^{-2\alpha r}$ in the MA expression can be applied, as its general validity has been confirmed by combining Monte Carlo with quantum chemical calculations on a realistic chain picture [38, 39]. The other (constant) contributions are encompassed in a prefactor in the Marcus hopping rate, which can be calculated using the Einstein-Smoluchowski relation, as described in Section 2.4.6.

2.4.5 The Franck-Condon factor

The FC factor accounts for the physical deformation of the polymer chains that occurs when a charge hops. The expression originates from calculating the rate constant for a system to transfer from one physical configuration into another. It is necessary in electron transfer equations due to the strong electron-phonon coupling, which deforms the conjugated chain segments as electrons arrive and leave. The general FC expression was originally formulated to describe solid state radiationless dynamics, of which dark electron transfer in solution is a specific example, and as such has also been derived independently of electron transfer theories. In general, the potential energy of a system, including both the reacting molecules and the surrounding medium, is the function of many thousands of nuclear coordinates, q, creating an q-dimensional potential energy surface. This can be illustrated using an idealised 1-dimensional profile, representing the energy surface of a system before and after a reaction. In the present context, the reaction is the hopping of a charge carrier from one conjugated segment (which becomes oxidised) to another (which becomes reduced). After the reaction, both the energetic and physical configuration of the system will change. Three such reactions from the reactants (R) to the products ($P_{1,2,3}$) are illustrated in Figure 2.5. For a system to change its state from one configuration to another (reactants to products) two requirements must be met:

- The Franck-Condon principal must be satisfied, which states that electronic changes occur so much more quickly than vibrational ones that the vibrational configuration of a system is effectively 'frozen out' during an electronic transfer. This means that the physical configuration of the system instantaneously before and after the charge transfer must be the same. In terms of Figure 2.5, no horizontal transfers are allowed.
- Energy must also be conserved (transfer must be possible in the dark), meaning that no vertical transitions in Figure 2.5 are allowed either.

Therefore a transition can only occur where the potential energy surfaces of the system before and after the reaction overlap. Otherwise, an electron or hole would find itself in the 'wrong' high-energy environment after the transfer. In other words, the system needs to find a configuration which suits both the before and after states, at which point it has a finite probability of making a transition from one to the other. As can be seen from the

surfaces in Figure 2.5, the energy of the crossover point is not usually at the potential energy minimum of either state. This means that the system must first be disturbed ('de-relax') from its ground state, by receiving an activation energy $\triangle G^*$. This energy is supplied by phonons, making charge transport a thermally activated process, where mobility can increase with temperature. This contrasts with the inorganic case, where elevated temperatures lead to increased scattering of electrons from their trajectories by phonon modes, which reduces the mobility. After the reaction, the system can then relax into its new ground state. The total energy required in moving from one ground state to the next is the sum of the energies required to reorganise all the molecules involved, such as by changing bond lengths and angles, both of the two molecules involved and the surrounding medium (sometimes referred to as the solvent). This is the reorganisation energy λ, which can be expressed as the energy difference between the ground state of the initial system and the energy it would have had if it adopted the ground state configuration of the new system, as can be seen in the diagram. The final energy involved in the reaction is the difference in the potential energy minima before and after the reaction, which is the change in the Gibbs free energy $\triangle G^0$.

The Marcus equation (Eq. 2.18) and Figure 2.5 reveal two distinct hopping regimes. The normal regime is defined as $|\triangle G^0| < \lambda$. Both upward ($\triangle G^0 > 0$, endergonic) and downward ($\triangle G^0 < 0$, exergonic) [40] hops drive the hopping rate, the rate being related to the magnitude of the energy change. By definition, exergonic (from the Greek, meaning 'producing', as they should be able to drive another reaction [16]), reactions should require no driving force and hence be spontaneous. In fact, despite being widely used, this terminology is misleading for the case of charge hopping, as energy is required for any hop, upward or downward, due to the polaron binding energy. For increasingly exergonic hops, the rate initially increases with the magnitude of $\triangle G^0$, but only up to the point where $|\triangle G^0| = \lambda$ (a thermoneutral reaction). Beyond this, hopping enters the Marcus inverted regime, where the hopping rate begins to fall again. This idea is counter-intuitive, but can be seen by consideration of Eq. 2.20 and has been shown experimentally to be correct [40]. Neither downward assisted hops nor the subsequent existence of the inverted regime are included the the M-A equation, another reason why the Marcus rate is a preferable means of modelling these processes.

It was shown by Marcus that the three energies involved in the reaction, $\triangle G^0$, $\triangle G^*$ and λ, are related by,

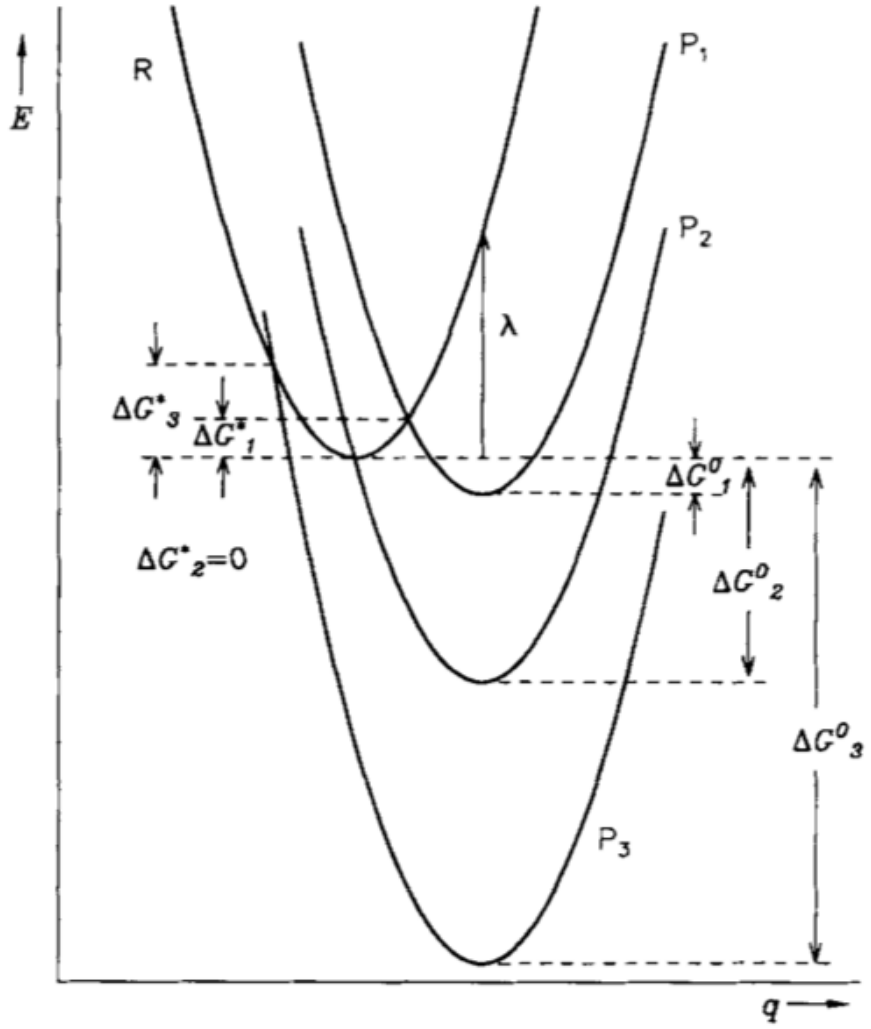

Figure 2.5: The potential energies E of the reactants (R) and the products (P_1-P_3) of three systems with different free energies of reaction $\triangle G^0$, as a function of the nuclear configuration q. 1: Exergonic reaction with $|\triangle G_1^0| > 0$ and $\triangle G_1^* > 0$; 2: exergonic reaction with $|\triangle G_2^0| = \lambda$ and $\triangle G_2^* = 0$; 3: $|\triangle G_3^0| > \lambda$ and $\triangle G_3^* > 0$ (Marcus inverted region) (reproduced from [40]).

$$\triangle G^* = \frac{\lambda}{4}\left(1 + \frac{\triangle G^0}{\lambda}\right) \tag{2.20}$$

so that only two are required in the final expression. The value of λ encompasses the relaxation energies of the two conjugated segments involved, and the relaxation of the

surrounding medium. Here, it is taken as a constant for transitions within the same polymer, and a value of $\lambda = 1.2 \times 10^{-19}$ J [41] has been adopted in the work presented in this thesis. It can be shown [38] that $\lambda = 2E_p$, where E_p is the polaron binding energy referred to earlier. Further discussion of reorganisation and relaxation energies, and how they are calculated, is beyond the scope of this thesis, as this is not being considered, as λ is taken as constant throughout. This means the only variable in the FC factor for a fixed temperature is the variation of $\triangle G^0$.

The distribution of $\triangle G^0$ is the disordered energetic landscape referred to earlier, and is modelled as static disorder, with individual conjugated segments being assigned an energy reflecting the change in $\triangle G^0$ for the system when an electron or hole becomes localised there. The static disorder of the system has two contributions: diagonal (in matrix representation where $m = n$) and off-diagonal ($m \neq n$). Off-diagonal disorder reflects variations in the strength of interaction between molecules, such as dynamic nonlocal electron-phonon coupling or static variations in inter-site coupling due to position and/or orientation. Diagonal disorder refers to disorder in individual sites, not their relationship with other sites, such as dynamical local electron-phonon coupling, and static energetic variations (due to a distribution of effective conjugation lengths) in site energies. Diagonal terms can be defined for a site without reference to other sites, whereas off-diagonal terms can only be defined by examining the relationship between sites. Off-diagonal static disorder encompasses variations in chain spacing and orientation, which will affect their transfer rate to other chains. To accurately take this into account in the modelled hopping rates, it would be necessary to first create and then simulate realistic morphologies, both of which are extremely computationally intensive procedures. However, the size of any morphology simulated should be sufficient to average out off-diagonal terms, so that their exclusion should have little effect on the overall hopping rates, expressed as current or mobility. All KMC device models have proceeded along these lines, without compromising the accuracy of results. The nature of the distribution of G^0 values, henceforth referred to simply as the energetic disorder of the system, and how this affects charge transport, is the subject of Section 6.2.

2.4.6 Applying charge transport: Mobility

Regardless of the microscopic mechanism of charge transport, in a semiconductor the presence of a field (F) will cause the charges to drift, with a net direction of motion, and hence a net velocity (v). The mobility (μ) of the charges can be defined very simply as the ratio of the net velocity to the electric field. As the velocity can be calculated by the displacement (d) over time (t) and the field can be simply defined as the voltage (V) dropped over that displacement, the mobility can be written in various forms, such as [38, 42],

$$\mu = \frac{v}{F} = \frac{d}{tF} = \frac{d^2}{Vt}, \tag{2.21}$$

giving it the units of $\mathrm{m}^2(\mathrm{Vs})^{-1}$.

In inorganic devices, the mobility is a constant relating the field across the device to the mean drift velocity of the charges (in the case of electrons, the direction of the drift will be antiparallel to the field vector). In organic devices, the presence of a field lowers the potential barriers between the conjugated segments, creating a field dependency of the mobility. The origin and quantitative nature of mobility in organic semiconductors will be elucidated further in Chapter 6. This definition of mobility is useful in its direct calculation, such as by experimental time of flight (TOF) method, or by Monte Carlo modelling, as outlined in Section 3.2.3.

Alternatively, the mobility may be defined as follows. If charge transport is considered to be purely diffusive, it can be described by a simple diffusion equation,

$$\langle x^2 \rangle = nDt \tag{2.22}$$

where $\langle x^2 \rangle$ is the mean square displacement; n is an integer value of 2, 4 or 6 depending on whether the motion is in 1, 2 or 3 dimensions; D is the diffusion coefficient, and t is the time. The mobility is related to the diffusion coefficient by the Einstein-Smoluchowski relation [38, 43],

$$\mu = \frac{eD}{k_B T} \tag{2.23}$$

Where e is the electron charge. This definition is essential to calculating the correct prefactor for both the Marcus and Miller-Abrahams rate equations, a topic raised in Section 2.4.4. Taking $n = 6$ and assuming nearest neighbour hopping with a lattice constant a, the hopping rate k is,

$$k = \frac{6D}{a^2} = \frac{6\mu k_B T}{ea^2} \tag{2.24}$$

For a given combination of μ, T and a, the hopping rate k for charges moving between isoenergetic localisation sites can then be calculated. The prefactor for the Marcus equation can now be found as follows. Writing Eq. 2.18 as,

$$k_{ij} = \nu e^{-2\alpha r} \exp\left[-\frac{(E_j - E_i + \lambda)^2}{4\lambda k_B T}\right] \tag{2.25}$$

By setting $E_i = E_j = 0$ (for purely diffusive transport), and setting $r = a$ (for nearest neighbour hopping) equations 2.24 and 2.25 can be equated to find the prefactor, ν,

$$\nu = \frac{6\mu k_B T}{ea^2} e^{2\alpha a} \exp\left[\frac{\lambda}{4k_B T}\right] \tag{2.26}$$

A similar procedure can be followed for the MA equation.

2.5 Energy levels in the system

In metals, electrons fill up the energy levels from the ground state upwards, obeying the Pauli Exclusion Principle, up to an energy defined as the Fermi energy E_F. Metals are characterised by high electrical and thermal conductivity, due to the abundance of

conduction electrons - those that are free to move about and are not bound to their parent atoms. This scenario is sometimes referred to as a 'Fermi sea' of atoms. The work function, ϕ_W, of a metal is defined as the difference in energy between the Fermi level and the vacuum level. In a semiconductor, the Fermi level is defined as that where the probability of occupation by an electron is exactly 0.5, and is also the highest occupied energy at absolute zero temperature. Consequently, the position of E_F in a semiconductor will depend on both doping and the carrier concentrations (which will vary with operating conditions), shifting it to a point known as the quasi-Fermi level. As the energies of the conduction and valence bands are important in describing semiconductor behaviour, two more terms are defined. These are the electron affinity, χ, which is the difference in energy between the bottom of the conduction band and the vacuum level; and the ionisation potential, ϕ_I, which is the difference in energy between the top of the valence band and the vacuum level. In organic semiconductors, these definitions are applied with respect to the LUMO and HOMO levels, respectively. Any difference between the energy of the LUMO/HOMO levels and the Fermi level in the injecting cathode/anode is called the injection or Schottky barrier, ϕ_B. This barrier limits charge injection, as charges will have to overcome it by thermionic emission and/or tunnelling.

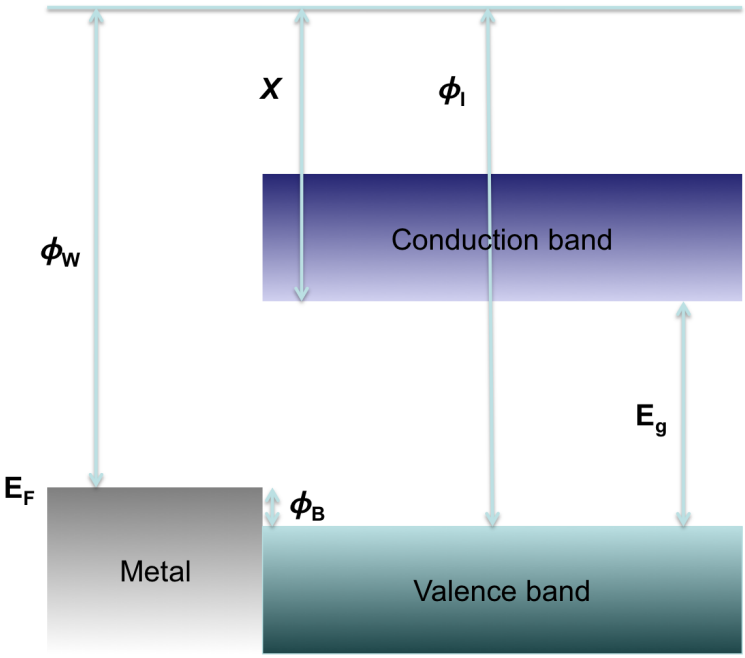

Figure 2.6: Primary energy levels in a metal-semiconductor junction.

When a metal/polymer/polymer/metal system is brought together, i.e. the short-circuit

operating point, the Fermi levels of the electrodes must align with each other. One of the electrodes will become polarised with respect to the other, shifting the workfunction, with the result that the rest of the energy bands in the system will bend in order to accommodate the change. This band bending is constrained by the fact that the Schottky barriers remain constant, due to pinning of the HOMO/LUMO level by the cathode/anode; and that the HOMO/HOMO and LUMO/LUMO offsets (referred to as the band edge offsets) must remain constant. The resultant field across the device, which is the 'built-in field' discussed earlier, will have a magnitude equal to the initial work function offset of the electrodes, divided by the thickness of the polymer layer between them. The energy levels in this scenario are illustrated in Figure 2.7 (a). By either placing a load, or applying a field, across the system, the electrode polarisation can be reduced, reducing the built-in field. Ultimately, the open-circuit regime will be reached, where the energy levels return to those before the system was joined, as shown in Figure 2.7 (b). Applying a stronger field can move the system into forward bias, where current injection will occur, shown in Figure 2.7 (c).

The electrodes used for organic electronics devices are chosen such that the Fermi levels are well aligned to the transport levels in the polymers, i.e. to minimise or eliminate the injection barrier. Thus, electrons and holes can flow relatively easily across the metal/semiconductor junction. Electron or hole only devices (EOD / HOD) can be achieved by creating a deliberate mismatch between the transport levels such that the injection barrier is prohibitively high for one of the carrier types. However, the rate of charge extraction is independent of barrier height, as the Fermi level in the extracting electrode is always below the relevant transport level in the semiconductor [44]. A contact where the is no injection barrier is referred to as an Ohmic contact. Ohmic behaviour has frequently been seen in experiment [45]. Specific examples of near-Ohmic behaviour in an electrical contact with, for example, MEH-PPV, include the insertion of a LiF between an aluminium electrode and the organic layer [44]; using a CsF layer with aluminium, the use of a Cs layer (which enhances injection regardless of the metal) [46]; or the simple use of Ca contact [47]. As can be seen from Figures 2.7 (a) and (c), the same electrode that collects a particular charge type at short-circuit for photovoltaic operation will inject the same charge type at forward bias conditions. For electrons and holes, these are defined as the cathode and anode respectively.

Alongside the net field within the organic layer, and the injection barrier, a third constituent is required to fully describe the bandstructure at the electrode. Each charge

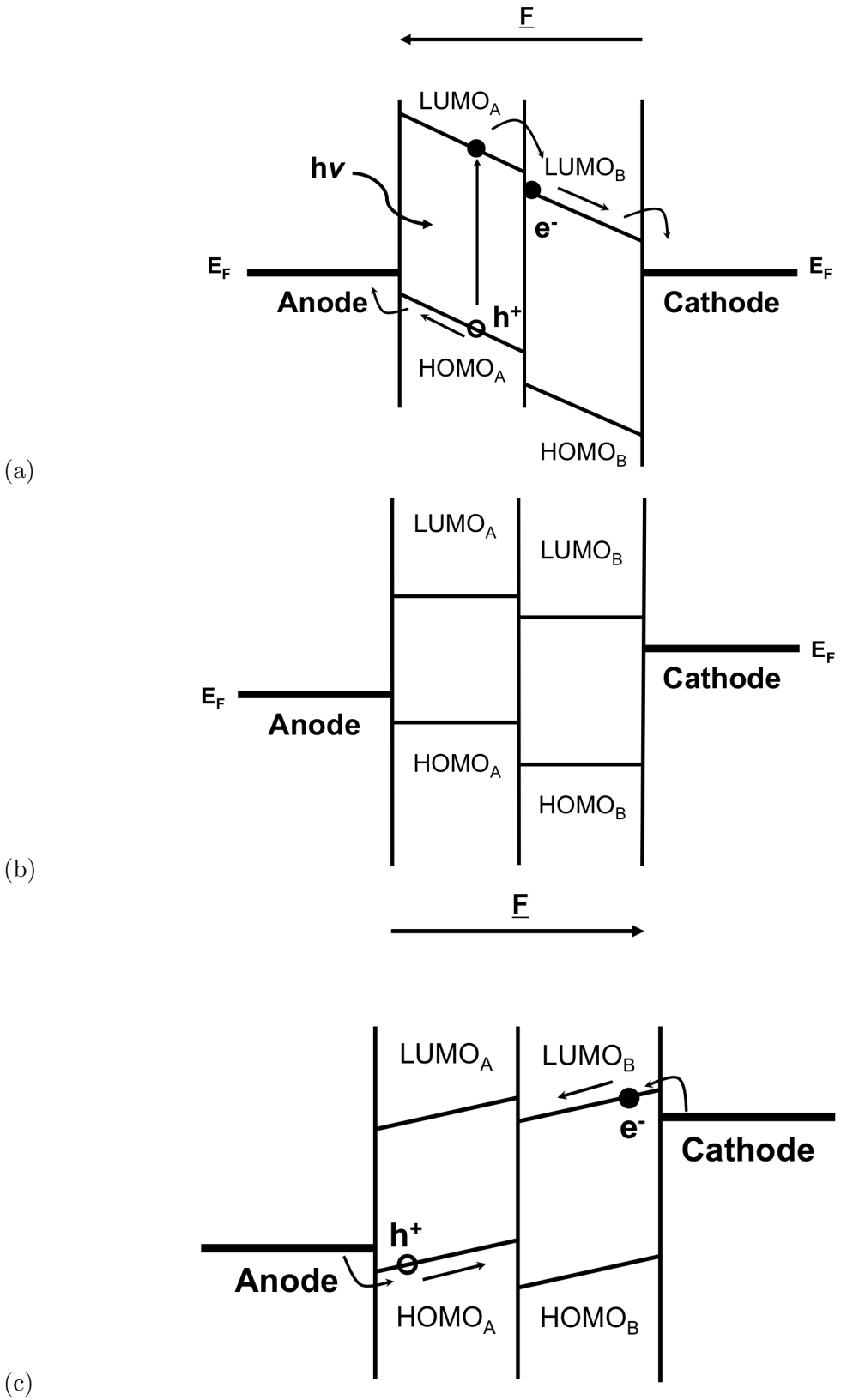

Figure 2.7: Organic photovoltaic bandstructure, for two polymers (A and B), at (a) short-circuit; (b) open-circuit and (c) forward bias conditions.

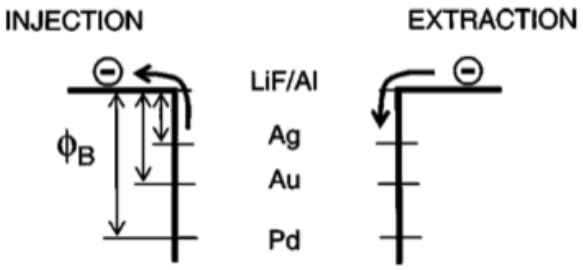

Figure 2.8: Schematic energy diagram of an interface between an organic and different top electrodes. The extraction current is independent of the work- function of the top electrode (reproduced from [44]).

in the organic layer(s) will induce an equal and opposite charge, its mirror image, in the electrode. There is then necessarily a force of attraction between a charge and its image, which effectively lowers ϕ_B. Overall, the potential in the direction of the field (perpendicular to the electrode plane), V(x), is described by,

$$V(x) = \phi_B - \frac{e^2}{16\pi e_0 e_r x} - eFx \tag{2.27}$$

Where the first term is the injection barrier, the second results from the image charge potential, and the third is from the net field, F. This is shown in Figure 2.9.

2.6 Electronic processes at the heterojunction

Having now described the behaviour of both excitons and charges, it is essential to elucidate how they can be created from each other, as it is these mechanisms that form the basis of, and essential differences between, PV and OLED behaviour. In any organic PV or OLED device, the reason that it is essential to combine at least two different semiconducting polymers is that the energies of the molecular orbitals in which the charges propagate will be offset from each other, forming a heterojunction at the interface between the two polymers. Heterojunctions are defined as type I, II, or III, depending on the relative positions of the HOMO and LUMO levels of the two polymers. It is both the type of heterojunction and the absolute energetic offset between the levels,

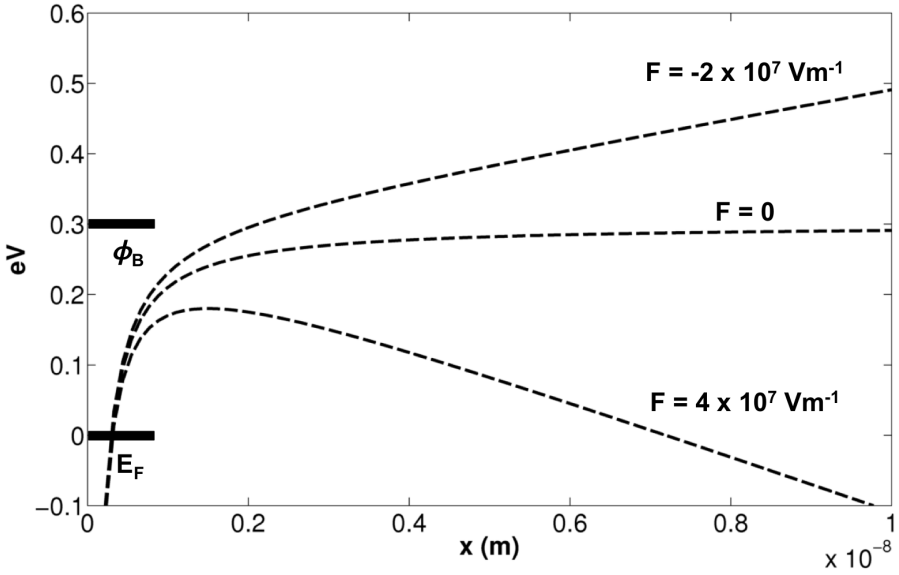

Figure 2.9: Band bending at the metal-semiconductor interface, from Eq. 2.27, for ϕ_B = 0.3 eV.

that determines the behaviour of particles at the interface. Although much of the work contained within this thesis concerns the generalised modelling of organic electronic systems, where experimental data has been used, it is always from devices based around polyfluorene derivatives, namely PFB, TFB, F8 and F8BT. All of these polymers contain the fluorene group F8 (poly(9,9'-dioctylfluorene)), which is both fluorescent (hence the name) and electroluminescent. They are frequently used by experimentalists due to their high chemical stability, good charge transport and luminescence properties, and they form the basis of many PV and OLED devices. Experimentally, the energies of the HOMO and LUMO levels of these and other polymers are determined by cyclic voltametry. Both the PFB:F8BT and TFB:F8BT combinations are found to form type-II heterojunctions at the interface, though PFB:F8BT is an efficient photovoltaic, and TFB:F8BT an efficient light-emitter. The reasons behind this, in terms of exciton and charge behaviour at the heterojunction, will now be explored, with reference to Figure 2.10.

Exciton formation has already been described in Section 2.3.1, and diffusion from donor (D) to acceptor (A) chromophores in Section 2.3.2. Following the notation used there, the photogenerated exciton will initially form on an acceptor chromophore, with the excited state dubbed A*. The high binding energy of the exciton, of the order of 0.5 eV,

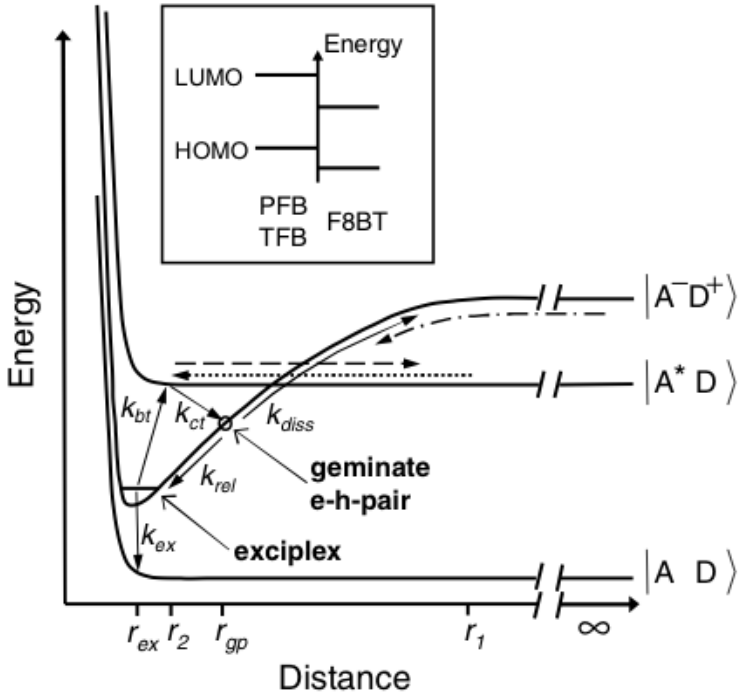

Figure 2.10: Potential energy diagram describing the energetics and kinetics at type II polymer heterojunctions (reproduced from [48]).

means that it cannot be dissociated in the semiconductor bulk at room temperature, but only at a type-II heterojunction (type-I heterojunctions merely facilitate exciton transfer to the copolymer of smaller bandgap, changing the colour of the light emission or absorption). Even then, dissociation will only be efficient if the band-edge offset at the heterojunction exceeds the exciton binding energy. If this is the case, then if the exciton successfully diffuses to a heterojunction before it recombines, then the charge separated geminate state lies lower in energy than the exciton state, and dissociation will be achieved, at a rate k_{ct}.

Following exciton dissociation, the polymer with the deeper LUMO level, in this case F8BT, will 'accept' the electron, which is why it is termed the electron acceptor/conductor, or n-type polymer. The polymer with the higher HOMO level, in this case PFB, will accept the hole, which is why it is termed the electron donor/hole conductor, or p-type polymer. Thus the A/D nomenclature applied to exciton transport (where D and A are merely the initial and final locations of an exciton during a hop) can be applied to the polymers that accept or donate the electron, respectively, though the charge polarisation

that results leads to them being dubbed A^-D^+. When so applied, the naming scheme is relative, and a polymer that is typically used as an acceptor and conductor of one charge type following dissociation can be used to conduct the other, if suitably combined with a different polymer with appropriately selected energy levels, leading to ambipolar charge transport [49].

Dissociation does not directly yield free, uncorrelated charges, but instead creates a geminate electron-hole pair. Efficient photovoltaic behaviour is exhibited in polymer combinations where the full dissociation of the geminate pair (diagrammatically donated with the rate k_{diss}), characterised by a greater separation between them, is highly likely. The alternative is that the geminate e-h pair will collapse (with a rate k_{rel}) into localised excited-state complex, termed an exciplex, which may then fully collapse (with a rate k_{ex}), with the energy lost from the system. However, exciplexes, which can also form from electron-hole capture of separate charges, are capable of endothermic back-transfer into an exciton state, occuring at a rate k_{bt}. This mechanism is thought to be a likely precursor to the generation of excitons in TFB:F8BT OLED devices. Additionally, in an OLED device, the band-edge offset at the heterojunction is usually insufficient to dissociate the newly formed exciton, making recombination with accompanied photon emission more likely.

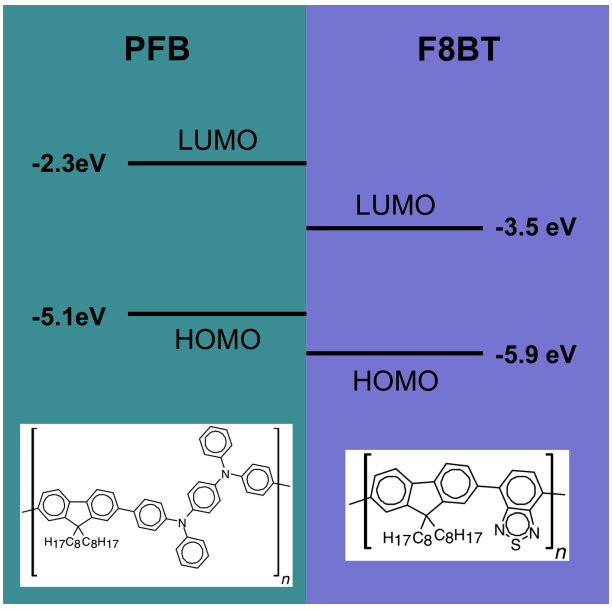

Figure 2.11: The PFB:F8BT type-II heterojunction, showing the HOMO/LUMO levels [50, 51, 52] and the chemical structures (reproduced from Ref. [48]).

Chapter 3

The Kinetic Monte Carlo model

Having expounded the essential physics of organic photovoltaics, this chapter will go on to discuss how this theory is implemented in the device model.

3.1 Organic device modelling

For organic devices, computer modelling is an essential tool for developing an understanding of the underlying device physics, and hence guiding improvements in device design. Over the last few years, various modelling approaches have been applied which can reproduce many experimental characteristics of organic electroluminescent, photovoltaic and FET devices. Model types that have been used include drift-diffusion, Master Equation and Kinetic Monte Carlo approaches.

Drift-diffusion models, such as those by Barker [53], Koster [45] and Martin [54], find solutions to the coupled drift and diffusion equations that describe charge transport. In simple models, these may be solved analytically, but in more complex modelling, such as for two-dimensional structures (e.g. Williams [55]), these equations must be solved using a numerical method such as Finite Element modelling. Such models have proved extremely useful, utilising well established mathematical descriptions of organic device behaviour, and can be executed relatively quickly. However, such models are unable to

take full account of the effect of three-dimensional structures, instead reducing a complex morphology to a basic homogenous description or a simplified two-dimensional structure. They also do not normally take full account of the related process of exciton dissociation, which has multiple stages that are critically influenced by morphology [48, 41].

The Master Equation approach solves the Pauli Master Equation in order to find the occupation probabilities of the sites on a lattice, based on hopping rates between sites, from which currents can be calculated (for a more detailed explanation see, for example, Refs. [37] and [56]). The use of a lattice and discrete charge hopping rates makes this method more akin to the KMC than the other approaches, whilst also being numerically more efficient [57, 56]. However, it only works for low charge densities, and requires steady state solutions [37, 58], whereas the KMC approach is a dynamical model that is not limited in these ways. Furthermore, the KMC is designed to account for multiple reaction types, rather than being limited to charge hopping, making it more appropriate for a full device model with multiple particle types. The price that must be paid for this flexibility is the vast computing resources that KMC requires.

The theory underpinning the KMC method will now be outlined, followed by a description of how it is applied to the modelling of organic devices.

3.1.1 Monte Carlo methods

The KMC model works entirely by simulating *events*, often called *reactions* due to their origins in physical chemistry. An event may be an exciton or charge hop, dissociation, recombination, injection or extraction. When an event occurs, the system (i.e. the simulated combination of polymers, electrodes and particles) can be thought of as making a transition from a state α to a state β. The physical nature of these processes has already been laid out in Chapter 2, as has the *rate* associated with each one. This rate is usually a function of several variables, most notably the energies of the initial and final sites of the particle(s) in question. The KMC model simulates the temporal evolution of the system, one reaction at a time, by finding all of the possible events that can occur, calculating their associated rates, and then calculating the *waiting time*, τ, associated with each, i.e. how much time will elapse before an event occurs and the system makes the transition $\alpha \rightarrow \beta$. Calculations of the waiting time allows the simulation to execute

each event at the correct time, and hence maintain events in the correct order. The complication with calculating waiting times is that individual events that have a fixed overall rate do not occur with a fixed temporal spacing. Instead, the waiting times are stochastic, chosen randomly from a fixed *probability distribution*. These distributions are calculated using a Master Equation, and it is this calculation that is the subject of the present section. Implementing the values of τ in the device model is the subject of the next section.

3.1.2 Solving the Master Equation

Starting with the general case where the rate of change of P is proportional to its magnitude,

$$\frac{dP}{dt} = -\varrho P(t) \tag{3.1}$$

Where ϱ is a rate constant. Such an equation describes scenarios that are equivalent to that in the KMC simulation, which can be useful in elucidating it. For example, in radioactive decay, the decay rate, $\frac{dP}{dt}$ is proportional to the amount of a substance that has not yet decayed, P, and ϱ is the decay constant. Hence the rate of decay at any time t can be precisely calculated from knowledge of ϱ, and vice versa. In such a scenario, the mean lifetime would simply be $\tau = \frac{1}{\varrho}$. However, even if the decay rate is precisely known, the exact time when a decay event, such as the emission of an α particle, will occur is still random. Therefore, it it were to be modelled, it would need to follow some probability distribution with a random element. Another example is an ensemble of particles, where the rate of change of the population (rate of hopping events) is proportional to the population magnitude (those which have not yet hopped). The same is true of the reactions kinetics modelled in the KMC simulation. The exact time at which a reaction occurs, i.e. the waiting time τ before the transition from the initial state α to the final state β, will follow a probability distribution based on the reaction rate, ϱ. Adopting this nomenclature,

$$\frac{dP_\alpha}{dt} = -\varrho P_\alpha(t) \tag{3.2}$$

Which states that the rate of change of the probability of remaining in a state α is proportional to the probability of being in that state α. The negative value indicates that the state can be thought of as decaying from $P = 1$ at $t = 0$ to $P = 0$ at $t = \infty$.

The solution could then be expressed as,

$$P_{\alpha\alpha}(t) = e^{-\varrho t} \tag{3.3}$$

Where $P_{\alpha\alpha}$ is the probability of remaining in the state α, i.e. making the transition $\alpha \rightarrow \alpha$. Alternately stated, this is the probability that the reaction $\alpha \rightarrow \beta$ has not yet occurred after a time, t, has elapsed. Therefore, the probability that the reaction has occurred after a time, t, has elapsed is,

$$P_{\alpha\beta}(t) = 1 - e^{-\varrho t} \tag{3.4}$$

The probability of a reaction occurring at a particular time, t, is the differential of this expression with respect to t,

$$P'_{\alpha\beta}(t) = \varrho e^{-\varrho t} \tag{3.5}$$

This can be demonstrated by re-integrating this expression from 0 to ∞, which will yield the probability that a reaction takes place over this time, which must equal 1. Therefore, Eq. 3.4 can be seen as the cumulative distribution function for the event's occurrence.

Now, if a variable t has a cumulative distribution function $P(t)$, which has an inverse $P^{-1}(t)$, and X is some random number, uniformly distributed over the interval 0:1, then t has the same distribution function as $P^{-1}(X)$.

$$P_{\alpha\beta}(t) = \int_0^t \varrho e^{-\varrho t} dt = 1 - e^{-\varrho t} \tag{3.6}$$

$$t_{\beta\alpha} = P^{-1}(X) = -\ln(1-X)\frac{1}{\varrho} \tag{3.7}$$

Although this will not be proved here, it can be demonstrated by examining the extreme cases of a peaked and a flat distribution of the probability of the events' occurrence. As X is a random number between 0 and 1, then so is (1-X), so the final solution can be re-written as,

$$t_{\beta\alpha} = -\ln(X)\frac{1}{\varrho} \tag{3.8}$$

3.1.3 The First Reaction Method

The First Reaction Method is a simulation methodology for applying the solution to the Master Equation derived above. Originally devised by Gillespie in 1976 [59], it is a computationally efficient means of modelling reaction kinetics. It works by evaluating all the events particles can partake in, and selecting the most likely event for each particle, based on its waiting time. Each event and its waiting time is held in a queue, which is executed in chronological order. When an event is executed, a new event is found for the particle in question, and inserted into the queue in the correct place.

Calculating the possible events and their associated waiting times is accomplished using particle type-specific subroutines. These evaluate every possible event that a particle can partake in, based on the particle type and location, and calculate the rate associated with each. For instance, the electron subroutine examines all of the neighbours within a range ξ of the electron location, and for every neighbour which is either an unoccupied electron conducting polymer site, or an electrode site, the hopping rate is calculated using Eq. 2.25. If it is adjacent to a heterojunction, with a hole directly on the other side, then one of the events open to it is recombination, which has a fixed rate k_r. From every rate is calculated a waiting time from Eq. 3.8, and the event with the shortest waiting time, the *fastest event*, is inserted into the queue.

The queue always contains the fastest event for every particle in the system, stored in chronological order, so that the event at the top is the *first reaction* that will occur.

Specifically, each event in the queue will contain the particle type, the initial and final location, the waiting time τ, and, where applicable, a particle ID. The particle ID is used for distinguishing between geminate and bimolecular recombination events, where applicable. When the first reaction takes place, the particle location will be updated, and the simulation clock, T_{sim}, will be incremented by τ. A new event is then found for the particle in question, by calling the particle subroutine, and the new event will be inserted in the queue in the correct position. All other events already held in the queue will have their waiting times reduced by τ. The system then moves to the next iteration, where the new event at the top of the queue is executed.

As well as a simulation clock, a simulation counter, C_{sim}, is also used in order to determine how frequently to save the output of the simulation, and ultimately define the endpoint when it will terminate. The counter is incremented whenever a particular event occurs, and the choice of event can be modified according to the simulation purpose. For instance, it may increment with each exciton creation or hole injection event. When C_{sim} reaches a multiple of a predetermined number, the simulation status will be saved to the output files. When it reaches another predetermined number, the simulation will terminate. Using a counter to control the save and termination points is more flexible than basing these on the simulation clock. For example, if a number of simulations are being run where the injection barrier or illumination level are varied, then the temporal spacing between incremental events may vary greatly, and so it may be more practical to save after a fixed number of events, rather than a fixed amount of time.

Most events will always involve two sites. For hops, these are the initial and final locations of the particle that is hopping. For dissociation, the exciton is replaced by an electron and a hole. As one of these will take the location of the exciton, the event still only involves two sites. Following any event, the occupation change of both sites will be examined, so that along with a new event for the particle in question (if it still exists), newly *enabled events* may also be found. So a dissociation event will create two new enabled events - one for the electron and one for the hole. Before executing the event at the top of the queue, it will be checked to see if it has become disabled. A *disabled event* is one which is prevented from occurring due to a prior event. For instance, if an electron is queued to hop to a particular site index, but before this event reaches the top of the queue, this site becomes occupied by another electron, then the event must become disabled to prevent double occupancy. In this case, the electron subroutine would be called, and a new event found for the electron in question. Disabled events are identified

by comparing the occupation of the sites involved before and after the event to a list of allowed changes.

The exception to this is charge injection and exciton creation events. As these events involve particles from outside the system, only a destination site is involved. Following such an event, the destination site is examined and a new event found in the same way as before. A simulation necessarily must start with an event of this type. In a full simulation, that includes both injection and photon absorption, this involves calculating the first electron and hole injection events, and the first exciton creation event. These are inserted into the queue. The simulation then begins with whichever of these is deemed to be the very first reaction. It then continues as described above. The queue will never become empty, as at least one electron injection, hole injection and exciton creation event will be held in there at any one time, due an event replacement technique, described in Sections 3.2.2 and 3.2.3 for excitons and charges respectively. If all the particles in the system recombine or get extracted, the system moves forward to the next particle creation event.

Clearly, the key approximation of the FRM is that events stored in the queue are based on the state of the system as it was when they were calculated, and not when they are executed. In-between initial calculation and eventual execution of an event, the state of the system will have changed due to events that will have occurred in the interim. As well as possibly disabling events, these may, for example, affect the local field, due to the movement of the charges which generate it. This approximation, therefore, relies on the assumption that the reaction at the top of the queue is substantively similar to the first reaction that would be calculated based on the present state of the system. The reduction in computing time created by using the FRM scales approximately with the number of particles in the system. In photovoltaic simulations, the system may contain up to $\approx$100 particles at any one time, so the simulation time is reduced by a factor of up to $\approx$100 when using the FRM instead of a more exact method. However, as the number of particles grows, so does the change in the system that can occur between original calculation and eventual execution of an event, ergo the accuracy of the FRM is likely to reduce with particle count. The validity of the the FRM when applied to organic photovoltaic simulations is the subject of Chapter 4. The alternative is to recalculate the possible events for every particle after each event is executed, a methodology also assessed in that chapter.

A flow diagram of the FRM is shown in Figure 3.1.

3.2 The KMC model used in this thesis

A device is represented by a three-dimensional Cartesian array, of dimensions $x \times y \times z$. This array represents a physical lattice, with a lattice constant $a = 1$ nm. x is taken as the dimension perpendicular to the electrodes, and thus parallel to the built-in field, $\underline{F}$. Periodic boundary conditions are applied in the y and z dimensions. Each point in the array can be considered as a point of localisation for both charges and excitons. Representing polymers in this fashion is a simplification that neglects their true chain-like structure, and thus also neglects resulting effects such as anisotropy, caused by variations in chain alignment and differences in inter- and intra-chain transfer rates; chain rotation [39] and inhomogeneity [60]. Including such effects would introduce a vast number of unknowns into the model, which are best computed using other means, such as quantum chemical calculations [58, 61]. Even if they could be deduced with reasonable accuracy, the computing time required to run a device model would vastly increase, potentially by orders of magnitude. At the device level, many of these effects can be considered to be 'averaged out', explaining the success of drift-diffusion models, where the level of morphology representation is simpler than here.

A single simulation utilises five parallel arrays of these dimensions, each storing a different value associated with a site:

- The morphology array, which represents physical site type.
- Three energetic arrays, storing the energies of exciton, electrons and holes at each site.
- The occupation array, which records the particle type at the site, if there is one.

These arrays, and their associated reactions, will now be discussed in turn.

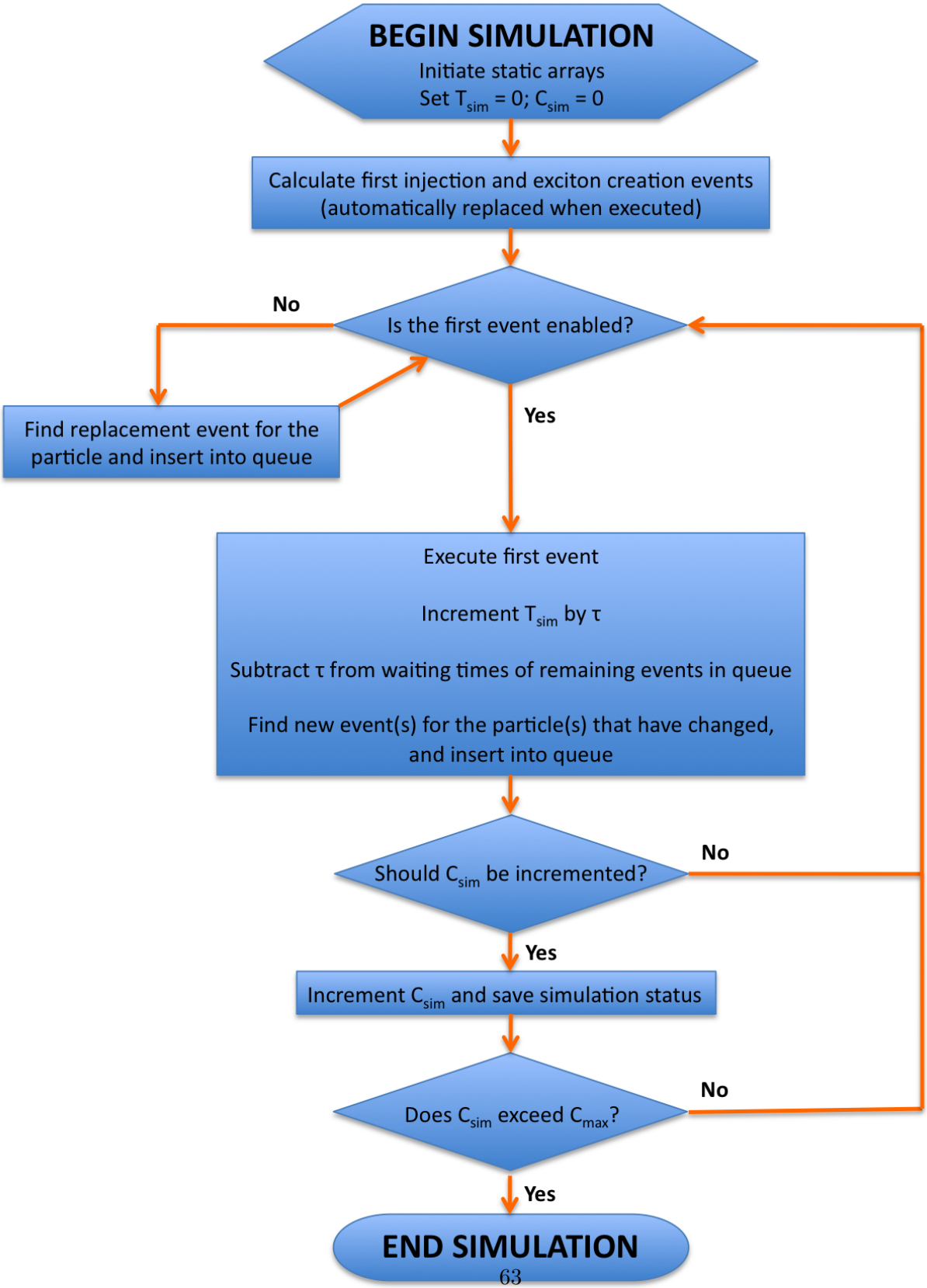

Figure 3.1: Flow diagram of the FRM

3.2.1 The morphology array

Morphology arrays are static, generated prior to the KMC simulation, and loaded at the start. Each site in the morphology array is assigned one of four labels:

- a: Anode sites
- p: 'p-type', hole conducting polymer sites
- n: 'n-type', electron conducting polymer sites
- c: Cathode sites

There is additional scope to add further polymer types, to account for, for example, the blending of copolymers. The electrodes are modelled as monolayers, plane-parallel to yz, and placed at x=0 and x=x_{max}, making the physical length of the device $l = ax_{max}$. An electrode site is not technically a site of charge localisation, but simply a point of entry or exit of charges, a methodology discussed in more detail in Section 3.2.3.

The morphology of the device is represented by the arrangement of n and p sites in the morphology array, and so each real-world morphology is reduced to its cubic lattice equivalent. The following sections describe how this is achieved for different classes of morphology. In Chapter 5, each of these morphology classes will be thoroughly investigated and compared to the others in terms of different measures of device efficiency.

Disordered blend morphologies

Blend morphologies are created by dissolving the two polymers in a common solvent, then spin-casting or doctor blading them onto the transparent bottom contact (normally ITO), with the top metallic contact then evaporated on top [6, 62, 63, 27]. The mixing process makes the resultant morphology highly disordered. Devices are usually then annealed, which causes phase separation of the finely blended polymers, lowering the interfacial area and increasing the average size of connected features of the same polymer (l_f). Along with the annealing time and temperature, the choice of drying time and

solvent can also affect the morphology [64, 60, 65]. As the interface between the two polymers constitutes an electronic heterojunction (discussed in Section 2.6), the distribution of this interface throughout the bulk of the device means it is referred to as a *bulk heterojunction* device. Since its inception in 1995 [66, 67], the bulk heterojunction has become something of the status quo in device design, due to its simplicity, efficiency advantages over bilayer devices, and the difficulty in reliably constructing ordered morphologies on the same scale.

For the purposes of simulation, blend morphologies are approximated using a simulated annealing program. The program employs an Ising model algorithm, named from its original use in magnetic Ising model simulations [68]. Generally, such an algorithm simulates the evolution of a system containing two site types, labelled A and B. These types may represent features such as magnetic spins, or, as in the case here, polymer types n and p. In such an algorithm, the energy of the system is calculated in terms of whether neighbouring site types are like or unlike. Like or unlike neighbours combinations are assigned different amounts of energy, and the total energy for the system calculated. The program then attempts to lower this total. In the polymers being studied, it is known that chemical incompatibilities result in a system that favours like neighbours over unlike ones, so that as the system evolves and the energy lowered, it will phase separate. This is entirely equivalent to ferromagnetic systems that favour adjacent spins to be like (parallel) rather than unlike (antiparallel).

The program itself proceeds as follows. Having constructed a regular 3D Cartesian array to represent the morphology, each site type is initially randomly assigned as either n or p, in a 1:1 ratio, though in actuality they are handled as logical values at this point, rather than characters, for speed of execution. The ratio reflects the quantities typically used in polymer blend solar cells, and the fine intermixing mimics the morphology created following initial deposition of a layer where the two polymers which have been dissolved and mixed in a common solvent. This is the finest level of intermixing, and generates a morphology with the smallest feature size. The purpose of the program is then to mimic phase separation by lowering the internal energy of the morphology. Experimentally, phase separation occurs by the interdiffusion of neighbouring sites [68], perhaps through the presence of vacancies [69]. There are different ways of modelling this, such as a Metropolis algorithm or cellular automata. The choice of method is somewhat arbitrary, as the desire is simply to create a computationally efficient method of mimicking phase separation, and we are not interested in the level of detail for which these methods were

originally devised, such as the rate at which transitions occur or the exact nature of the morphological evolution. Here, Kawasaki spin-exchange dynamics are used, following the method of Adams *et. al.* [68]. This uses some of the terminology and calculations derived for spin exchanges to model an entirely analogous system.

The free energy associated with the molecular contact of different site combinations is first chosen. Although it is possible to calculate these values precisely for certain molecules, it is unknown for many others of interest, and for the purposes of this work, the exact values are unnecessary [69]. The values can therefore be assigned arbitrarily, and any values where like sites have a lower energy than unlike sites will work, as this energetically favours phase separation. This is expressed in terms of a Kronecker delta function δ_{ij} for sites i and j, which may be of type n or p.

The algorithm then investigates the impact of swapping a randomly chosen site with one of its neighbours, also chosen at random. It achieves this by calculating the total energy before and after the swap is made, by taking the two sites in question (i_1 and i_2) and summing the energetic contributions of all their neighbours j, according to whether they are of the same or opposite site type. If non-nearest neighbours are considered, the energy contribution is weighted by distance factor w. The summation is only performed for these two sites, as sites beyond their neighbour range are unaffected by the swap, and hence cancel each other out in the calculation of ΔE. Here, the 6 nearest neighbours, and 12 next nearest neighbours are included, the latter being weighted by $w = \sqrt{2}$. If ϵ_{i_1} is the Ising hamiltonian of site i_1, then $E = \epsilon_{i_1} + \epsilon_{i_2}$,

$$E = -\frac{J}{2} \sum_{i_1 i_2} \sum_{j=1}^{18} w(\delta_{ij} - 1) \tag{3.9}$$

Where J is the exchange interaction between nearest neighbour spins[1]. The energy difference $\Delta E = E_{new} - E_{old}$ before and after i_1 and i_2 are swapped can then be found, and the probability of a swap being accepted is taken from Kawasaki spin-exchange dynamics [70]

[1]This method is equivalent to the expression in Peumans *et. al.* [69] or Groves *et. al.* [60] of setting $2E_{AB} = E_{AA} = E_{BB}$; $2E_{AB} - E_{AA} - E_{BB} > 0$ and reversing the sign of Eq. 3.9.

$$P(\triangle\varepsilon) = \frac{\exp(\frac{-\triangle\varepsilon}{k_B T})}{1 + \exp(\frac{-\triangle\varepsilon}{k_B T})} \tag{3.10}$$

The Monte Carlo algorithm chooses whether to accept the swap by evaluating whether $(R < P)$, where R is a random number of a uniform distribution over the interval 0:1, and if true, will accept the swap. The process is then repeated over a large number of Monte Carlo steps, creating gradual changes in phase separation. The state of the system is saved periodically, creating a range of morphologies with different interfacial areas, which can then be modelled. These are illustrated in Figures 3.2 to 3.5, which show the morphology produced by the Ising Model after 10, 100, 1000 and 10000 Monte Carlo steps.

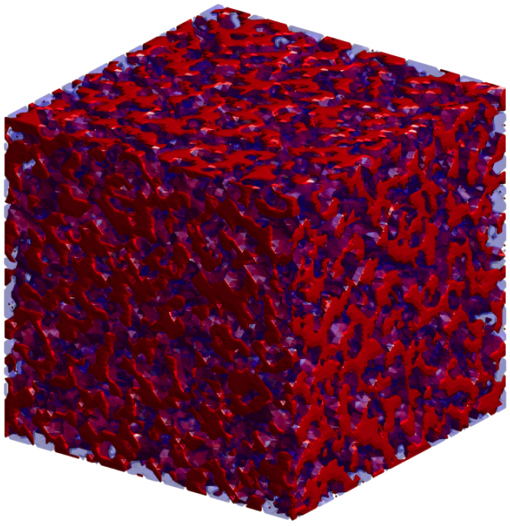

Figure 3.2: Ising model morphology after 10 Monte Carlo steps.

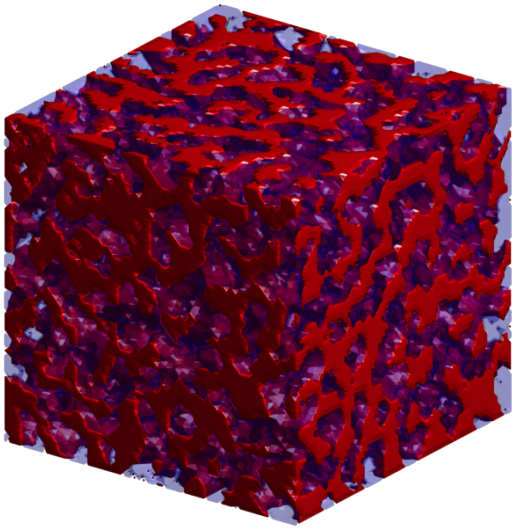

Figure 3.3: Ising model morphology after 100 Monte Carlo steps

Bicontinuous, minimal surface morphologies

Bicontinuous, minimal surface morphologies are ordered structures which can form by spontaneous self-assembly. Details of their geometry, physical formation and potential use in polymer photovoltaics are given in Section 5.2. The datasets representing the morphologies were generated by Gerd E. Schröder-Turk of the Institut für Theoretische Physik, Friedrich-Alexander Universität, Germany, and not the author. As such,

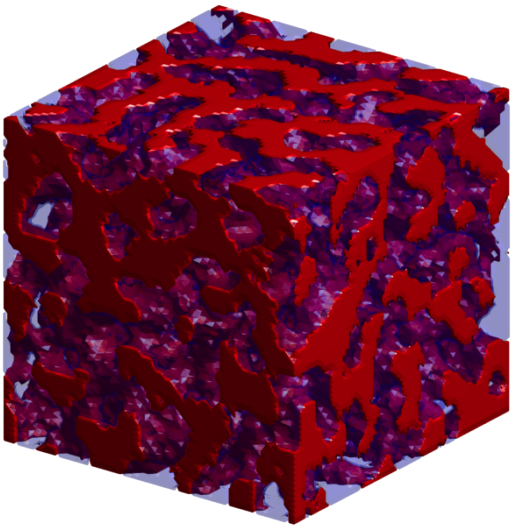

Figure 3.4: Ising model morphology after 1000 Monte Carlo steps.

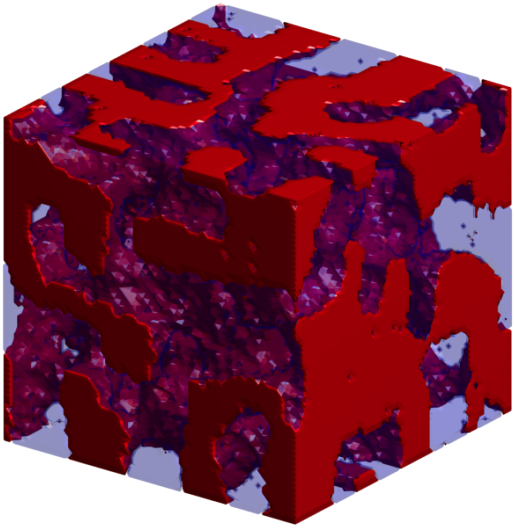

Figure 3.5: Ising model morphology after 10000 Monte Carlo steps.

full details of their generation will not be given. These datasets were converted into the appropriate coordinate system for the KMC model using a simple Matlab code written by the author. Their creation starts with the computation of a triply-periodic minimum surface, onto which is superposed a three dimensional grid. The minimum surface divides the morphology into two labyrinthian-like solid regions that are themselves triply-periodic. The final morphologies can then be generated by one of two mechanisms:

- First, a single geometry such as the single gyroid or single diamond, is derived by setting all the sites in one of the two labyrinthine domains to n, and those in the other domain to p, yielding a structure with 50% volume fraction of both domains. This procedure generates a partition of space into two identical domains.
- Second, double geometries are derived by setting all sites within a given distance Δ from the minimal surface to n and all others to p. This procedure yields a partition of space into two network- or labyrinth-like p domains separated by a layer of n sites (often termed the matrix). The volume fraction of n sites can be adjusted by the choice of Δ, and here is chosen to maintain a 50% volume fraction of both domains, as for the single geometries.

The binary datasets, from which the morphologies are created, are obtained by generating surface patches representing $n \times n \times n$ cubic translational unit cells of the gyroid or diamond surface, using the Weierstrass parametrisation (see, for example, [71]). With a choice of $b = L/n$ for the lattice parameter b and a given box width L, this yields surfaces that divide the box $[0, L]^3$ into two intertwined labyrinth domains. The Cartesian array of M^3 sites (hence of inter-site spacing L/M) is superposed over this box and each site value adjusted to n or p according to the scheme detailed above (which for the double geometries involves the computation of the so-called Euclidean distance map). The morphologies utilised in Chapter 5 are obtained for n=1,2,4,8; L=64 and M=64. All of the morphologies have 50% volume fraction of both phases.

Other morphologies

Several other morphologies are also utilised in the simulations described in this thesis. Bilayer morphologies can be easily created by setting all of the sites on one side of the mid-way point in x to n, and the others to p. Vertical, square rod morphologies are generated using a simple code that creates alternating square blocks of polymer in a chessboard layout, and then replicates this in x to produce rods, the thickness of which can be varied. A vertical rod morphology has often been suggested as being ideal for solar cell applications, although it has yet to be fully realised in experiment. It can be approximated by a number of means, including SAM printing [72], nanoimprint lithography [73] or, as will be seen below, through spontaneous self-assembly of the constituent polymers, either in situ or prior to annealing. An alternative means would be to create a hybrid cell where the electron conducting polymer or fullerene is replaced by either nanorods [74] or nanotubes [75].

Interfacial area and feature size

The interfacial area of any morphology is calculated using a very simple algorithm. The system examines the type of lattice site, and then the type of its six nearest neighbours. Where the two sites are of different types, the interfacial area is incremented by an area $a^2 = 1$ nm^2. This is repeated for every site in the array. The total interfacial area is then divided by two, due to double counting of each interface. Finally, the area of the

electrodes is subtracted. This interfacial area A is converted to a characteristic feature size l_f of a volume V using

$$l_f = \frac{3V}{A} \tag{3.11}$$

3.2.2 The exciton array

The exciton array contains the energy an exciton will have when it become localised on any of the sites in the array, allowing fast calculation of the hopping rates according to Eq. 2.13. The energies in the array describe the energetic disorder of the polymers, and are drawn from a static distribution, usually a Gaussian of width σ. The origin and use of different descriptions of energetic disorder is given in Section 6.2. The calculation of the photon absorption / exciton creation distribution and temporal spacing has already been discussed in Section 2.1.2. As exciton creation does not result from an internal reaction, but rather from the absorption of radiation which is incident at a fixed power density, the waiting time used is not subject to the first reaction method. Exciton flux is maintained in the queue using an event replacement technique. At the beginning of the simulation, the first exciton creation event, with the correct waiting time (based on the optical flux), is inserted into the queue. Upon execution, this event is instantly replaced with another with the same waiting time. This ensures an accurate model of fixed photon flux.

Following formation, exciton transport will occur as described in Section 2.3.3. If the exciton reaches a heterojunction before recombining, then a new reaction, that of dissociation, becomes open to it. The dissociation rate is taken as $k_{ct} = 1 \times 10^{10}$ s^{-1} [76]. The resulting geminate pair is modelled as a discrete electron and a hole, placed on neighbouring sites either side of the heterojunction, each in the correct polymer, and hence one of the charges will take the place of the exciton. The charge pair remains tightly bound, due to the strong coulombic attraction over the distance of separation, which is initially the lattice constant, a. Both charges are then able to hop away, or recombine to the ground state. The possibility of 'double recombination' in this scenario is dealt with in Section 4.3.1. The intermediate exciplex state is not modelled in PV devices, as it was deemed unnecessary where exciton regeneration is unlikely, and so

recombination occurs directly to the ground state, with a rate k_r. As the origin of k_r is not well established, the value used will vary, and quoted in the relevant section of this thesis where the modelling is applied. The branching ratio between geminate pairs that recombine and those that fully separate effectively comes from the FRM competition between k_r and the individual hopping rates for the charges, calculated using Marcus theory.

3.2.3 The electron and hole arrays

In the same way as for excitons, in order to efficiently calculate charge hopping rates from Equations 2.25 and 2.16, the values of E_i and E_j need to be found quickly. The electron and hole arrays hold the static contributions to these values, incorporating the same disorder description as the exciton array; as well as the contribution of the overall field and the injection barriers for electrons (ϕ_{Be}) and holes (ϕ_{Bh}), as described in Section 2.5 and by Eq. 2.27. E_i and E_j also include a dynamical contribution, $\triangle$V, due to the presence of other charges. At any particular site, i, $\triangle$V due to all other charges at sites j_n, is calculated as,

$$\triangle V = \sum_{j=1}^{n} \frac{qe}{4\pi\epsilon_0\epsilon_r r_{ij}} \tag{3.12}$$

where n is the number of other charges in the system; $q = +e$ for electron-electron and hole-hole repulsion and $-e$ for electron-hole attraction; and r_{ij} is the distance between charges i and j. Care must be taken not to include the coulombic presence of the charge at i when calculating possible hopping rates, as this will result in self-interaction.

In other KMC models [32, 77, 78, 79, 80], whenever a charge moved, $\triangle$V has been calculated for every site within a specified cutoff radius, r_c, of the old and new locations of the charge, and the electron and hole arrays updated. However, this approach involved thousands of calculations for every charge hop, an approach deemed unnecessary here, due to the low charge densities in organic photovoltaics. Instead, $\triangle$V is calculated by the electron and hole event subroutines when determining the fastest hopping event, and is only applied to the present location of the charge and to each possible destination

site. For example, in the case of a hopping range of $\xi = 3a$, each charge has up to 122 neighbours to which it can hop. If there are 20 other charges in the system, the result is (122+1) x 20 = 2460 calculations per hop. This contrast with updating all the site energies in the arrays within the cutoff radius, which for $r_c = 10$ nm is ≈ 10000 calculations. This approach removes the need for a cutoff radius entirely, extending the range of influence of each charge to the entire system, maximising accuracy. Clearly, this approach is only computationally efficient as long as the product of the number of charges in the system and the number of neighbours for each charge remains below the number of sites within r_c.

As for image charges reflected in the electrodes, this is calculated by adding an extra factor to Eq. 3.12, which effectively places an equal an opposite charge a distance $2x_{a/c}$ away, where $x_{a/c}$ is the distance in x from the anode / cathode. In terms of evaluating the necessity of taking into account multiple reflections, Casalegno *et. al.* [81] evaluated the use of the Ewald sum technique in KMC simulations by comparing it to the use of a potential array with a cutoff (as already described). It was found that under these circumstances, neglecting the Ewald sum technique underestimated efficiency. However, it was also found that extending r_c beyond 16 nm created excellent agreement between the potential array and Ewald sum techniques. Furthermore, in the work by van der Holst *et. al.* [37], where the image charge is taken into account, it is noted that although this image charge represent only the first term in an expansion of repetitive images, no significant change in the results was obtained when taking higher order images into account. Consequently, from the work of these two groups, and given the absence of any cutoff in the application of Eq. 3.12 here, it is believed that there is no need to take repetitive image charges into account.

Modelling mobility

The definition and nature of mobility has already been described in Section 2.4.6. In order to measure the mobility of a device with any particular morphology and material parameters, a variant of the primary KMC code has been created. In this variant, the simulation begins by creating a single charge at a random location within the device. The charge then explores a continuous block of polymer, i.e. with periodic boundary conditions applied in all three dimensions, without electrodes or image charges. The

application of a field and periodic boundary conditions in x means an adjustment must be made to the value of $E_j - E_i$ when hopping from $x = l$ to $x = 0$ (or vice versa) to account for the step change in potential, so that the charge sees the field gradient as continuous. After each hop, the charge displacement parallel to the field is recorded, incrementing a running total. When the net displacement in x reaches a predefined value, d, the mobility μ_i is calculated using Eq. 2.21, where t is the total simulation time elapsed, which is the sum of all the hop waiting times, τ. The simulation is then reset for a new charge. After 100 such charges the simulation is reset again, but this time with a new configuration of Gaussian disorder, with the same width σ, which another 100 charges will pass through. The mobility for any particular combination of device morphology, material parameters and field is the mean value $\overline{\mu_i}$ averaged over 500 configurations of disorder. For each morphology/parameter combination, field values are taken in the range $F^{0.5} = 1000 : 10000$ $(\mathrm{V/m})^{0.5}$.

Modelling the mobility in terms of a fixed distance instead of a fixed number of hops runs contrary to the work of some other groups [82], but is essential. This is best illustrated by considering the case of devices containing traps significantly below the energetic disorder range. Taking a fixed number of hops, at low field the net displacement of the charge will be small, due to the random walk. This means it will only explore a relatively small section of the device, especially as it is also more likely to re-visit sites. If traps are evenly distributed around the device, a charge at low field will encounter relatively few of them, due to the limited range of exploration. In contrast, at high field the net displacement of the charge will be large, meaning that for a fixed number of hops it will explore more of the device. Furthermore, it is less likely to re-visit sites, meaning that a greater proportion of the hops will be to new locations. Therefore, it is likely to encounter more of the traps in the device. Deep traps have very long waiting times for escape (from Eq. 2.25), and so it is they that will dominate the mobility, rather than the increasing randomness of the walk taken at low field. As a result, the mobility becomes controlled by the number of trap encounters, which can increase with field, resulting in a negative field dependence of the mobility. This is counter-intuitive and rarely observed in polymers.[2] If, instead, mobility is modelled in terms of fixed distances, then the same length of the device must be traversed by charges at any field, restoring the intuitive and widely encountered positive field dependence. This was confirmed by

[2] An exception to this is sometimes observed at low fields, where high disorder and/or weak coupling between sites can mean that the most favourable hops might be in directions opposite to that of the field, and therefore increasing the field will diminish such hops [17].

running simulations (not shown) using these two methodologies.

Charge injection

As described in Section 2.4, modelling charge transport using Marcus theory is preferable to using the Miller-Abrahams expression due to the rigorous nature of its derivation from charge transport theory. However, this small polaron rate is not applicable to injection from the electrode into the polymer, and so it becomes necessary to resort to the conventional Miller-Abrahams (MA) expression for injection and extraction events, whilst retaining the small polaron rate for all other hops. In the absence of a rigorously defined physical theory for describing injection events, this working empirical relationship, which has been successful in many previous descriptions of charge injection, will suffice. The injection mechanism implemented here is similar to that used by Wolf, Arkhipov and Bässler [83], and subsequently by others [37][3].

Charges in the electrodes are not explicitly simulated, as this is deemed to be an unnecessary waste of simulation time. Instead, injection is simulated by the appearance of charges at the destination sites of injection events, with the correct waiting time. The Fermi levels of the electrodes are pinned at the initiation of the simulation - they are not affected by charge flowing in or out, as these processes do not affect the density of the overall 'sea' of charge already sitting in the electrodes. Charge injection is calculated by first choosing a random site on the appropriate electrode. The polymer neighbours of this site are then examined for the possibility of injection, and waiting times to all unoccupied sites of the correct polymer type (electron or hole transporting, as appropriate) are calculated. The energy of each possible destination site, E_j, is calculated in the same way as for other hopping events, i.e. from Eq. 2.27, combined with the local field due to charges, Eq. 3.12. The injection rate is then calculated using Eq. 2.16, where E_i is the fixed Fermi energy of the source electrode. The injection event with the shortest waiting time will be inserted into the queue, and the process repeated if multiple parallel injection events are desired (the actual time at which the charges are injected will not be simultaneous, as each will have its own waiting time, but they will be inserted into the queue at the same iteration).

[3]Clarified in discussions with the author.

The first injection event is the most significant, as the disruption to the local field can have a substantial effect on subsequent injection rates [83, 77]. Once a charge is injected, it will hop as normal, and will move between polymer sites, or return to the electrode, if this is calculated to be the fastest event. Electrode sites are always deemed to be 'free' - no Pauli exclusion principle is implemented for electrode sites as it is for multiple occupation of polymer sites, so that charges can be extracted to any site at any time. Injection works on the principle that there is always a charge waiting to be injected. As with exciton creation events, when an injection event is executed, it is instantly replaced by a new one in the queue, calculated in the same manner. In this way, there will always be the same number of injection events waiting in the queue, and there is no lag time between the execution of one event, and the calculation of the next. It is possible to have as many 'parallel' injection events in the queue as is desired, and this number will be maintained by the system. This provides a means to scale injection if necessary, though of course the same scaling must be applied to all simulations. In all the work contained in this thesis, only one injection event exists in the queue at any one time.

3.2.4 The occupation array

The occupation array stores the occupation of all sites. It is initialised at the beginning of the simulation with all sites set to 'o' - unoccupied. This is then updated as events are executed by the queue. The occupation array is frequently referred to when calculating new events for particles, and for preventing disabled events, such as double occupation of a site, from being executed.

Having described the fundamental principles of photovoltaics, the underlying scientific theory, and how this theory is implemented in the Kinetic Monte Carlo model, the rest of this thesis is concerned with modelling simulations that have been carried out, their results, and conclusions that they lead to about organic devices and their simulation.

Chapter 4

Validating the First Reaction Method

Much of the work contained in this chapter has been published in *The Journal of Chemical Physics* **133**, 144110 (2010).

4.1 Introduction

The theory of the First Reaction Method was introduced in Section 3.1.3. The FRM is a widely used approximation, and has been very successful in the modelling of chemical reactions, such as gas-phase systems [59] and surface reactions [84, 85]. However, the FRM has never been rigorously tested, nor its accuracy quantified, for specific use in polymer electronics simulations. This has led some authors to resort to more exact methods, where the computational overheads may have been unnecessary [81, 86].

A particular case in point for the accuracy of the FRM is in how it handles the simulation of geminate pair dynamics. This is vital for photovoltaic models, as calculating the exact nature of how a geminate pair behaves following exciton dissociation is crucial to calculating device efficiency. Given that, following dissociation, geminate pairs are formed at a distance of a = 1 nm apart, and also that the dielectric constant in semiconducting polymers is typically low (ε_R = 3-4); the FRM approximation might seem to be particularly invalid for photovoltaic simulations, as the changes in local field that are unaccounted for can be very significant. This makes it particularly pertinent that its validity under these circumstances be confirmed, if any conclusions reached using FRM modelling are to be substantiated. A brief comparison between the FRM and a more exact method of simulation, where all events are recalculated at every timestep, was made by Marsh *et. al.* [77]. There it was found that the two methods agreed well, but this was only tested for a small range of parameters. The aim of the present chapter is to go much beyond that work, to quantitatively compare the FRM with a more exact method of geminate pair and device simulation, across a range of fields, disorder values and charge mobility combinations relevant for organic photovoltaic device simulation. It can then be determined if, and under which circumstances, the FRM is a valid approximation which does not significantly sacrifice accuracy, and exactly how valid it is.

4.2 Geminate pair dissociation dynamics

Drift diffusion models usually make use of Onsager-Braun theory to describe exciton dissociation and to compute the geminate pair separation efficiency, defined as the pro-

portion of dissociated excitons that are successfully extracted by the electrodes, here donoted η_{gs} . As an example, Williams [55], following the work of Barker [53], made use of a simple, two-step dissociation mechanism when performing complex finite-element calculations of 2D photovoltaic devices. In this method, excitons diffuse towards a heterojunction, at which point a charge transfer (CT) state with a finite lifetime forms. This state can either recombine, with a fixed recombination rate k_r that is independent of field, or fully dissociate; creating a branching ratio between those states that produce free carriers and those that don't. The use of a metastable CT state as a precursor to free charges was the key adaptation of Braun over Onsager. Onsager had assumed that the charges that result from dissociation would either immediately recombine or become separated to infinity, depending on the range of electron transfer upon dissociation. The problem with this description, when applied to donor-acceptor polymer systems, is that fitting to experiment yielded unrealistically high electron transfer ranges (the distance the electron moves away from the hole upon dissociation) of 2-3 nm. This was inconsistent with spectroscopic evidence that the exciton state that generates the charges chiefly involves nearest neighbour electron transfer, i.e. the electron only moves as far as the next nearest point of localisation on a chain, typically $\approx$ 1 nm away. These ranges were originally rationalised at 'thermalisation lengths', but this explanation had no real justification. Braun adjusted this theory, by giving the precursor CT state a finite lifetime, during which it could be imagined that an unsuccessful separation could still reform the CT state instead of instantly recombining. This increased the probability of dissociation, and hence yielded a more realistic electron transfer range which correlated well with nearest neighbour separation [87].

Still, even Braun's theory is too simplistic, because, as noted by Barker and examined in detail by Groves [41], it neglects the effects of morphology on η_{gs}. In models based on Onsager-Braun theory, the medium of separation is assumed to be homogeneous in order to make the calculations tractable. However, in an actual device, the energetic and physical disorder may cause the CT state to reform at a different location, by forcing the charges together again en route to electrode extraction. A Monte Carlo approach to modelling can take all aspects of the morphology, both physical and energetic, into account when calculating η_{gs}. This is relevant, both for the current chapter where disorder will be considerably varied, and for Chapter 5, where the morphology will be varied. As described in Section 3.2.2, the nature of the KMC model is such that η_{gs} effectively comes from the branching ratio of the field-independent recombination rate k_r and the individual hopping rates for the charges, calculated using Marcus theory. In

the limit of a simple bilayer system of low disorder, $\eta_{gs}(F)$ should be similar for both the Monte Carlo and Onsager-Braun approaches, as under these circumstances neither the energetic nor physical morphology is likely to prevent charges from being extracted by the electrodes after initial separation. Simulations (not shown) of the same system using these two different approaches, over a field range of 10^4 - 10^8 Vm^{-1}, do indeed yield a quantitatively similar trend for $\eta_{gs}(F)$.

4.3 Method

The work that follows was conducted in collaboration with Chris Groves of Durham University, who made use of a version of the KMC code that had been written independently of the author's. The primary simulations were run on both copies of the code, which provides a test of the code presented in this thesis, and also testifies as to the portability of the method.

The aim of the present chapter is to examine how accurately η_{gs} is calculated using the FRM, by comparing it to a more exact method of simulation, where the waiting time for each event is recalculated at every timestep (further details as to the different methods of calculating events are given in Section 3.1.3). This will be achieved by running simulations where geminate pairs are created at a heterojunction in a bilayer device, which will then ultimately be extracted or recombine. The values of η_{gs} computed using the two methods will be compared, across a range of parameters. For every parameter combination, the field strength is varied from 10^5 to 10^8 Vm^{-1}, in a manner similar to Braun *et. al.* [87]. This neatly accounts for most operating conditions, from short-circuit to near-flatband. The disorder is varied from 0 to 150 meV, encompassing the range of values reported for the semiconducting polymers of interest (see Section 6.2.2). For each value of field and disorder, three mobility combinations are simulated: one carrier trapped; both carriers mobile with equal mobility; and both carriers mobile but with unequal mobility. The testing by Marsh *et. al.* only accounted for scenarios where both polymers had equal mobility, whereas the materials blended in actual devices frequently have very different mobility values, especially if a fullerene is used, where the electron mobility may exceed the hole mobility over an order of magnitude [88]. Furthermore, charge trapping can be common in devices, and trapping is sometimes enhanced near the interface [89], showing the 'one carrier trapped' simulations to also

be a particularly relevant test.

Writing Eq. 2.25 as,

$$k_{ij} = N_{e(h)}\nu e^{-2\alpha r} \exp\left[-\frac{(E_j - E_i + \lambda)^2}{4\lambda k_B T}\right], \tag{4.1}$$

these scenarios correspond to holding $N_e = 1$, and using $N_h = 0$, 1 and 10.

4.3.1 Double recombination

Most of the processes contained within the device simulation, such as hopping or dissociation, can be termed 'unimolecular' - the event primarily involves only a single particle moving between an initial and a final state, although the field changes induced by charge movement can affect other particles in the system, and dissociation will produce two particles. Recombination is a bimolecular process, that is to say it is a paired event involving two particles, and is in this respect unique in the simulation. In the KMC code, each particle type has an algorithm associated with it that calculates all the possible events ('reactions') that can occur for the particle in question, and the waiting time for each, and then chooses the fastest event and inserts it into the queue (see Section 3.1.1). In order for recombination to be possible for both electrons and holes, it must be included in the algorithms for both particle types, but this immediately leads to a problem. Following exciton dissociation, the fastest event for both the electron and hole will be calculated before the simulation continues, and as recombination must be allowed for both particles, this event is considered twice, doubling its chances of occurring. Clearly this must be corrected, but the means of correction depends on the simulation methodology being applied.

When using the exact method, the correction is simple - recombination can simply be removed as a possible process in the fastest event algorithm for one of the charge types. Whenever the charges meet, both algorithms will always be run, and so the recombination process will always be considered once, and only once. However, the FRM presents additional challenges when implementing this change. Under most circumstances, the nature of the FRM means that the recombination process will only be considered once,

as is desirable, as only one particle's fastest event will be calculated at any timestep. However, there is still the problem of double counting following initial dissociation, because the fastest event for both charge types will be found in the same simulation step. Removing the recombination action for one particle type is clearly not possible, as it may then never be considered later in the simulation.

This problem is solved by applying a logical 'marker' to this process in the code. Whenever recombination is considered (even if it is not chosen) for an electron, the electron marker is set to 'true'. When the hole subroutine is run, it checks to see if this marker is true, and if it is, it does not consider recombination as a possible event. The marker is reset the next time the electron subroutine is called. Therefore, it will only remain 'true' immediately following its consideration. The same is applied to the hole subroutine - the electron subroutine will not consider recombination if the hole one just has. Following dissociation, the electron subroutine is called first (by default if both the electron and hole locations have changed at the same time). It will consider recombination, setting the marker to true whether it chooses this event or not. The hole will then not consider recombination as a possible event, and so recombination is only considered once for the particle pair. When the electron hops away, the marker is reset. The same would be true if the hole subroutine was called first. Subsequent to these event, for the most part, the marker is irrelevant as only one charge subroutine will ever recalculate events when a recombination scenario is entered in to, and the marker will have been reset from previous actions.

There is one situation where this does not apply. If the electron chooses recombination, it can be a process with a relatively long waiting time. The hole, in the mean time, may have sufficient time to hop away from the electron and then hop back to the same location before the electron recombination event reaches the top of the queue. In the normal FRM, double counting would occur under these circumstances when a new event is found for the hole. However, using the marker approach, the electron marker will still have not been reset, as it is yet to perform an action following the initial dissociation. Therefore the hole is still prevented from examining recombination. However, the charge pair may then recombine due to the original recombination event which is still waiting in the queue - the electron does not see that the hole has left and then returned to the same location. This still compromises accuracy, as the original waiting time will have been reduced while the hole moves, meaning that when it returns the event appears to happen much more quickly. Strictly speaking, it should instead be recalculated at this

point. However, this is a part of the approximation of the FRM method in general, and exists with or without the 'marker'. In the exact method of course, this event is always recalculated.

To illustrate this, an alternative situation may be considered. Following dissociation, the electron considers recombination, but then rejects it and chooses to hop. Subsequently, the hole, of course, cannot consider recombination. The electron then hops away and then hops back. It then considers recombination again, with a fresh waiting time, not reduced in its absence. This situation is exactly equivalent to the one described above, but the probability of recombination on return is reduced, because the event has not been sitting in the queue, with its waiting time being reduced by each intermediate event.

4.3.2 Simulation parameters

The following parameters are used throughout these simulations. The choice is somewhat arbitrary, but each represents a reasonable value for polymeric semiconductors. Except where stated otherwise, hopping is restricted to the six nearest neighbours (ξ = a).

k_r	1×10^7 s^{-1}
ν	1×10^{11} s^{-1}
λ	0.25 eV
ε_r	4

Table 4.1: Parameters for FRM simulations

For every combination of parameters, 10000 charge pairs are simulated, after which a new configuration of the disorder is implemented, and another 10000 simulated. Each result is the average over 50 such configurations of the disorder. The device dimensions are (50 nm)^3.

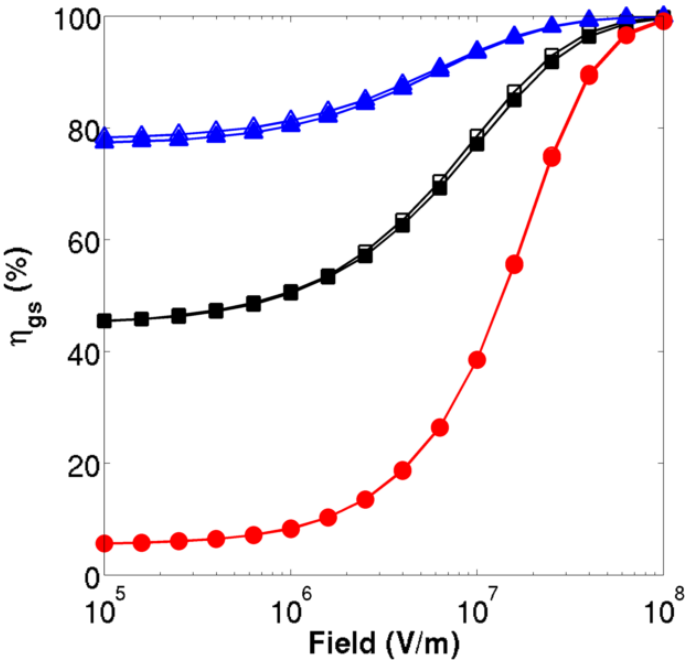

Figure 4.1: η_{gs}(F) for $\sigma = 0$ meV. Filled symbols are for the FRM, open symbols for the exact method. Red, black and blue correspond to $N_h = 0$, 1 and 10 respectively.

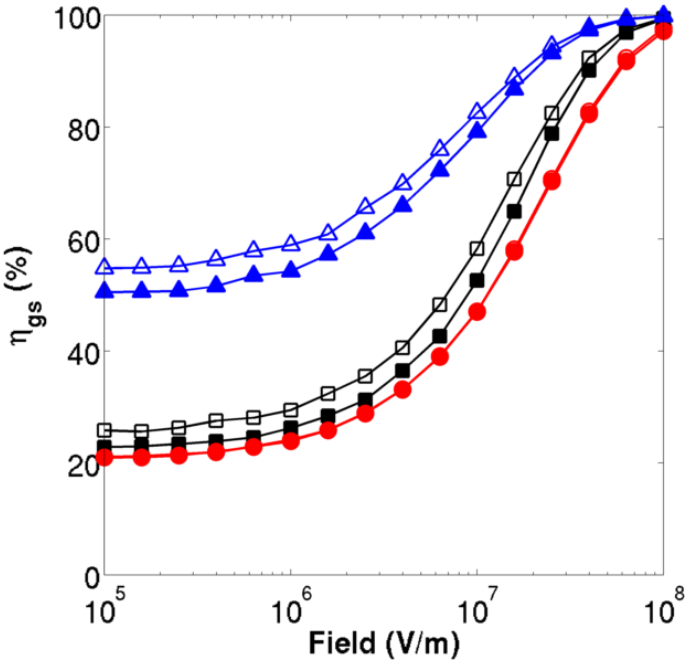

Figure 4.2: η_{gs}(F) for $\sigma = 50$ meV. Symbols and lines as for Figure 4.1.

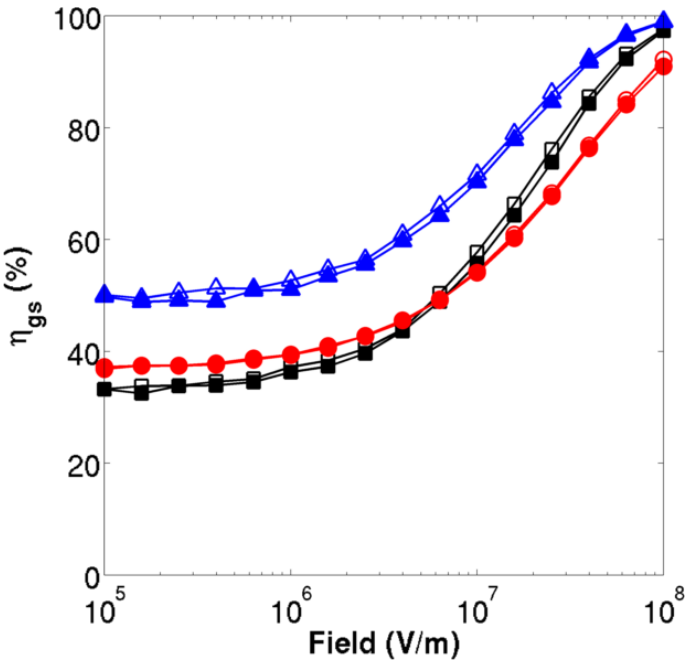

Figure 4.3: η_{gs}(F) for σ = 100 meV. Symbols and lines as for Figure 4.1.

4.4 Results

4.4.1 General trends

Figures 4.1, 4.2 and 4.3 show η_{gs}(F) for F = 10^5 to 10^8 Vm^{-1}; for σ = 0, 50 and 100 meV respectively. For all three mobility combinations, N_h = 0, 1 and 10, a similar general trend is seen for all levels of disorder. In each case, η_{gs} is saturated at small fields, increases at a rate of $\approx \exp \frac{F}{F_0}$ (where F_0 is a constant) at intermediate fields, and saturates again close to 100% at high field.

Where the values from the two methods differ, the FRM always underestimates η_{gs}. This can be explained by careful evaluation of the different ways in which the two methodologies will handle geminate pair dynamics. Following exciton dissociation, a newly formed geminate pair will straddle the heterojunction, and events for both the electron and hole will be calculated ($\varrho_{e1}, \varrho_{h1}$). If the electron event has the shorter waiting time, ϱ_{e1} will be executed first, and a new event found for the electron in question. By the time ϱ_{h1} is executed, the local system, particularly the local field, may have

changed considerably from its state at formation. For instance, the first event may be for an electron to hop perpendicularly away from the interface, increasing the distance between the geminate pair by a factor of at least two, depending on the range of the hop. However, in terms of the local field, the hole will still 'see' the electron in its original location, adjacent to the interface, and will not be aware of the significant reduction in field that has just occurred. It is therefore more likely to remain close to the interface, whereas in the exact method the reduced field may have allowed it to hop away. In the FRM, the hole will only see the new state of the system after it has itself hopped. The pinning of the hole close to the interface due to being unaware of the movement of the electron will then draw the electron back again. Clearly, therefore, using the FRM increases the probability of geminate recombination, leading to the observed lower values of η_{gs} using this method.

It can be seen that the offset between the values produced by the two methods is a function of both disorder and mobility, a result which will be analysed in Section 4.4.2, below. The relative positions of the curves for different values of N_h also appears to be disorder dependent, and this is discussed with specific reference to low-field trends in Section 4.4.3. In general, the agreement between the two methods improves as the global field ($\underline{\mathrm{F}}$) increases. As the key difference between the two methodologies is in their calculation of the local field, this result is to be expected, as the significance of the local field diminishes as the global field increases, ultimately reaching the point where the global field alone is sufficient to drive all charge pairs to separation, and so $\eta_o \rightarrow 0$ as $\eta_{gs} \rightarrow 100\%$.

4.4.2 Field averaged offset, η_o

In order to more thoroughly investigate $\eta_{gs}(\sigma)$, these data have been replotted as field-averaged values of $\eta_o = [\eta_{gs}(FRM) - \eta_{gs}(exact)]$.

Nearest neighbour hopping

Figure 4.4 shows that, with one carrier trapped ($N_h = 0$), the two techniques agree perfectly, within the noise of the simulations (0.31%). This is to be expected, as when

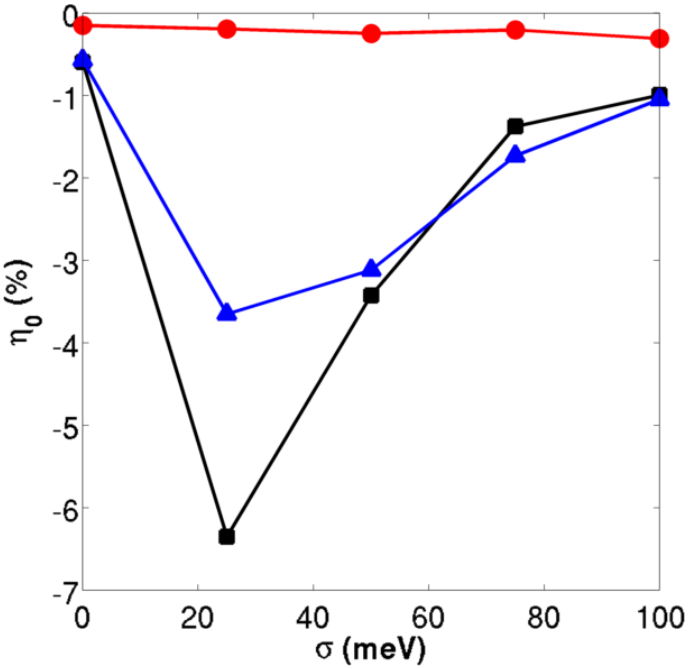

Figure 4.4: $\eta_0(\sigma)$ for $\xi = a$. Symbols and lines as for Figure 4.1.

one carrier is immobile, there are no changes in the local field for the other one to take account of, and so the FRM and exact methodologies are identical - there is only one mobile charge and it is updated at every timestep.

When $N_h = 1$, the values agree to within $\approx 0.6\%$ at 0 meV. η_o then increases to peak at $\approx 6\%$ at 25 meV, before decreasing again to drop below 1% when disorder exceeds 100 meV. This peak value of $\eta_o = 6\%$, although high, is not seen as a terminal flaw in the FRM methodology as applied to polymer blend solar cells. The justification is that the disorder values reported for the materials of interest are generally > 50 meV (see Section 6.2.2), and, furthermore, the agreement is much better at the field values relevant for short-circuit and maximum power point (MPP) behaviour.[1]

Nevertheless, these trends demand explanation. Following dissociation, both charges have a number of possible routes to separation and ultimate escape, starting with any one of five possible hops either parallel or perpendicular to the heterojunction. At $\sigma = 0$ meV, there is no energetic barrier to any of these routes, the hopping rate is

[1]Assuming a typical PFB:F8BT device of 130 nm thickness, with $V_{bi} = 1.3$ V, the SC field will be 1 $\times 10^7$ Vm^{-1}, with the field at V_{MPP} typically no less than half this [90].

a function of the local and global fields alone. As disorder increases, the creation of energetic barriers of increasing height between sites can render one of more of these routes highly unlikely, reducing the number of probable pathways to escape. As this continues, charge separation become reliant on progressively fewer transport pathways, and the simulation becomes more sensitive to any mistakes in calculating the local field, thus increasing η_o. Reliance on progressively fewer *energetic* pathways is analogous to simulating blend devices of varying interfacial area, where increasing the interfacial area of the morphology forces the charges to become reliant on progressively fewer *physical* pathways to escape.

As σ increases further, η_o begins to decrease again. This seems counterintuitive, as the magnitude of the aforementioned effect will continue to increase. As disorder builds, the relative proportion of neighbours of higher energy (necessitating an 'uphill' hop) to those of lower energy at any particular site will remain the same on average (1:1 in the centre of the DOS). However, the spread of these neighbour energies will increase, so that even favourable (energetically downhill) routes will have large reaction rate differences between them, reducing the likelihood of choosing anything but the most energetically downhill hop. All this should increase η_o. The clue as to the origin of its decrease lies in comparison with the scenario where one carrier is immobile ($N_h = 0$), which, as has already been seen, produces the result that $\eta_o \approx 0$. Even when both carriers are mobile, a high level of energetic disorder can lead to one of them becoming trapped for large timespans during the simulation. Therefore, as disorder increases, the simulations where both carriers are mobile will begin to resemble those where one carrier is completely trapped, leading to a decrease in η_o.

$N_h = 10$ simulations display a similar trend to $N_h = 1$, but the peak value of η_o is now only 3.6%. Although η_o peaks at 25 meV in both sets of simulations, interpolation reveals that the true peak is at a value around 10 meV higher in the $N_h = 10$ simulations. For a given amount of disorder, higher mobility charges will be less restricted in terms of extraction routes, explaining both why the peak value of η_o is lower, and also why it appears to occur at a higher level of disorder. Furthermore, higher mobility charges are less likely to become trapped, explaining why η_o is marginally higher at 75 and 100 meV.

Increasing the hopping range

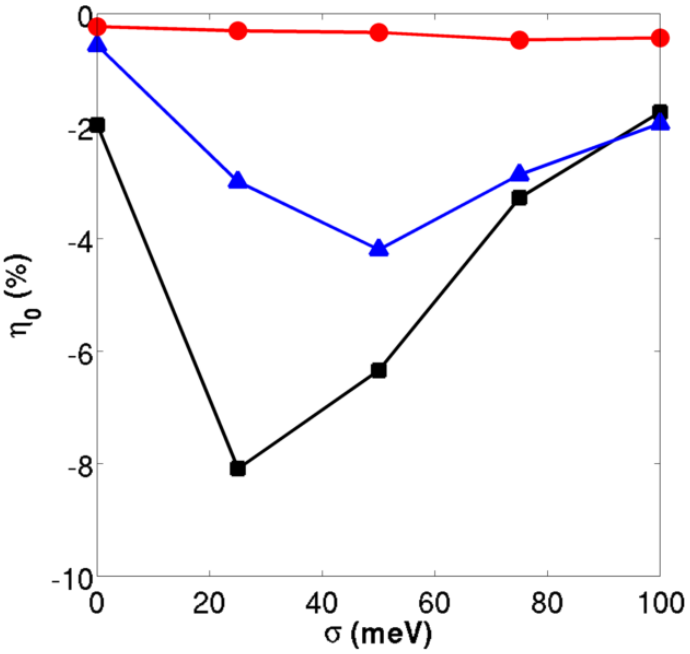

Figure 4.5: $\eta_o(\sigma)$ for $\xi = 2a$. Symbols and lines as for Figure 4.1.

In Figure 4.5, the charge hopping range has been increased to ξ = 2a. For $N_h = 1$, the result is that the magnitude of η_o increases for all values of σ, which now peaks at 8.1% at 25 meV. This is to be anticipated, as the increased hopping range means the field changes unaccounted for by the FRM are now greater. Proportionally, however, the increase in η_o when moving from 0 to 25 meV disorder has decreased from a factor of 10 to a factor of 4. Therefore, the effects of energetic restriction on the number of probably escape pathways has been reduced; an intuitive result given that the number of available neighbours for hopping to has been increased, and that the proportion of these neighbours that are not adjacent to the interface has increased from 1/6 to 5/18. Again, higher mobility charges are less susceptible to these effects, and the peak value of η_o for $N_h = 10$ is now at 50 meV, continuing the trend discussed above.

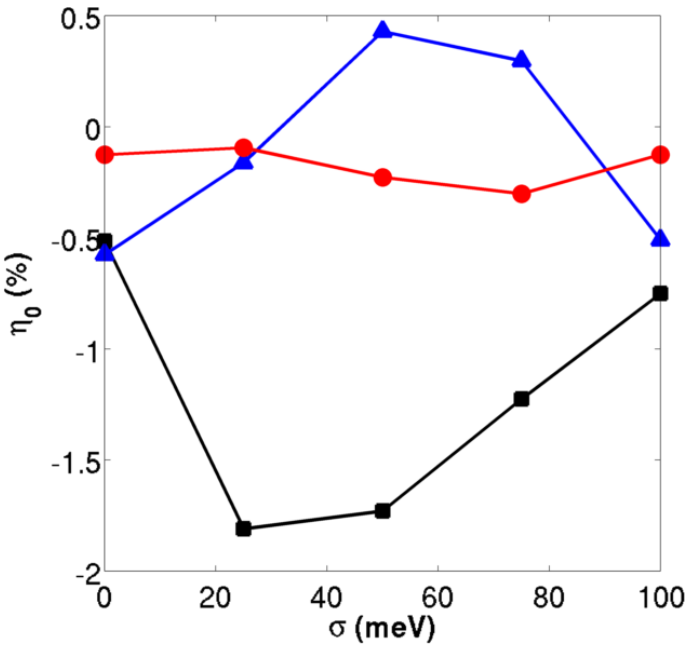

Figure 4.6: $\eta_0(\sigma)$ when using correlated disorder. Symbols and lines as for Figure 4.1.

Correlated disorder

The ξ = a simulations were repeated with the energies of the six nearest neighbours correlated using the method of Gartstein and Conwell [82], with ξ_c = a (energetic correlations are explored in more detail in Section 6.2.3). The results are shown in Figure 4.6. At 0 meV, there is no disorder to correlate, and so the results here should be the same as for the uncorrelated simulations. This, therefore, gives a measure of the uncertainty for these simulations. In this case, the greatest difference between the two sets of simulations is 0.08%, at $N_h = 1$. Another measure is the $N_h = 0$ values, which peak at 0.23%.

The results show that the value of η_o becomes less negative across all values of N_h and σ. Correlating the disorder lowers the energetic barriers between neighbouring sites, whilst maintaining the same overall distribution of site energies. This reduces the aforementioned effect of restricting the number of extraction pathways, in much the same way as increasing the number of neighbours does, thus reducing the effect of approximations in calculating the local field, reducing the magnitude of η_o. However, unlike the scenario where the number of neighbours is increased, the changes in the local

field are still relatively small, explaining why η_o takes its lowest values in these results.

However, when $N_h = 10$, η_o becomes positive for disorder levels of 50 and 75 meV. The magnitude is small ($\approx 0.4\%$), but above the noise level established above, showing this must be a real effect, generated by a mechanism not yet accounted for. It has already been seen (vide supra) that the approximation inherent to the FRM can result in increased geminate recombination. However, this is not the only difference between the FRM and the more exact method. One of the essential precursors to geminate recombination after initial separation is charge tracking along the heterojunction due to coulombic attraction (this is explored further in Sections 5.4 and 5.5). A consequence of using the FRM for modelling a geminate pair is that each charge is unaware of the actions of the other until its next hop. If the electron hops in the +y direction, the hole will be unaware of this until after its next hop, which is based on the previous state of the system. Only then would it see the new location of the electron and perhaps begin to track it. Therefore, each charge can be considered to be at least 'one step behind' when tracking the other. As tracking is essential to recombination, η_o can actually be *increased* by this scenario, to the extent where it can even become positive. This effect may be present for some or all of the previous results, but it is impossible to isolate from other effects. The reason it is sufficiently strong here to raise η_o to positive values when $N_h = 10$ is the minimisation of effects that reduce η_o, as already noted, and the enhanced tracking that occurs when mobilities are imbalanced.

4.4.3 Low field η_{gs}

The effects of disorder upon η_{gs} at low field are also examined, as this is relevant for establishing the open-circuit voltage of a device, and also yields unexpected trends that warrant explanation and provide further insight into the mechanisms governing geminate separation and hence device efficiency. Figure 4.7 shows η_{gs} for F = 10^5 Vm^{-1}, for ξ = a, and for a second scenario, where the e-h pairs are generated by excitons created throughout the device, which will hence explore the DOS before dissociating.

It might be expected that increasing σ would result in a decrease in η_{gs} due to the associated reduction in mobility. However, as the results show, the situation is more complex than this. With one carrier trapped, an *increase* in $\eta_{gs}(\sigma)$ is in fact observed for

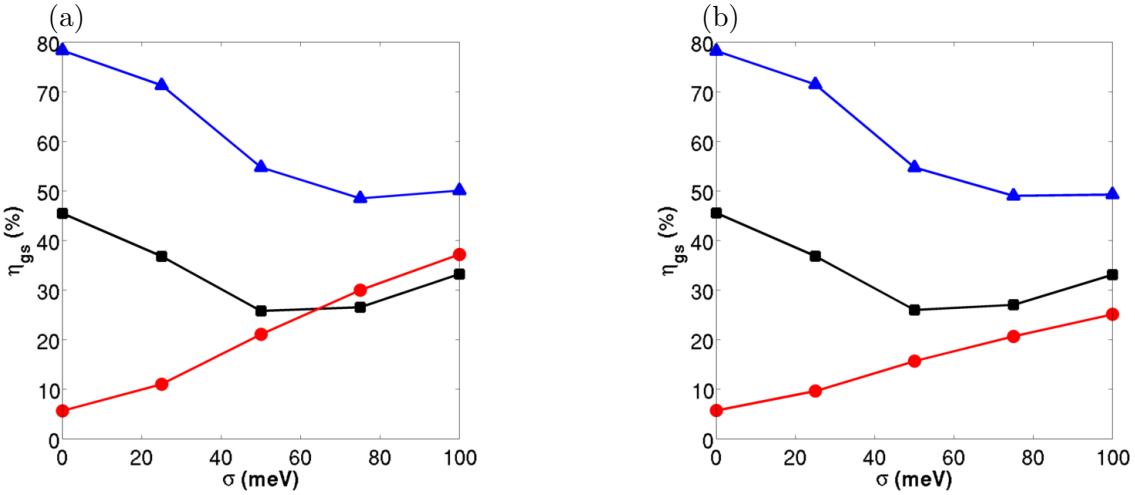

Figure 4.7: $\eta_{gs}(\sigma)$ at low field (F = 10^5 Vm^{-1}), for ξ = a (a); and when the e-h pairs are generated by excitons (b). Symbols and lines as for Figure 4.1.

the two simulation scenarios. This can be attributed to equilibration. In the simulation, charge carriers are created at random pairs of sites along the heterojunction, positioning them randomly within the DOS. When placed within a Gaussian DOS, carriers ordinarily relax towards tail states, and would eventually saturate at an energy known as the equilibration energy, if allowed to hop for long enough. It was shown by Bässler [30] that the value of the equilibration energy is,

$$\varepsilon_\infty = -\frac{\sigma^2}{k_B T} = -\sigma\hat{\sigma} \tag{4.2}$$

When carriers are adjacent to each other, such as immediately following dissociation, they can be considered to be in a 'recombination scenario', where recombination is one of the competing options open to them. As disorder increases, the waiting time for all hops away from this scenario is increased (the mobility is lowered), while the recombination rate k_r remains constant. It might be expected that charges in a recombination scenario are therefore increasingly likely to choose recombination as disorder increases. However, when one carrier is trapped, the excess energy of the free carrier above its equilibration energy allows it to quickly escape this scenario without the other carrier tracking its position parallel to the interface. Thus, the higher the disorder, the greater the excess energy of the carrier above the equilibration energy, and the higher the separation probability, explaining the increase in $\eta_{gs}(\sigma)$ when $N_h = 0$. As recombination is modelled as

a fixed rate process, excess carrier energy can only ever enhance separation, as it will always drive the charges away from their starting positions and out of the recombination scenario.

When both carriers are mobile, equilibration effects will still occur, but with the charges now able to track each other, their probability of re-entering a recombination scenario following initial escape is greatly increased. Initially, this results in a decrease in $\eta_{gs}(\sigma)$. However, as σ increases further, the reduction in mobility will also reduce tracking, whilst the effects of equilibration continue to increase. Eventually equilibration champions both competing effects (the reduced likelihood of escaping a recombination scenario due to disorder, and the ability to re-enter a recombination scenario due to tracking), and the monatonic increase of $\eta_{gs}(\sigma)$ is recovered beyond $\approx$ 50 meV for $N_h = 1$ and $\approx$ 75 meV for $N_h = 10$. In other words, equilibration still occurs, but with the carriers able to track each other, more energy is required for its effects to become apparent. A higher mobility requires a greater excess energy before the effect becomes noticeable, explaining the latter result.

Turning to Figure 4.7 (b), the results where the charges are created following exciton diffusion and dissociation and very similar to (a), but the rate of increase of $\eta_{gs}(\sigma)$ when $N_h = 0$, i.e. when equilibration is most apparent, is reduced. As excitons diffuse, they will gradually equilibriate, with the result that the sites on which they dissociate are not at random locations in the DOS, but are, on average, at energies below the average. The resulting charge pair will thus be created at sites closer to the equilibration energy, with the result that a greater value of σ is required to create a particular value of η_{gs}. This idea may be continued, by creating charge pairs at their equilibration energy, meaning they contain no excess energy with which to separate. Simulations performed by Chris Groves show that, under this scenario, η_{gs} decreases across the complete σ range, for all values of N_h.

In PV devices, the net difference between the built-in and applied bias close to open circuit is very small, resulting in a small field. Therefore, this section potentially provides insight into means of reducing geminate recombination close to open circuit. This might even extend the open-circuit voltage, as a greater current will be produced at any given (low) field value. However, these results only address geminate recombination, not bimolecular, and so minimisation of η_{gs} won't necessarily result in an overall increase in efficiency. More significantly, however, these results suggest that increasing the exciton

diffusion length in polymer blend solar cells, such as by careful engineering and choice of polymers, may not create the anticipated increase in device efficiency. A greater diffusion length means that excitons will explore more of the DOS prior to dissociation, meaning the charges will form on lower energy sites, increasing the level of trapping and hence geminate recombination.

4.5 Summary and conclusions

The results have shown that the First Reaction Method agrees excellently with the more exact method of simulation, across nearly all values of field, disorder, and for the three mobility combinations simulated. Significant deviation between the two methodologies only occurs at field and/or disorder levels than are much lower than those under which a polymer blend photovoltaic will operate, and even then the difference peaks at only $\approx$ 8%. This validates the First Reaction Method for using in polymer blend photovoltaic simulations, and as such it will be used, where applicable, throughout this thesis.

In terms of the field-averaged offset between the two methods, η_0, the following conclusions can be drawn:

1. The FRM usually underestimates the probability of a geminate charge pair attaining final separation, η_{gs} (i.e. η_o is negative). This is because it does not take into account changes in the local field that arise following the movement of the first charge to leave the interface, therefore potentially pinning the second charge to the interface, drawing the first one back again. The exception is when one carrier is trapped, i.e. $N_h = 0$, as the FRM and exact methods become identical under these circumstances.

2. Increasing the disorder increases this offset (η_o becomes more negative), as charges become reliant on progressively fewer energetic pathways to facilitate their extraction from the device.

3. Increasing the disorder still further reduces this offset again (η_o becomes less negative), as carriers start to become trapped for large timespans during the simulation, creating a scenario similar to where $N_h = 0$.

4. Increasing the hopping range to $\xi = 2$ increases the offset due to approximations in calculating the local field, as field changes following an event may be larger, thus increasing the magnitude of the effect described in (1) (η_o becomes more negative).

5. However, for $\xi = 2$, the relative change in $\eta_o(\sigma)$ is smaller, as there are more pathways to escape. Therefore the effect described in (2) is lessened (η_0 becomes less negative).

6. Having a greater number of pathways to escape also decreases the likelihood of long-term trapping at higher disorder, lessening the magnitude of the effect described in (3) (η_o becomes more negative).

7. Correlating the disorder reduces the size of energetic barriers between sights, lessening the magnitude of the effect described in (2), in a manner analogous to that described in (5).

8. When $N_h = 10$, correlating the disorder can actually raise η_o to positive values. This is in contrast to the mechanism described in (1), and is due to reduced charge tracking in the FRM.

Furthermore, the analysis of low field characteristics provides insight into the geminate recombination mechanism, and how it is affected by mobility imbalance, disorder, and carrier trapping.

Chapter 5

Investigating the morphology of polymer blend photovoltaics

Much of the work contained herein has been published in *Physical Chemistry Chemical Physics* **12**, 844-851 (2010).

5.1 Introduction

Monte Carlo modelling is ideal for exploring the precise role of the nanomorphology in determining the efficiency of a photovoltaic device. This is because it is possible to build up a morphology on the scale of the lattice constant, enabling the observation of how each physical process interacts with that morphology on the same scale. At any particular voltage, the internal quantum efficiency and current density of the device can be calculated, and by extending simulations to encompass a range of voltages across the device, the power conversion efficiency and fill factor can also be found. By first reproducing experimental J-V trends for blend morphologies, the Monte Carlo model can be validated, and subsequently used to predict the experimental impact of changing a number of parameters, as well as to establish the precise role of the morphology in determining that impact. Drift-diffusion models are unable to take full account of the effect of three-dimensional structures, which are of interest here, instead reducing the complex morphology to a basic homogenous description or a simplified two-dimensional structure. They also do not normally take full account of the related process of exciton dissociation, which has multiple stages that are critically influenced by morphology [48, 41].

The disordered structure and lack of reproducibility of polymer blend solar cells have often been identified as severe limitations to their performance. The customary 'shake and bake' production process described in Section 3.2.1 creates highly unpredictable morphologies, containing disconnected islands of polymer that act as recombination centres, as well as tortuous and disconnected charge transport pathways, leading to high losses through charge recombination. It is desirable to find a means of creating ordered morphologies, that have short, bicontinuous electron and hole charge transport pathways to facilitate good charge collection; as well as a high interfacial area to enhance exciton dissociation. Triply-periodic minimal surface structures fulfill these morphological requirements, and the possibility of their self-assembly in photoconductive polymers overcomes the experimental difficulty in reliably creating nanoscale structures by other means. The generation of morphologies by self-assembly also makes such structures more reproducible [63, 91, 92]. Recently, interest in such structures has greatly increased[1], and they therefore serve as a useful and interesting addition to any exploration of solar cell morphology. The nature of these structures, as well as their potential use in solar

[1] See section 5.2.3 for details.

cells, is described below.

5.2 Bicontinuous, triply-periodic minimal surface nanostructures

5.2.1 Minimal surfaces

Minimal surfaces are surfaces of zero or 'vanishing' mean curvature, i.e. they are equally convex and concave at all points. A trivial example of a minimal surface is a plane. Other examples include the helecoid and catenoid. In nature, these surfaces form as the interface between two immiscible constituents. They are termed 'minimal' as they represent the smallest surface area achievable under certain constraints, the nature of which are particular to the system in which they form. Any system initially formed in a high energy state, e.g. by mixing two chemicals, will attempt to lower its free energy. If the constituents are chemically repulsive, it will achieve this by minimising the interfacial surface area where they are in contact, and in doing so the shape of the surface will explore geometric space. A simple way to generate a minimal surface is to dip a wire frame into soapy water. Under surface tension, the soap film minimises its area to form a catenoid [93]. In block copolymers, the constraint is the covalent bonds between blocks.

Triply-periodic minimal surfaces are invariant under translation in three independent directions, i.e. they have three lattice vectors. A triply-periodic minimal surface is the boundary between two labyrinthian-like solid regions that are themselves triply-periodic. This justifies the term bicontinuous [94]. The periodicity of the structures justifies generation by means of a unit cell, which is also the basis for any analysis of the structure. Structures with a triply-periodic minimal surface geometry form in a number of systems, including lipid-water systems [95], dendrimers [96] and diblock copolymers. It has even been shown that such phases can even freely self-assemble from pear-shaped hard particles, driven by entropy alone [97]. It is the formation of such geometries in block copolymers that is of interest here.

5.2.2 Block copolymers

Homopolymers consist of a chain of a single monomer type A_n. Copolymers contain two monomer types, A and B. They can be joined in random combinations, or in block formations, consisting of chains of one type covalently bonded to chains of the other. When joined linearly, common combinations include the diblock formation (AB), the triblock/terblock formation (ABA) and the multiblock formation $(AB)_n$, though joining can also be branched [98]. Adding a third monomer type (C) creates terpolymers, and so forth. The large number of molecular topologies that can be created in this way leads to an enormous variety of morphologies and physical properties of the resulting material. Block copolymers are a form of soft matter - they are characterised by local disorder and long-range order. Examples of their use include upholstery foam, adhesive tape and asphalt additives, used to reduce pavement cracking [98]. Chemical incompatibilities between the two blocks produces excess free energy that make mixing unfavourable. Thus, as the system tries to lower its energy, microphase separation will ensue. If there are no constraints, macrophase separation will follow, such as the separation of oil and vinegar in a salad dressing or the formation of large structures in typical polymer blends during annealing. However, the covalent bonds in diblock copolymers limit separation, counterbalancing the thermodynamic forces driving it. To keep the molecules of the diblock copolymer apart, the chains must adopt extended configurations. However, the number of configurations accessible to extended chains is far more limited than to those in their native coiled state. As the systems tries to minimise its free energy, it will explore this limited configuration space, and adopt a geometry that represents the lowest free energy achievable, that with the minimal surface. The most likely configuration depends on composition and molecular weight [98, 92].

Some of the configurations that can form include spherical, cylindrical, lamellar and gyroid morphologies [98, 99]. The gyroid configuration itself is ubiquitous in natural and synthetic self-assembled materials [100]. It was first identified in lipid-water systems by Luzzati in 1967 [95], named in 1970 by Schoen [101], and first discovered in diblock copolymers by Hajduk in 1994 [102]. It is a cubic morphology and forms because it contains the least curved microdomain interfaces of the various cubic morphologies available to the system, therefore best satisfying the compromise between chain stretching and interfacial tension, representing an 'optimised state of frustration'. It almost never forms in organic crystal structures, suggesting the short-range liquidlike disorder common to

soft matter is near-essential to the formation of this high-symmetry molecular packing [98].

5.2.3 Self-assembled solar cells

If such structures could be formed in polymer blend solar cells, there is the potential to create devices with efficiencies that exceed those achievable using disordered blend morphologies. The dimensions of the geometries formed in copolymers are appropriate to solar cell devices, with feature sizes of the order of the exciton diffusion length, L_x [63, 98, 99]. The cylindrical configuration, if it could be made to be vertical with respect to the electrodes, would be similar to the rod morphology already proposed for solar cell devices, and simulated in this chapter.

Gyroid morphologies have been created in nanoporous silica films by Urade *et. al.* [103]. Bulk heterojunction solar cells made from a porous titania structure synthesised using a poly(styrene-block-polyethylene oxide) diblock copolymer template infiltrated with a semiconducting polymer were made by Oey *et. al.* [104], who noted that gyroid structures could be created by this technique. Recently, gyroid and columnar structures were replicated in anatase titania and the titania structures immersed in dye and back filled with a liquid electrolyte to create dye-sensitised cells (DSCs) [105, 106]. These cells show power efficiencies of around 2%, considerably less than the best efficiencies of 11% obtained for liquid electrolyte dye-sensitised cells made from mesoporous titania [107], but comparable to devices of a similar thickness. To date, triply-periodic minimal surface nanostructures have yet to be adopted in an all-conjugated polymer solar cell, although diblock copolymers based on conjugated polymers have now been synthesised [108]. Jenekhe *et. al.* have used the self-assembly of nanowires in P3BT/PC_{71}BM devices to increase the efficiency by over an order of magnitude. In this work, the need for truly nanoscale modelling in order to understand and develop this idea was emphasised [109].

5.3 The purpose of this chapter

The aim of the work contained in this chapter is to fully investigate the role of morphology in determining organic solar cell efficiency. In doing so, the theoretical change in efficiency due to introducing triply-periodic, bicontinuous minimal surface nanostructures as device morphologies will also be evaluated. The use of such morphologies is considered a novel adaptation on the existing bulk heterojunction approach, and are henceforth referred to as the 'novel' morphologies for brevity. Three common bicontinuous phases will be simulated: the gyroid, double gyroid and double diamond. The double gyroid is a close structural model for the well-known gyroid phase in diblock copolymers [110], a phase that had previously been identified as the double diamond [111]. The single gyroid is not found in diblock copolymers, but has been identified in linear terblock copolymers ([112], although not with volume fraction 50%), and as the nanostructure of the wings in certain butterfly species [100]. The feasibility of these structures as active layer morphologies will be assessed in comparison to two other classes: the disordered blend and interdigitated vertical rod morphologies. The interdigitated structure used is similar to the cylindrical phase described above. These structures are illustrated in Figure 5.1, and details on how each is generated can be found in Section 3.2.1. Each morphology will be evaluated in terms of complete J-V performance and its constituent processes across a range of parameters.

Although each of the novel structures examined is known to form in diblock or terblock copolymers, in order to be useful for organic electronics, the polymers forming the self-assembled structures would have to be conjugated, thus satisfying the semiconducting properties required for both solar cells and OLEDs. One block would function as the donor, the other as the acceptor. The polymer backbone in conjugated polymers is thought to be too rigid for phases such as the gyroid to form, and to date they are yet to be observed. S. Sun has suggested the use of a flexible non-conjugated bridge unit in order to overcome this problem (see, for example, [113, 114, 92, 63]). However, the emphasis here is on the usefulness of bicontinuous structures in general, of which the three examined here are merely examples, due to the recent development in interest in them, and should a means of creating them be developed in the near future. All three share the essential traits of island-free continuous charge transport pathways with a high interfacial area, which should provide interesting further insight into the nature of the morphological dependence of PV efficiency, as well as generating a clear performance

improvement on existing disordered blend structures.

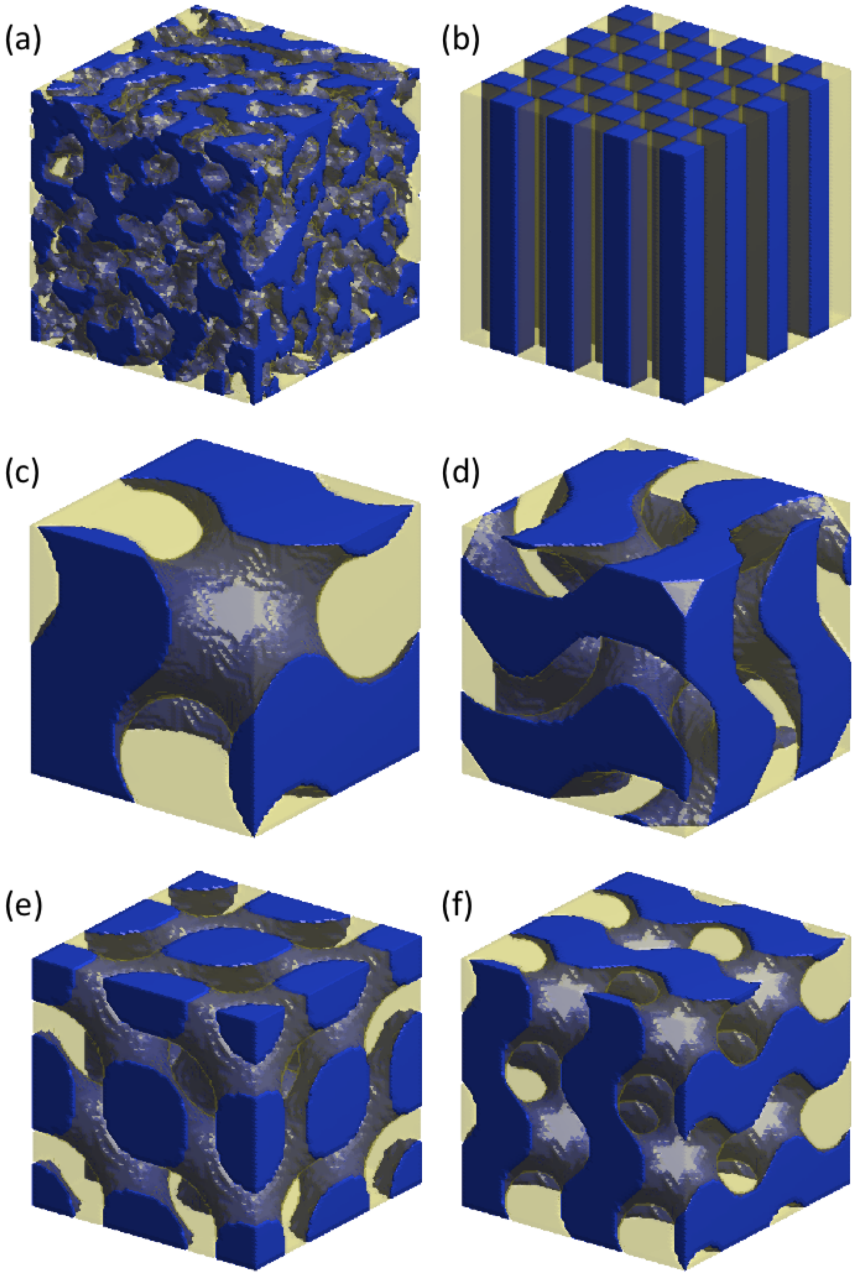

Figure 5.1: Disordered blend (a) and interdigitated rod (b) structures. Panels (c-e) show a single cubic translational unit cell of the single gyroid with symmetry $I4_132$ (c), the $Ia\bar{3}d$ double gyroid (d) and the $Pn\bar{3}m$ double diamond (e) structures. Panel (f) shows an extended gyroid structure consisting of 2^3 translational unit cells of the structure in (c) with half the lattice length a.

5.4 Results and discussion

The following simulation parameters are used throughout this chapter, unless otherwise specified:

k_r	1×10^6 s^{-1}	[77]
λ	1.2×10^{-19} J	[41]
ε	4	[77]
σ	62 meV	[77]
μ_0	1×10^{-7} m^2 (Vs)$^{-1}$	[115, 116, 117]
V_{bi}	1.3 V	[118]

Table 5.1: Parameters used in the model, unless otherwise specified.

The exciton diffusion length used was 3.53 nm [2].

5.4.1 General trends

Figure 5.2 shows the results of simulations on a set of blend morphologies, with feature sizes (the typical width of connected sections of the same polymer, defined by Eq. 3.11) ranging from $l_f = 2$ nm to $l_f = 32$ nm. The trends shown here are representative of all the morphology groups examined, as can be seen in section 5.4.3, hence the discussion that follows is applicable to the other morphologies as well. All of the trends observed here are consistent with experimental findings [64]. However, in this chapter an exact quantitative reproduction of experimental parameters has not been attempted, and so exact efficiency values will not be compared with experiment, with the exception of optimum feature size, as discussed below.

Exciton dissociation efficiency (n_{ed}) drops off steadily with feature size, falling from 1.0 (all excitons dissociated) for the 2 nm feature size morphology, to 0.33 for the 32 nm morphology. As feature size increases, so does the mean distance between heterojunctions, reducing the probability of an exciton reaching a heterojunction before recombining. Over the same range charge collection efficiency (n_{cc}) shows an increase from 0.24 to

[2] A mistake was made in the original simulation coding, which resulted in this diffusion length instead of the intended 6 nm. However, it is the trends that are being examined here, not the precise values obtained; and the role of the exciton diffusion length is addressed specifically in section 5.4.2, below.

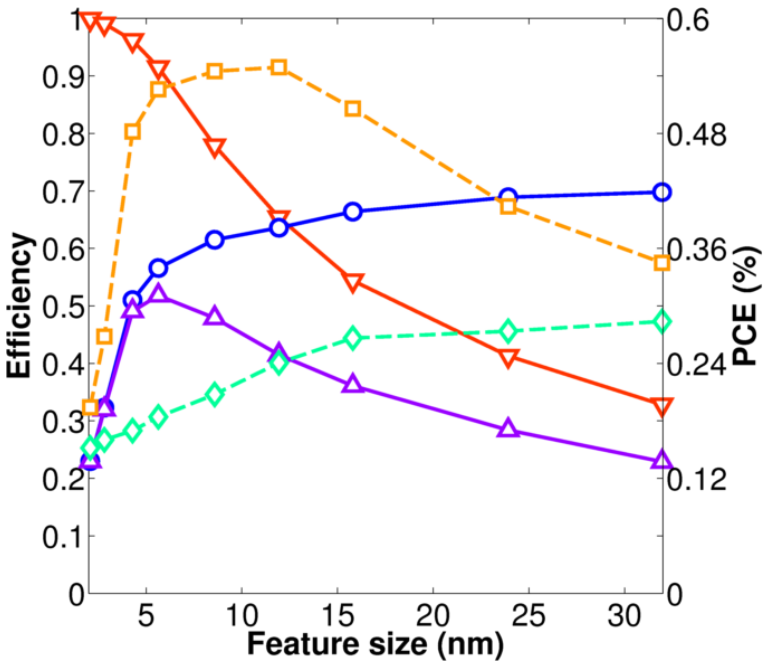

Figure 5.2: Results for blend structures, as a function of feature size. Showing n_{ed} ($\bigtriangledown$); n_{cc} ($\circ$), IQE ($\bigtriangleup$), FF ($\diamond$) and PCE ($\square$)

0.70, though the majority of this rise is at the smallest feature sizes, beyond which it reaches a plateau, similar to other theoretical studies [41]. Broadly speaking, this increase is due to the widening of the charge transport pathways that occurs as the morphology evolves, which reduces the probability of recombination. However, a more detailed analysis of the contributions made to this result by geminate and bimolecular recombination is required to fully explain these observations, and this is provided in section 5.4.4. The internal quantum efficiency (IQE) peaks at 0.55 for the $l_f = 5.6$ nm morphology. The existence of an idealised intermediate morphology such as this, where the product of η_{ed} and η_{cc} is optimised, is now well established in both theory and experiment [64, 119, 32, 65].

By stepping the applied bias for each morphology up from 0 V (short circuit) to 1.4 V (where V $>$V$_{bi}$), it is possible to discover the fill factor and power conversion efficiency for all the morphologies. These are plotted alongside the other measures of efficiency. For the sake of simplicity, in this section it has been assumed that $V_{OC} = V_{BI} = 1.3\ V$ [118], as any variations from this value are insignificant for these parameters. Fill factor can be seen to increase steadily with l_f, in agreement with experiment [64, 120, 121].

This occurs because fill factor is essentially a measure of the device's ability to collect current, and so increases for larger l_f where n_{cc} is also larger. A larger current collection efficiency is an alternative way of saying the device has a lower series resistance, which is known to increase fill factor [3]. Analysis of recombination trends, given in section 5.4.4 below, allows a fuller description of the microscopic origin of this trend.

Finally it can be seen that, like the IQE, the PCE peaks at an intermediate feature size, but that the optimum feature size as determined by this measure of efficiency is larger than that deduced when analysing IQE alone (devices at short-circuit). The defintion of PCE shows that it will be biased by the morphological dependence of the fill factor, discussed above, leading to this result. Thus, a morphology optimised for short circuit current will not be the optimal morphology for power conversion. Although a somewhat trivial result, this characteristic does not appear to have been identified in the literature, and is significant as it affects the choosing of the optimum morphology for solar cell operation.

5.4.2 Domain purity

In the results presented above, the IQE peaks at a feature size of 5.3 nm, similar to the exciton diffusion length of 3.53 nm. These results are sensitive to device parameters [32], many of which are only known approximately as they depend on chain alignments, for example the dissociation rates [122] and charge mobilities [39], and these alignments will vary widely in the disordered films. Another problem is domain purity, as minority components in the blend domains can have a sizeable impact on the results because they act as dissociation, and hence recombination, centres. For polymer solar cells, it is generally accepted that the peak efficiency occurs where $l_f \approx L_x$, as found above. However, more recent and detailed experimental studies have found that the domain size of an optimised morphology can exceed the exciton diffusion length by a factor of more than two [64], even though domain purity >90% is common in these polymers [123, 124]. To investigate this discrepancy, the calculations of IQE in the blend morphologies were repeated, this time creating additional islands, to represent impurities, by randomly swapping voxels in the domains of each polymer, and then plotting the results against the original feature sizes. This mimics experiment, where the islands are invisible under AFM, and so mean domain size is potentially overestimated when

compared to a computer calculation. Additionally, the common result that $l_f \approx L_x$ for polymer solar cells implies a linear relationship between the two, an assumption which will be tested below.

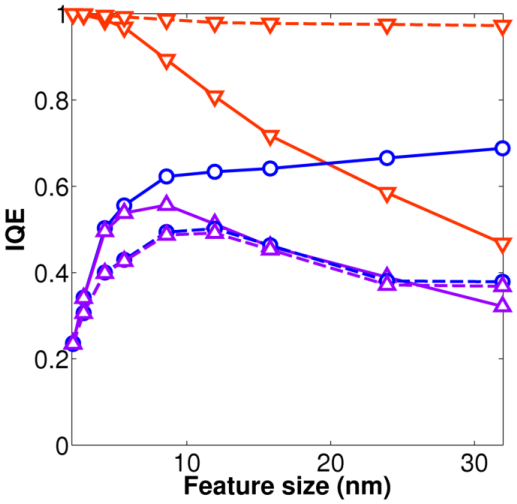

Figure 5.3: η_{ed}, η_{cc} and IQE for 100% (solid lines) and 95% (dashed lines) purity. Symbols as for Figure 5.2.

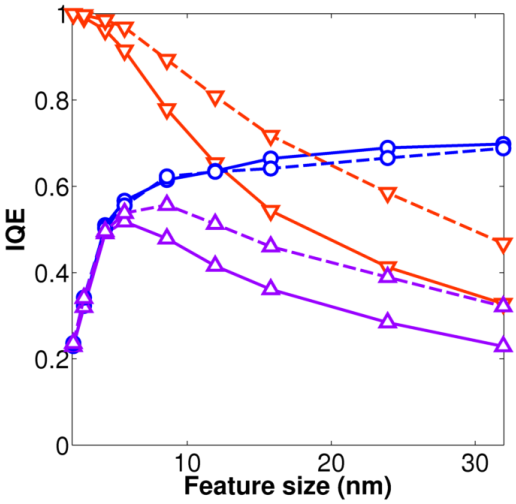

Figure 5.4: η_{ed}, η_{cc} and IQE for diffusion lengths of 3.53 nm (solid lines) and 6.0 nm (dashed lines). Symbols as for Figure 5.2.

The results for 100% and 95% purity are plotted in Figure 5.3. It can be seen that the addition of impurities reduces the rate of decrease of $\eta_{ed}(l_f)$. In terms of efficiency, most of these additional excitons will be wasted, as they will dissociate at disconnected islands and therefore cannot contribute to the IQE. However, the random placement of the islands means a few will be connected to existing charge transport pathways, increasing their interfacial area. This results in a modest increase in IQE at some feature sizes. However, by far the more important change that results from the impurities is that η_{cc} no longer increases monotonically with l_f across the range of morphologies, but now shows an intermediate peak. This occurs because as l_f increases, the interfacial area of the charge transport pathways decreases and exciton dissociation proportionally takes place more at the disconnected islands (the number of which are fixed), reducing overall charge collection efficiency.

Table 5.2 shows the full results of this study. Interpolation has been performed to better identify the point of peak efficiency for each morphology, due to the disparate nature of feature size simulation. The table shows the polymer purity, the apparent feature size at

which the IQE peaks, the ratio of this feature size to the exciton diffusion length (3.53 nm), and the peak IQE value itself. The addition of impurities does indeed shift the *apparent* optimum feature size to higher values, as anticipated. The peak IQE values decrease with impurities, as islands waste excitons and impede charge flow. The most interesting result is that decreasing the polymer purity by just 5% results in the IQE peaking at an apparent feature size more than twice the exciton diffusion length.

Purity	**Peak of IQE**	**Ratio**	**IQE**
100%	5.3 nm	1.50	0.52
99%	6.1 nm	1.73	0.49
95%	7.4 nm	2.10	0.47
90%	8.6 nm	2.44	0.30

Table 5.2: Effect of domain purity on peak of IQE for an exciton diffusion length of 3.53 nm. A full explanation is given in the text.

The above simulations were repeated with $L_x = 6.0$ nm. This enables testing of the assumption that optimum feature size shifts linearly with exciton diffusion length, as well as allowing a more direct comparison of the results calculated here with the systematic experimental study by McNeill *et. al* [64], though this can only be approximate as no attempt has been made to precisely reproduce the mobilities seen in that study.

Purity	**Peak of IQE**	**Ratio**	**IQE**
100%	8.1 nm	1.35	0.56
99%	8.5 nm	1.42	0.55
95%	10.3 nm	1.72	0.50
90%	13.9 nm	2.32	0.46

Table 5.3: Effect of domain purity on peak of IQE for an exciton diffusion length of 6.0 nm.

The ratios of optimum feature size, $l_f(peak)$, to exciton diffusion length are similar here to before, but they are consistently smaller. Although the clarity of this result is hard to be confident of, given the uncertainty in the data and the disparity of feature sizes, it could be explained as follows. The assumption that the optimum feature size shifts linearly with exciton diffusion length implies that the devices are invariant to L_x - doubling it would simply double the l_f scale of the results. However, as shown in Figure 5.4, this clearly cannot be the case, as the relationship $\eta_{cc}(l_f)$ is more complex than this. Shifting L_x into the plateau region of η_{cc} will indeed result in near-invariance of the result

with exciton diffusion length, indeed $l_f(peak) \rightarrow L_x$ as η_{cc} flattens out. Conversely, as L_x approaches smaller distances at which strong coulombic forces dominate (see section 5.4.4), the sharp drop-off in η_{cc} will prevent $l_f(peak)$ from moving too far into this region, increasing the ratio $L_x : l_f(peak)$. Returning to the results for $L_x = 6.0$ nm, it can now be seen that for 90% purity, the IQE peaks at 13.91 nm. This compares favourably with the 18±4 nm optimum feature size in McNeill *et. al*, where the exciton diffusion length is calculated to be between 6 and 10.4 nm.

Self-assembled nanostructures are less likely to contain these islands, enhancing their appeal

5.4.3 Comparison of different morphology classes

Having discussed the trends common to all morphology classes, the differences between the morphology classes will now be examined. These results are plotted in Figures 5.5, 5.6 and 5.7. They are also summarised in Table 5.4, where interpolation has again been used to help identify the point at which the IQE peaks.

	IQE	**PCE**	**FF**
Blend	0.55 (5.6 nm)	0.56% (7.5 nm)	0.34
Rod	0.77 (6.5 nm)	0.91% (8.0 nm)	0.38
Gyroid	0.57 (5.6 nm)	0.53% (8.6 nm)	0.33
Double gyroid	0.58 (6.8 nm)	0.57% (8.3 nm)	0.32
Double diamond	0.59 (6.4 nm)	0.56% (6.9 nm)	0.30

Table 5.4: Interpolated peak values of IQE and PCE, and the feature size at which they occur. Fill factor values are taken at the peak PCE.

Morphology class appears to have little effect on the optimum feature size. Overall, the gyroid, double gyroid and double diamond structures do not compare as favourably with the disordered blend morphologies as might be expected. In terms of both IQE and PCE, the bicontinuous structures are, at best, only fractionally more efficient than the blends. The vertical rod structures stand head and shoulders above the others in terms of efficiency. These data are analysed further in section 5.4.4.

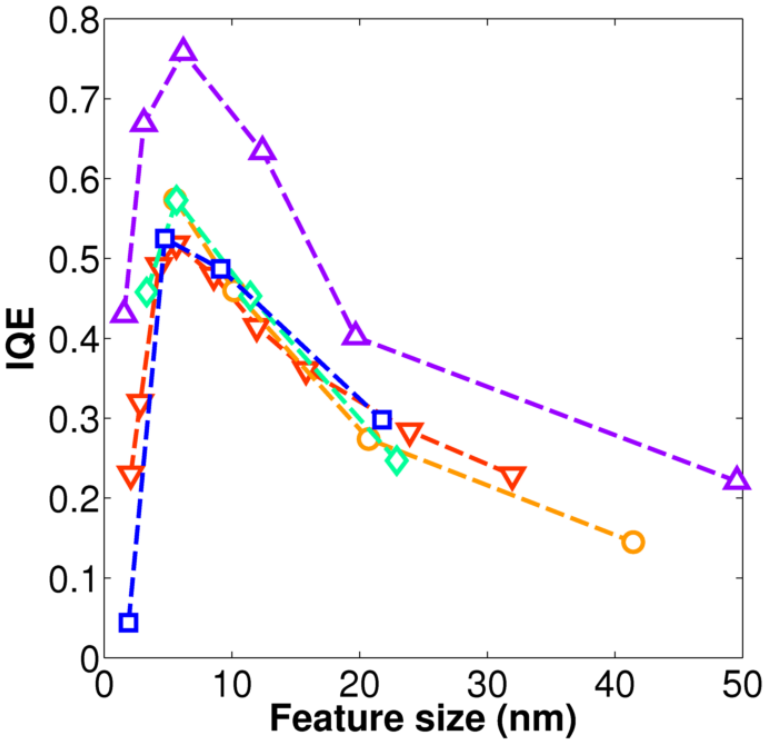

Figure 5.5: IQE as a function of feature size for blend (red, ▽), rod (purple, △), gyroid (orange, ○), double gyroid (green, ◊) and double diamond (blue, □) morphologies.

5.4.4 Recombination data

One of the advantages of the Monte Carlo technique is that it enables examination of the microscopic processes contributing to each result, as has been mentioned above when analysing the origin of certain trends. In this section, geminate and bimolecular recombination are analysed, with discussion as to how these trends contribute to some of those already discussed.

In figure 5.8, geminate recombination is plotted as a function of feature size for all the morphology classes under investigation. In general, increasing l_f reduces geminate recombination because the charges have more room in which to escape their geminate twin. The large drop in $\eta_{gr}(l_f)$ up until 3 nm occurs because the morphology forbids initially separated geminate pairs at the smallest separation ranges from escaping their mutual coulombic well. At l_f =3 nm there is a sharp change in the drop off rate for

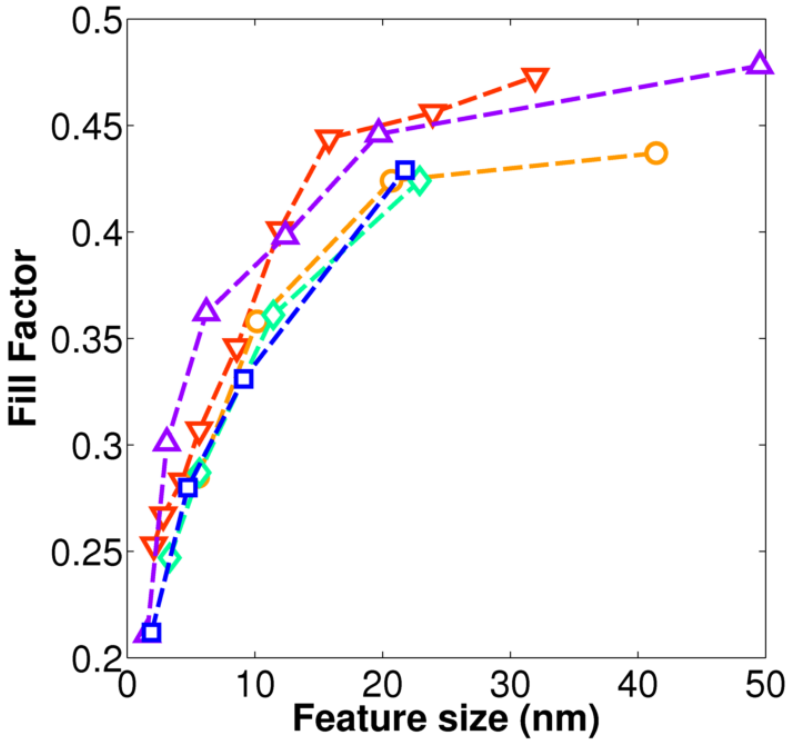

Figure 5.6: FF as a function of feature size. Symbols and line types as for Figure 5.5.

$\eta_{gr}(l_f)$, as at this range coulombic attraction is comparable with energetic disorder. For $l_f > 3$nm, charges have the room required to escape their mutual coulombic well and avoid recombination, but $\eta_{gr}(l_f)$ continues to decrease because the morphology, both physical and energetic, can still force free charges back together *en route* to the electrodes. Such behaviour was seen and explained by Groves *et. al.* [41] for bilayer and blend devices. Single and double gyroid structures, however, exhibit a modest increase in η_{gr} with l_f for $l_f > 3$nm, an effect which can be explained in section 5.4.6 by examining its illumination dependence. Geminate recombination is lowest in the rod structures because the morphology does not obstruct the charges from separating perpendicular to the interface, and rapid extraction is facilitated by the short, direct escape route to the electrodes. This advantage is lost at the two smallest rod sizes, 1 nm and 2 nm, because motion perpendicular to the interface is particularly tightly constrained, reducing the number of degrees of freedom and making separation highly unlikely, as charges are unable to escape their mutual coulombic well. In this case charges are more likely to track each other along the interface, creating multiple recombination attempts of the

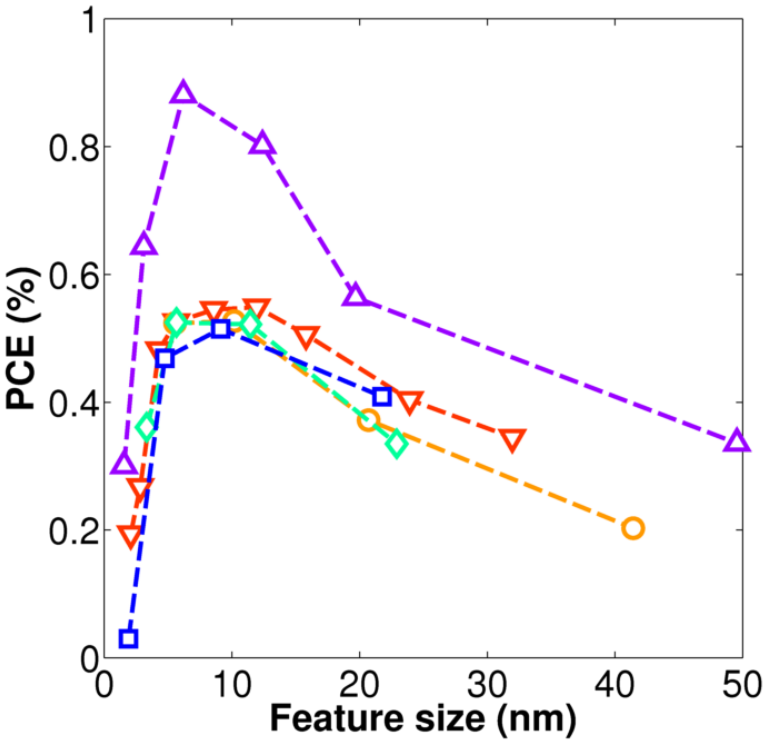

Figure 5.7: PCE as a function of feature size. Symbols and line types as for Figure 5.5.

geminate pair.

The result may be slightly biased by the relaxation of the excitons in the density of states (DOS). As feature size increases, excitons that reach the interface will have explored more of the DOS, and the energetic dependence of the Förster transfer rate means they will move downward in energy as they do. Therefore, excitons in larger features that travel further before dissociation are likely to reach a lower energy site than those that dissociate soon after forming. It follows that, following dissociation, the charge carrier created on the same side of the heterojunction as the dissociating exciton will rest on a site of at least marginal trapping, an effect which may increase η_{gr} [89].

Figure 5.9 shows that bimolecular recombination drops off more steadily with l_f. This is simply because morphologies with a larger feature size are able to keep charges physically separated due to the greater distances between interfaces, reducing the probability of this form of recombination occurring. These morphologies also dissociate fewer excitons,

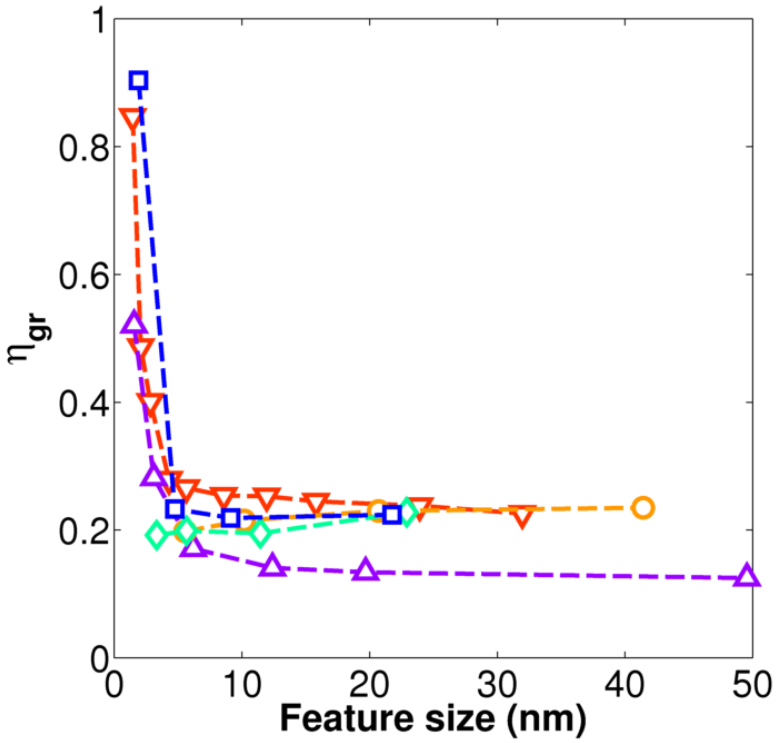

Figure 5.8: Recombination fraction of geminate pairs, η_{gr}, for all morphology classes, as a function of feature size. Symbols and line types as for Figure 5.5.

reducing the charge density and further lowering the probability of two nongeminate charges encountering each other. It is not possible to create the single gyroid and double diamond morphologies with $l_f < 2$ nm, but for the other morphologies, η_{br} takes its lowest values at these small feature sizes. This result is a direct corollary of the data in Fig 5.8. The low η_{br} values at small feature size are a consequence of η_{gr} being high for these morphologies, removing charges that could otherwise suffer bimolecular recombination. Once η_{gr} reaches a low value as l_f approaches 3 nm, there is a consequent sharp increase in η_{br}. For $l_f > 3$ nm η_{br} drops off for all morphologies, although the single gyroid shows slightly less bimolecular recombination than the blends at larger feature sizes. The rod structures again have much lower recombination, due to the short time the charges spend within the device, and the clear segregation of the charge transport pathways.

The recombination data show the origin of the high efficiency of the rod devices. How-

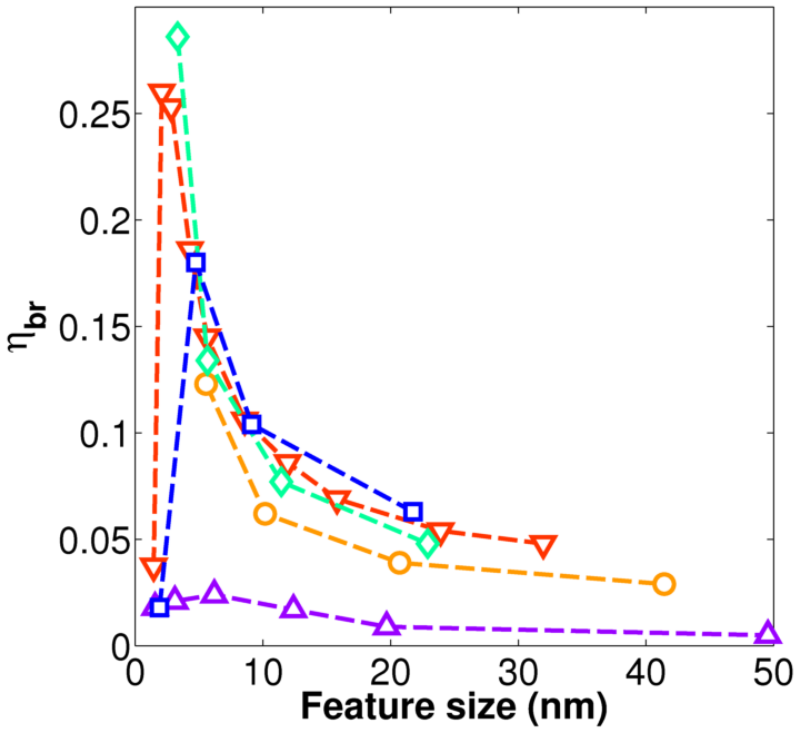

Figure 5.9: Recombination fraction of bimolecular pairs, η_{br}, for all morphology classes, as a function of feature size. Symbols and line types as for Figure 5.5.

ever, it fails to explain why the novel morphologies appear to be no better than blends at either achieving separation of the geminate pair, or preventing recombination *en route* to the electrodes. It is inferred that the presence of islands as well as discontinuous pathways in the blends is not a severe limitation in their efficiency. The true origin of blend (in)efficiency is discussed below.

The microscopic origin of the feature size dependence of FF

Figures 5.2 and 5.6 show that the fill factor of the devices consistently increases with l_f, a result already explained briefly in Section 5.4.1. Separate analysis of the geminate and bimolecular recombination data allows for a fuller, microscopic explanation of this result. Figure 5.10 shows the current density, charge collection efficiency and both forms of recombination, as a function of voltage, for $l_f = 2.1$ and 32.0 nm. The fill factors are

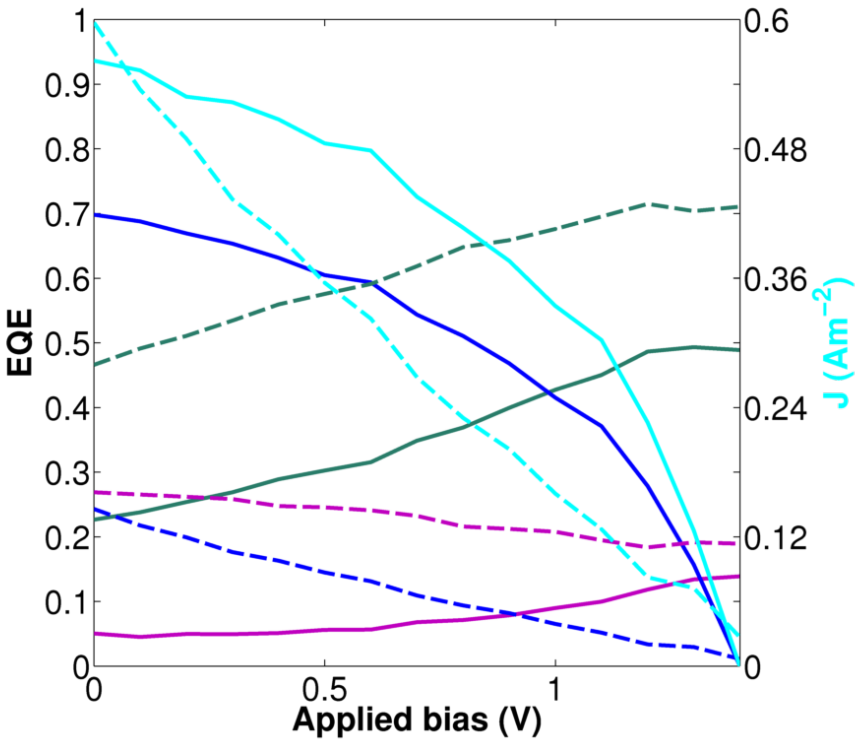

Figure 5.10: Voltage dependence of solar cell efficiency, for the 2.1 nm (dotted line) and 32.0 nm (solid line) morphologies; showing η_{cc} (blue), η_{gr} (green), η_{br} (purple), J (cyan).

0.23 and 0.70 respectively. Comparing these two particular morphologies is revealing, as the data shows that they have similar current densities at both 0 and 1.4 V, but with a very clear divergence in-between. Examination of η_{cc} begins to explain this, showing that the morphology with $l_f = 32.0$ nm has a vastly greater ability to collect charge, the resulting current being proportional to the product $\eta_{cc} \times \eta_{ed}$, where η_{ed} is voltage independent. Whereas for the 2.1 nm morphology, the voltage dependence of both J and η_{cc} is linear (except close to open circuit where injection begins), for the 32.0 nm morphology the voltage dependence is non-linear, shifting the maximum power point to a higher voltage, creating a higher fill factor.

As $\eta_{cc} = 1 - (\eta_{gr} + \eta_{br})$ (as charge can only be lost by one of these two recombination mechanisms), the non-linearity must lie in $\eta_{gr}(V)$ or $\eta_{br}(V)$. $\eta_{gr}(V)$ has the same linear trend in both morphologies, and only varies in magnitude. The linearity is due to the origin of η_{gr}, which is the result of the competition between hopping away from the in-

terface and a fixed recombination rate, k_r. Over the range of voltages examined, $k_{ij}(V)$, from Eq. 2.25 is approximately linear. This means that the origin of the different fill factors must lie solely in the field dependence of η_{br}. For the 2.1 nm morphology, η_{br} drops off linearly with field, which, combined with the linear trend in $\eta_{gr}(V)$, explains the overall linear trend in both J and η_{cc} for this morphology. However, for the 32.0 nm morphology, bimolecular recombination exhibits a nonlinear *increase* with field. This in turn causes η_{cc}, the rate of change of which starts off parallel to that for the small morphology, to drop off more rapidly with field. When there is a high current flow, the morphology with the smaller interfacial area will suffer less bimolecular recombination, as there are fewer places for charges to meet. It might be expected that this ceases to be true for a higher interfacial area, but such morphologies also have a greater number of separate pathways for charge to flow along, which may keep different current channels entirely separate. At short circuit, the current density is higher, meaning the occupation probability of each channel is high, facilitating high recombination. Towards open-circuit, the charge density is higher [55], but the current flow is lower, and the high geminate recombination shows charges will not travel far from their point of formation, which with a Gaussian absorption profile will be close to the centre of the device. The remaining current flow towards the electrodes is low, and hence the few charges that *are* passing through the system may be incapable of encountering one another in a morphology with high interfacial area due to the occupied channels being entirely separated by unoccupied ones. When there are fewer, larger features, encounters are always possible, even at low current density. This explanation can be confirmed by examining the same data for the square rod morphologies (not shown), where the 'isolated channel' picture is clearer. The same trends are found.

5.4.5 The geometry of the geminate recombination mechanism

Both the novel structures and the rods are bicontinuous, free from tortuous and disconnected charge transport pathways, as well as islands. Yet, whereas the rods perform much better than the blend structures, both in terms of geminate and bimolecular recombination, the novel morphologies have approximately the same efficiency. In the simulation, the probability of separation following dissociation is determined by the competition between the field dependent rate for one of the charges to hop away from the interface, described by Eq. 2.25, and the constant recombination rate k_r. Eq. 2.25

shows a sinusoidal relationship between the hopping rate and the angle of the hop with respect to the field. With respect to hopping perpendicular to the field, parallel and anti-parallel hops result in equal and opposite changes to the hopping rate, and hence the probability of recombination. For rods, separation is always perpendicular to the field. Blends and bicontinuous structures have interfaces at angles from 0°(field-assisted separation) to 180°(field impaired separation) with respect to the field and so might be expected to have a similar efficiency to the rods, the variations in hopping rate being averaged out. However, initially separated charges will have multiple attempts at geminate recombination if initial separation is against the field, as they will need to explore the interface to find a way out. Thus, the detrimental effect of an interface where separation is against the field, when compared to perpendicular separation, is far greater than the advantage of separation with the field.

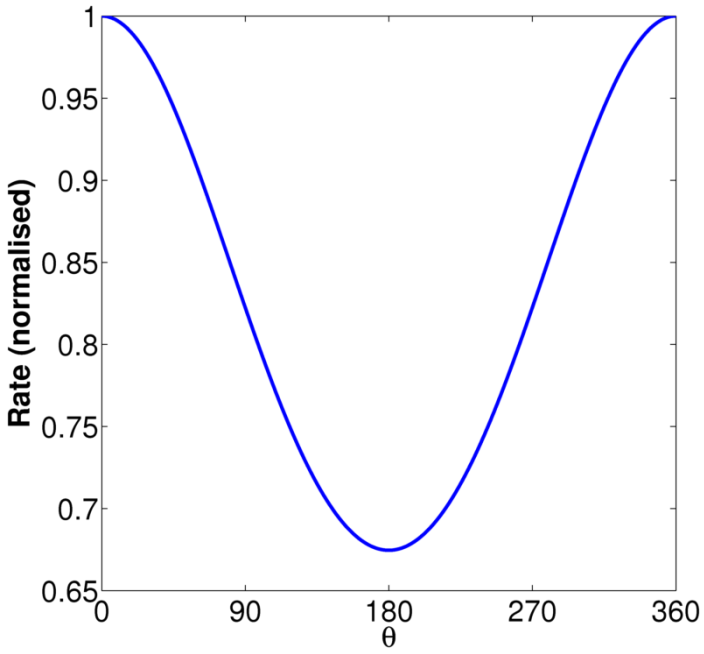

Figure 5.11: Charge hopping rate as a function of field at angle θ with respect to the interface normal. Hopping rate is calculated from Eq. 2.25 and normalised to its value for a bilayer device ($\theta = 0$).

To confirm this argument, bilayer structures were created for separation at different angles to the field. The fraction of charges successfully escaping geminate recombination, η_{gs}, were obtained for a field $F = 1 \times 10^7$ Vm^{-1}. The results are shown in Table 5.5,

and are in agreement with the much more detailed study by Groves *et. al.* [41]. The magnitude of this effect shows it is the dominant limiting mechanism for efficiency. Hence, as the interfaces in the blend and bicontinuous morphologies have no preferred direction with respect to the field, the results can be expected to be noticeably below those for the rods, where the interface is always at 90°, which is what is found. This is a crucial effect which is only seen in Monte Carlo modelling, where the full geometry of the microscopic mechanisms inside organic electronic devices is taken into account. As an aside, it is not anticipated that this effect will create a problem when implementing these structures in DSCs, as the device structure screens out the internal field [125].

Angle	η_{gs}
0°	78%
90°	74%
180°	17%

Table 5.5: Geminate separation as a function of angle to field. Field simulated is 1×10^7 Vm^{-1}.

5.4.6 Illumination

Intensity dependence

Varying the illumination level provides further valuable insight into the mechanisms controlling organic solar cell behaviour. To investigate this, simulations were run from 0.1 to 20 suns illumination, for one morphology from each class. All the morphologies have a feature size of approximately 10 nm (or as close as possible, given the discretisation of feature sizes produced by the Ising model), and all illumination simulations were performed at short-circuit.

The current density for each morphology is plotted in figure 5.12 as a function of illumination level (measured in suns, where 1 sun is defined by the AM 1.5 spectrum, of which 5.8% is absorbed by a PFB:F8BT blend). As can be seen, all the devices exhibit a slightly sublinear response to illumination, showing that efficiency decreases as a function of light intensity. The results for the bilayer are in reasonable quantitative agreement with experiment [64], suggesting that the ratio of recombination rate to mobility used in these simulations is approximately correct. The sublinearity indicates the existence of

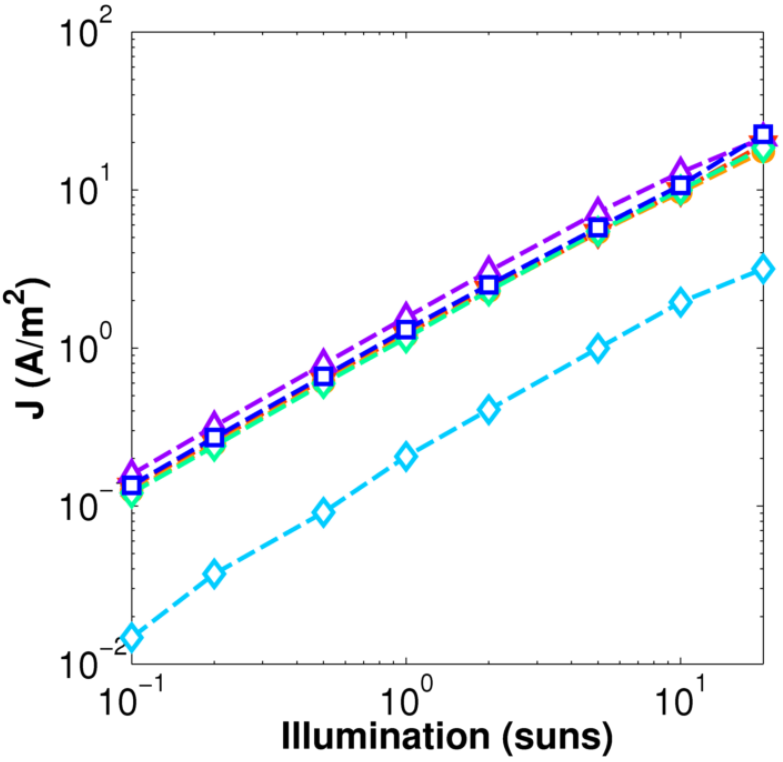

Figure 5.12: Current density as a function of illumination level. Symbols and line types as for Figure 5.5, with the addition of the bilayer structure (cyan, ♢).

charge density dependent effects, such as bimolecular recombination and space charge. Here, space charge is defined as the accumulation of charge in the same space, the effect of which is a modification of the geminate dissociation efficiency due to changes in the local field, i.e. the coulombic effect of local charges. The losses can be split into the two constituents of geminate (Fig. 5.13) and bimolecular (Fig. 5.14) recombination. Exciton dissociation efficiency is unaffected by illumination level as exciton-exciton annihilation is not included in these simulations.

Unsurprisingly, bimolecular recombination increases with intensity. The higher the charge density in the system, the more crowded the transport pathways become, and the more likely charges are to recombine en route to the electrodes. This effect is noticeably suppressed in the bilayer device. In this morphology, fewer charges will be dissociated, reducing the carrier density at any illumination level with respect to the other morphologies, and thus reducing recombination. Furthermore, once charges leave the single

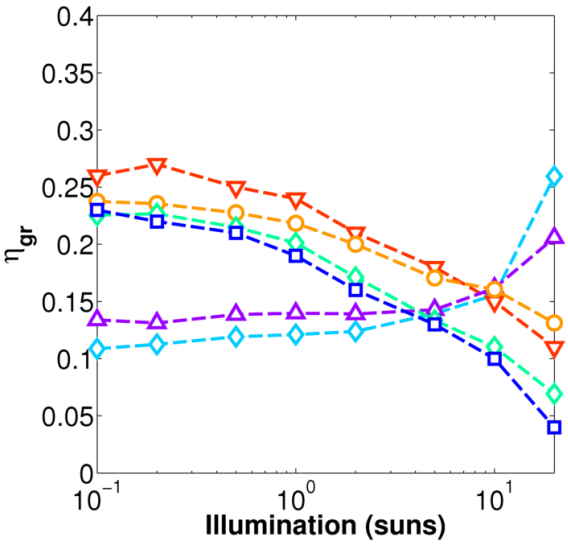

Figure 5.13: η_{gr} as a function of illumination intensity. Symbols and line types as for Figure 5.12.

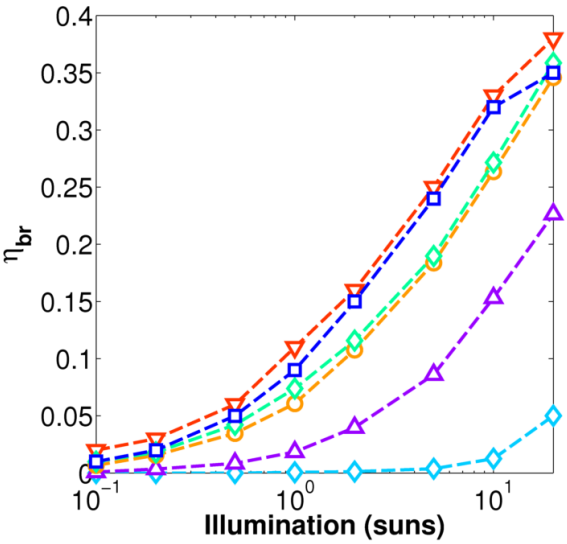

Figure 5.14: η_{br} as a function of illumination intensity. Symbols and line types as for Figure 5.12.

interface they cannot encounter any other charges of the opposite kind. The fact that any bimolecular recombination exists at all suggests that charges remain near to the interface for a long enough period of time to escape their original twin but still encounter another charge. That both forms of recombination increase in the bilayer structure also shows that diffusion plays no useful role here - increasing the charge density gradient causes the efficiency to decrease, not increase. This will be discussed below with respect to interface geometry. At higher illumination levels (5 suns in the blend, 10 suns in the rods), bimolecular recombination overtakes geminate as the dominant recombination mechanism.

The geminate results are more interesting. In the rod and bilayer structures, geminate recombination increases gradually with illumination, whereas in the blend and novel morphologies it decreases. This suggests that space charge can have opposite effects on efficiency depending on the device structure. The greater recombination in the bilayer and rod structures can be understood easily. All the surfaces in these structures are planar, and the presence of multiple geminate pairs along the same planar stretch of interface (of which there is only one in the bilayer, which is why this effect is more pronounced) leads to a reduction in the probabability of charges escaping the interface, due to coulombic interaction of the multiple pairs. This is illustrated in Figure 5.15a.

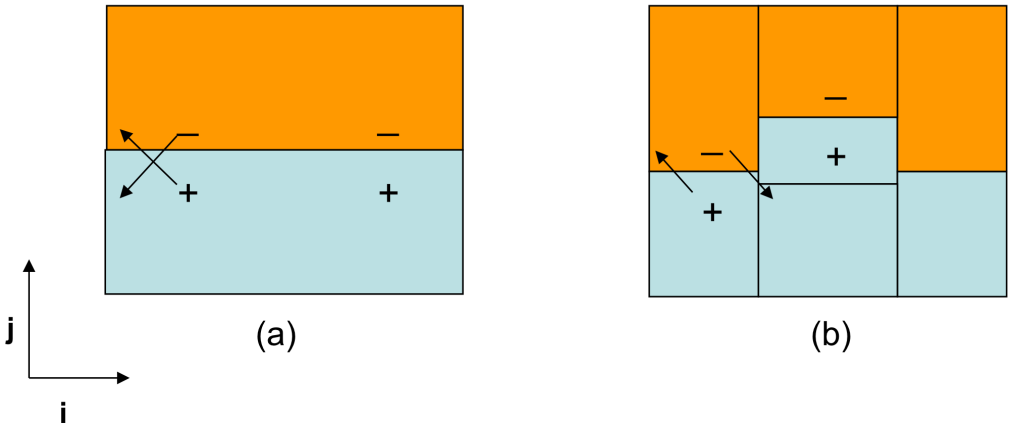

Figure 5.15: By resolving forces in two dimensions (i and j), this figure illustrates the impact on a geminate pair of introducing a second geminate pair in close proximity. (a) (Planar interface) In j, the presence of the second charge pair drives the the first pair towards each other. As the recombination rate k_r is fixed, the effect of this is to reduce the rate of hopping away from each other perpendicular to the interface. In i, both charges are driven along the interface in the same direction, causing tracking and multiple attempts at recombination. Overall the probability of eventual recombination is increased. (b) (Non planar interface) In j, the presence of the second charge pair drives the charges towards each other as before. However, the charges are driven in opposite directions in i. As the recombination rate is fixed, the net effect is to pull the charges apart along the interface. The overall probability of recombination is decreased.

The blend and bicontinuous structures contain curved surfaces (or at least the cubic lattice approximation of curves). With curved surfaces, the presence of additional charge pairs in close proximity increases the probability of separation. This is illustrated in Figure 5.15b. Higher charge densities increase the magnitude of this effect, showing why geminate recombination decreases with illumination. This can therefore be seen as a 'positive' space charge effect. It is not known to what extent these variations would be seen in real devices, where genuinely planar surfaces would be extremely rare due to interfacial roughness.

Feature size dependence at 5 suns

The above analysis of the role of feature size on efficiency, for all the morphology classes, is now repeated at 5 suns illumination. A PFB:F8BT blend absorbs relatively little of the AM 1.5 spectrum (see Section 2.1.2), so the charge densities at this higher illumination level show effects that may reasonably be expected in other common PV materials at 1 sun illumination. The IQEs for the different morphology classes is shown in figure 5.17 and the geminate and bimolecular recombination levels are given in figure 5.19 and 5.21. These figures have been plotted against those for 1 sun illumination, for ease of comparison.

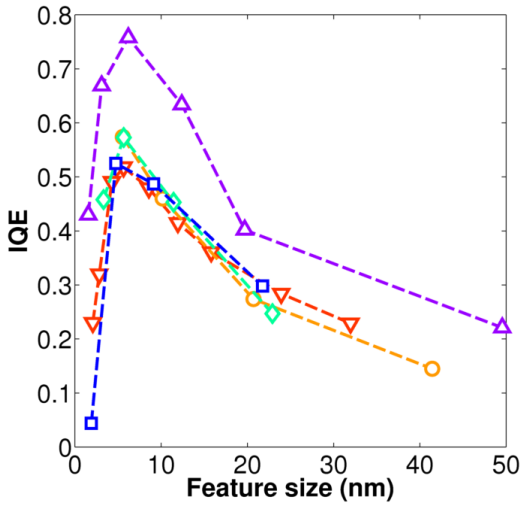

Figure 5.16: IQE as a function of feature size at 1 sun illumination for blend (red, ▽), rod (purple, △), gyroid (orange, ○), double gyroid (green, ◊) and double diamond (blue, □) morphologies.

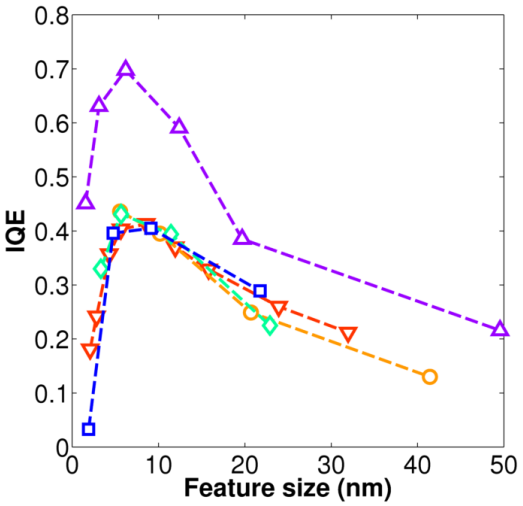

Figure 5.17: IQE as a function of feature size at 5 suns illumination. Symbols and line types as for Figure 5.16.

The most significant change when increasing illumination from 1 to 5 suns is in the level of bimolecular recombination, which increases significantly for all morphologies. This reduces the IQE of the blends and bicontinuous structures by 12-25%, but the rods by only 8%, widening their efficiency advantage over the other structures. It is clear from this that the novel structures are no better at handling higher charge densities than the blends - the level of bimolecular recombination and the IQE shift by very similar amounts in both. This is further evidence that the disordered structure of the blends

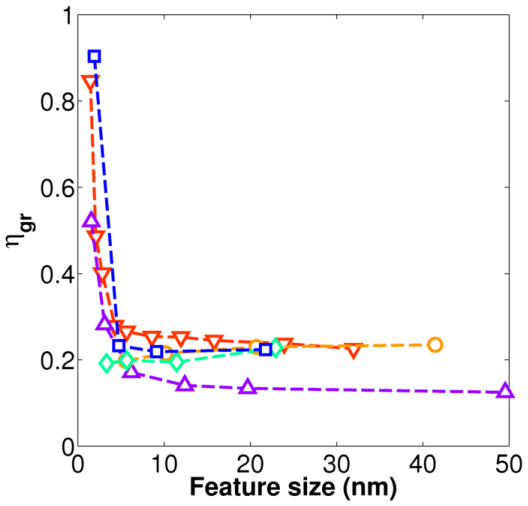

Figure 5.18: η_{gr} as a function of feature size. Symbols and line types as for Figure 5.16.

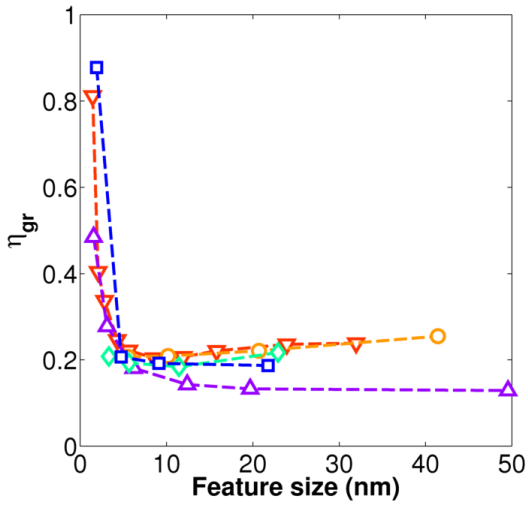

Figure 5.19: η_{gr} as a function of feature size at 5 suns illumination. Symbols and line types as for Figure 5.16.

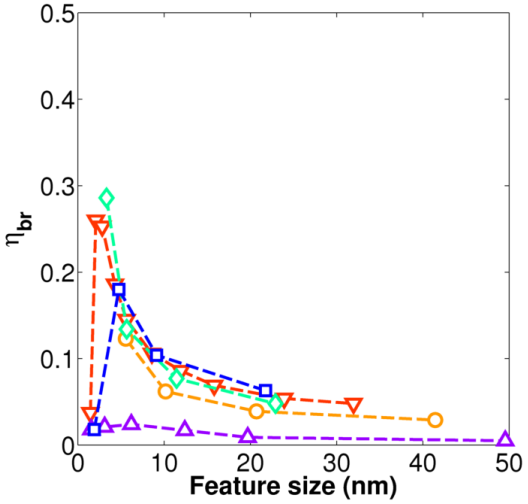

Figure 5.20: η_{br} as a function of feature size. Symbols and line types as for Figure 5.16.

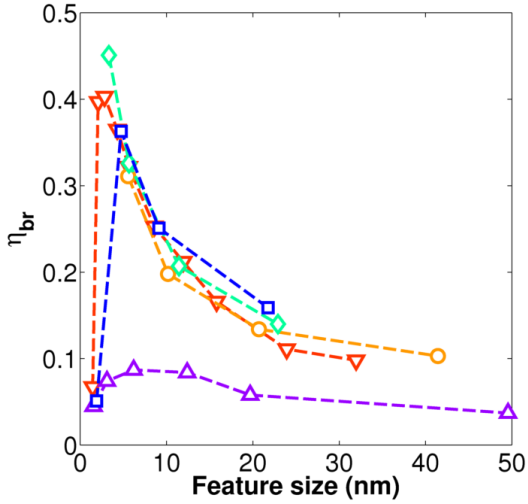

Figure 5.21: η_{br} as a function of feature size at 5 suns illumination. Symbols and line types as for Figure 5.16.

is not primarily responsible for their inefficiency. Additionally, the blend morphology where the IQE peaks shifts from that with $l_f = 5.6$ nm to that with $l_f = 8.6$ nm, as wider pathways are required to keep recombination at a reasonable level.

It was seen earlier that at normal illumination the gyroid and double gyroid structures exhibit an increase in η_{gr} with l_f. At 5 suns illumination, this trend continues to be seen, but is now also seen in the blend structures when $l_f > \approx 10$ nm (below this point η_{gr} increases due to the constrained geometry, as explained earlier, creating a minimum in l_f). The origin of this effect lies in the mechanism described in Fig 5.15.

Given that these morphologies are constructed on a cubic lattice, scaling up a gyroid or blend morphology will have the result that the number of instances of curved surfaces will remain the same, but the surfaces will become wider and flatter. In other words, although the overall interfacial area will decrease, a greater proportion of connected planar surfaces will emerge, as small connected surfaces are made larger. This will increase the instances of multiple charges along the any single planar interface, which will reduce the escape probability of the charge pairs, and increase recombination. In the blend, gyroid and double gyroid structures, doubling the feature size will double the size of the planar sections of the morphology, without halving the charge density (as seen by the IQE plots). Therefore, as feature size increases, the relative proportion of charges along planar surfaces will increase, increasing geminate recombination. In the rod structures, there are no curved features, and so all the surfaces can already be considered planar and are perpendicular to each other. Increasing the feature size will reduce the total surface area, and hence the area of planar surfaces, whilst charge density is also reduced, explaining why this effect is not seen. This can be seen not only in terms of scaling up a morphology, but also in the nature of the Ising model. Larger feature size blend morphologies have undergone more pairwise swaps to reduce the potential energy of the structure, which will increase the number of planar surfaces, as these have lower energies.

This is likely to be confirmation of the space charge effect described above with respect to variations in the intensity dependence of geminate recombination in different morphologies (Figures 5.13 and 5.15), as the effect of this process will be more noticeable for large domains where more geminate pairs can align along the same planar stretch of interface. It has already been seen that, at 1 sun illumination, this effect is absent in the blends but present in the gyroid and double gyroid structures. Additional simulations show the effect is absent in the latter structures at 0.01 suns. Hence there is a coulombic effect due to the close proximity of multiple geminate pairs which becomes noticeable in the single and double gyroid structures at a lower illumination level than the blends.

The charge densities simulated here are of the order of $10^{21} - 10^{22}\ m^{-3}$, consistent with other models [53, 45, 55], which in a system of this size consists of no more than approximately 10 charge pairs at any time. Animations show that these charge pairs remain in the vicinity of each other for a long time after dissociation, and can track each other within the device. The reason the novel morphologies are more influenced by this effect is due to the continuous nature of their interface, which allows charge pairs to track each other throughout the device, whereas the blends have broken interfaces which reduce tracking. This effect competes with the two already described: difficulty in escaping the mutual coulombic well at very small feature sizes, and diffusion from curved surfaces.

5.4.7 Recombination rate

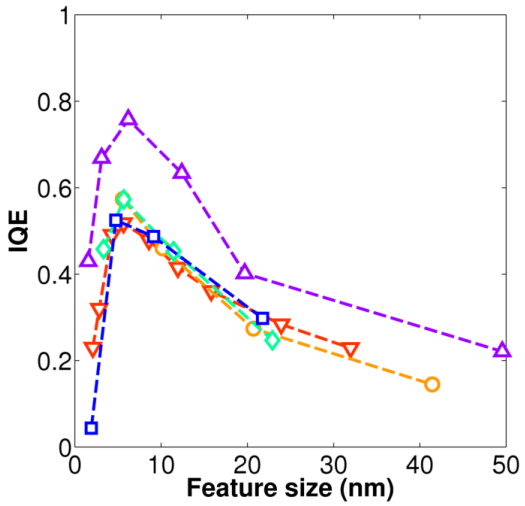

Figure 5.22: IQE as a function of feature size for $k_r = 1 \times 10^6$. Symbols and line types as for Figure 5.16.

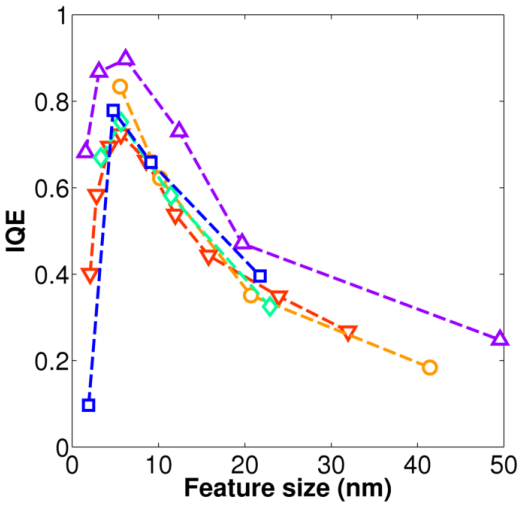

Figure 5.23: IQE as a function of feature size for $k_r = 1 \times 10^5$. Symbols and line types as for Figure 5.16.

Comparison of figures 5.22 and 5.23 reveals that lowering the recombination rate by an order of magnitude increases the charge collection efficiency of all morphologies. In the case of blends, the peak IQE increases by 35% to 0.72; and the peak PCE increases by 69% to 0.93% and the fill factor for the optimum morphology increases by 26% to 0.44. As the PCE incorporates both IQE and FF into its calculation, the relative change in its value is larger than for the IQE.

The rods continue to show the highest efficiency, but the most efficient of these have less of an advantage over other morphologies at this recombination rate. Whereas for $k_r = 1 \times 10^6$, the peak IQE was 33% higher than the next best non-rod structure, at this lower recombination rate it is only 5% higher. The reason is that the level of geminate and bimolecular recombination in the rods is very low for $k_r = 1 \times 10^6$, leaving little room for improvement, and at this lowered recombination rate $\eta_{gr} < 5\%$ and $\eta_{br} < 2\%$ for nearly all structures. Therefore the rod structures are approaching a saturation point where their IQE is determined by exciton dissociation efficiency alone. The non-rod structures, with their higher recombination levels under normal parameters, therefore benefit more from a lowering of the recombination rate. Consequently, this shows that using higher mobility materials in experiment will be of limited benefit if exciton harvesting cannot also be improved.

5.4.8 Mobility

To investigate the role of mobility, simulation were performed at mobilities one order of magnitude above and below the value used so far (Table 5.1). As is to be expected, device efficiency increases and decreases in line with charge mobility. In the blend morphologies, raising the mobility to $\mu_0 = 10^{-6}$ $\mathrm{m}^2(\mathrm{Vs})^{-1}$ increases the peak IQE by 22% to 0.652 and the peak PCE by 50% to 0.817%. Decreasing the mobility to 10^{-8} m^2 $(\mathrm{Vs})^{-1}$ reduced the peak IQE by 43% to 0.308, and the PCE by 50% to 0.272%. The fill factor also increases and decreases with mobility, again explaining why the relative increase in PCE is greater than that in IQE.

Figure 5.24 shows geminate and bimolecular recombination for the three mobilities in the blend structures. As can be seen, geminate recombination dominates. The simulations show that an order of magnitude change in mobility shifts η_{gr} by a factor of approximately two for all morphologies. Therefore the relative loss to the IQE for decreasing the mobility should be approximately double what it gains for increasing the mobility, which is what we observe (43% and 22%). Bimolecular recombination, however, reacts differently to mobility shifts. Instead of varying inversely with the mobility change as the geminate rate does, both raising and lowering the mobility reduces bimolecular recombination across most feature sizes, suggesting that the mobility used thus far happens to be near an η_{br} maximum. At low mobility, this occurs because increased geminate

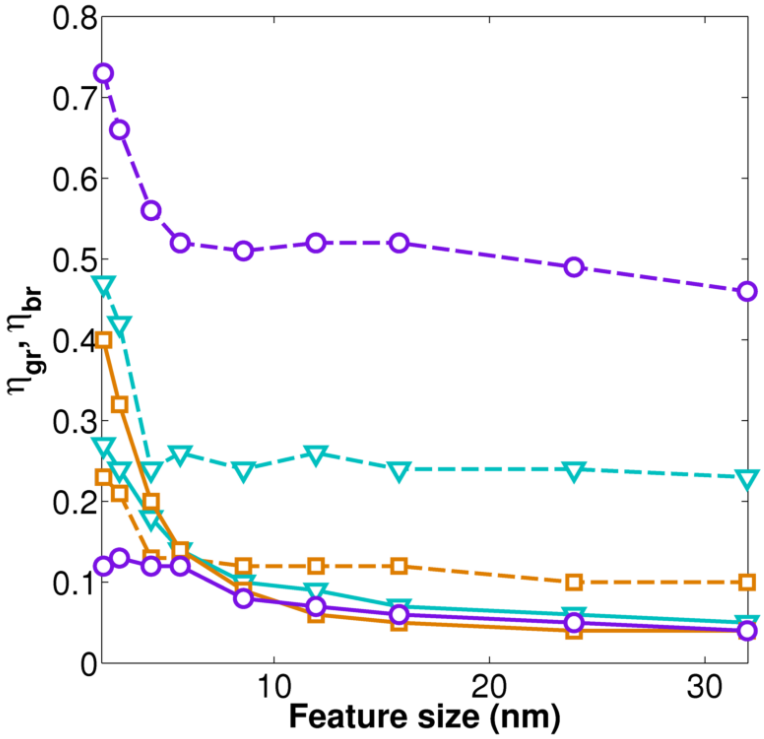

Figure 5.24: Geminate (dashed line) and bimolecular (solid line) recombination for the morphologies, as a function of feature size. Showing $\mu_0 = 10^{-6}$ m^2 (Vs)$^{-1}$ ($\square$); 10^{-7} m^2 (Vs)$^{-1}$ ($\bigtriangledown$) and 10^{-8} m^2 Vs^{-1} ($\circ$)

recombination removes charges that would otherwise have suffered bimolecular recombination, lowering η_{br}, analogous to the situation at the very smallest feature sizes under normal parameters, discussed in section 5.4.4. For a high mobility, η_{br} is lowered for the same reasons as η_{gr}, except at small feature sizes, where the increased charge density in a limited space leads to an increase level of bimolecular recombination. Performing the same analysis for the rod morphologies (not shown) shows they have little room for improvement in this area, and so the gap between them and the other morphologies is reduced.

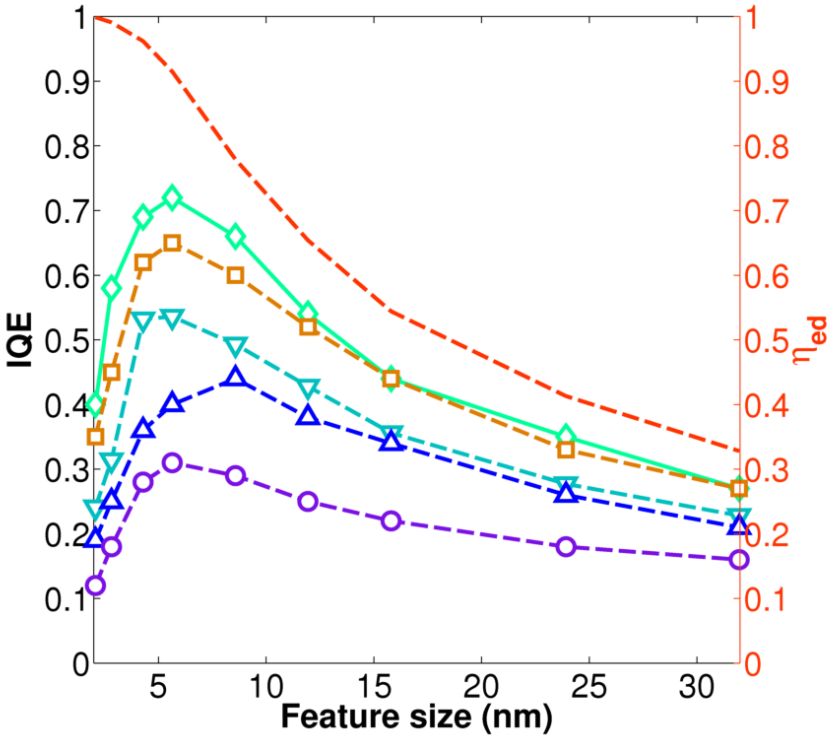

Figure 5.25: IQE(l_f) for the parameters in Table 5.1 ($\bigtriangledown$); $\mu_0 = 10^{-6}$ m^2 (Vs)$^{-1}$ ($\square$); $\mu_0 = 10^{-8}$ m^2 Vs^{-1} ($\circ$); $k_r = 1 \times 10^5$ s^{-1} ($\Diamond$) and 5 suns illumination($\bigtriangleup$). Also shown is exciton dissociation efficiency (dotted line) for comparison.

5.4.9 Overall

Figure 5.25 summarises the effects of varying the mobility, recombination rate and illumination on the IQE of blend morphologies. In addition to the trends already discussed, this figure also reveals that the relative advantage of either a higher mobility or a lower recombination rate for the blend structures is feature size dependent. Beyond $\approx$ 15 nm, the results for $\mu_0 = 10^{-6}$ m^2 (Vs)$^{-1}$ and $k_r = 1 \times 10^5$ s^{-1} are near-identical. For smaller feature sizes, however, lowering the recombination rate appears to create a greater performance improvement.

At these smaller feature sizes, the narrow and tortuous percolation pathways may prevent the charges from being immediately separated by the field, forcing them together for sections of the simulation, during which time they may track each other and un-

dergo multiple recombination attempts. A higher mobility is of little or no advantage under these circumstances, as it cannot be used to enhance separation if separation is impossible. However, a lower recombination rate will always be an advantage under these circumstances. For example, if 10 hops are required to move the charges from the point of creation to a point where they be separated by the field, then, regardless of mobility, there will be 10 recombination attempts, each with the same probability. Hence the best way to reduce recombination will be to reduce the recombination rate. A higher mobility may be of some advantage if it leads to a greater average distance per hop, but the results clearly show that this advantage is outweighed by that of the lower recombination rate. Whenever there is room to escape the interface in the direction of the field, such as with larger percolation pathways, or in the rod structures where the pathways are always parallel to the field, this ceases to be the case. Repeating these simulations on the rod structures confirms this - the effect of raised mobility or lowered recombination rate are near identical at all feature sizes.

5.5 Summary and conclusions

The simulations performed have examined the effects of feature size, domain purity, illumination level, recombination rate and mobility for a range of morphologies. The morphologies simulated have been characterised in terms of η_{ed}, η_{cc}, η_{gr}, η_{br}, IQE, FF and PCE. For each set of parameters, morphologies with a range of feature sizes have been simulated at short circuit, and frequently across a range of voltages up to open circuit as well. The morphologies have been grouped into five classes: disordered blends; vertical interdigitated rods; and three novel, bicontinuous morphologies: the gyroid, double gyroid and double diamond phases, as formed in diblock copolymers. Th effect of group type on performance characteristics has also been examined.

The general trends observed are consistent with experimental findings, validating the modelling approach used here. By separately analysing the underlying mechanisms contributing towards the various measures of efficiency, it has been possible to give microscopic explanations behind these trends. Furthermore, the demonstration that optimum feature size for morphologies characterised at short circuit is less than that which is best for power conversion efficiency will help inform experiment; as will the findings concerning the role of impurities, which also shift the perceived optimum feature

size.

Many counterintuitive discoveries have also been made, the most useful being those that are unique to Monte Carlo modelling - the ones that consider the precise impact of the morphological geometry being studied. It is also these that are most relevant when investigating the possibility of using novel structures for solar cell morphologies, the task of this chapter. Most critically, it has been shown that the angle of the interface at which exciton dissociation takes place, with respect to the field, is more critical for determining efficiency than previously thought. In other forms of modelling, it is assumed that η_{gr} is determined solely by the initial scenario in which the charges find themselves. However, the modelling here reveals that charges that are not immediately driven apart by the field will spend a significant amount of time exploring the interface, tracking each other as they do, increasing the number of recombination scenarios (this was also confirmed by running animations of the simulations). Therefore, when compared to separation perpendicular to the field, the loss in efficiency when separating against the field is far greater than the gain from being aligned to the field. Thus, any morphology where the angle of the interface to the field varies continuously, such as the blends or novel structures, will be significantly less efficient than a vertical structure. As the disordered blend and the novel morphologies produce similar efficiencies, it is this effect that is deemed to be the primary mechanism limiting blend efficiency, and not disorder.

These conclusions concerning the geminate dissociation mechanism were also reached by Groves *et. al.*, providing confirmation of many of the conclusions reached in this chapter. Here, however, the results have been deduced from the scenario of comparing disordered with bicontinuous morphologies, which may be more directly applicable to future morphology research. Of course, this conclusion rests on the assumption that the description of the dissociation mechanism contained herein is correct. In other words, if the rate of recombination is *not* determined by the competition between a fixed recombination rate and a hopping away rate, described by Marcus theory, then the conclusions contained herein may not be completely valid. The full nature of the recombination process in experiment is more complex than can be accounted for using this model. Furthermore, it has been shown more recently that in PFB/F8BT, the energetics at the interface are different to those in the bulk, with greater trapping occurring and hence very little tracking by geminate pairs [89]. However, the basic idea that charges caught in an intricate morphology will have to explore the interface, often moving counter to the field, and thus track each other, increasing the probability of recombination, is inescapable. The

only uncertainty is in the magnitude of this effect in different systems.

When this work was conceived, it was predicted that triply-periodic minimal surface 'novel' morphologies would create a means of raising solar cell efficiency, as the understanding was that the main limitation in the blends was their disordered structure. This has been shown not to be the case, and the mechanism described above explains why. The novel morphologies are not a complete loss, however. They frequently exhibit marginally higher efficiencies than the blends, and are free from disconnected islands. Also, as the novel morphologies represent a minimum energy structure that will self assemble under the correct circumstances, it should be easier to reproduce particular structures, enhancing their practical appeal. This contrasts with the less predictable 'shake and bake' process, used to create the disordered blends, which has an innate problem with reproducibility [91]. Vertical rod structures may be the best option if they can be made defect free, as they exhibit a far superior performance, A very narrow rod structure is the most desirable, to improve the exciton dissociation efficiency. In order to maintain good charge collection, high mobility materials would be required, in order to reduce geminate recombination and evacuate charges quickly to avoid subsequent loss.

Other conclusions reached include the nature of recombination at planar and curved surfaces. It was shown that increasing the charge density along planar surfaces increases geminate recombination, but at curved surfaces reduces it. This has implications for both illumination and morphological dependence of η_{gr}. However, it is hard to say to what extent this would be seen in experiment, as truly plane surfaces will be rare. The illumination section also shows that, whilst the biggest limitation to solar cell efficiency is likely to be optical absorption, more highly absorbing polymers are of little use if their structure and chemical properties are not tailored to handle the increased charge density efficiently.

Chapter 6

A quantitative model of photovoltaic devices

6.1 Introduction

As has already been outlined in Section 3.1, there are several approaches to modelling polymer electronic devices, some of which will be explored in more detail in the present chapter. Previous work by research groups has often been successful in quantitatively reproducing experimental results in one or more aspects of device behaviour. However, the scope of previous successes in device modelling is usually relatively narrow, with published studies focussing almost entirely on one particular aspect of a complete device model, such as mobility, injection or overall efficiency; with the interdependency of these aspects rarely investigated. For example, work may focus entirely on the mobility of a polymer or device, and not attempt to use this to accurately predict overall efficiency [56]; or model the overall efficiency, using a fitted mobility value plucked from a range of reasonable values contained in the literature [77]. Complete self-consistent studies of a device that quantitatively model individual aspects separately and then use the result in a complete and accurate device model are lacking. The aim of the present chapter is to achieve exactly this for a photovoltaic device, using a self-consistent 'building blocks' approach. First, the charge mobility in the constituent polymers will be reproduced through a thorough examination of the nature of polymer disorder. The disorder and mobility parameters deduced from this will then be used in an attempt to reproduce unilayer, unipolar J-V behaviour, from which the injection barrier can be deduced. Finally, these values will be combined with optical modelling in an attempt to reproduce the complete J-V and EQE characteristics of a PV device.

This will be achieved using the data of, and with reference to, the successful experimental and device modelling work of James Blakesley *et. al.* [62], performed at the Cavendish Laboratory, Cambridge. In that work, a sophisticated drift-diffusion model was applied to experimental data for devices using PFB and F8BT, which successfully reproduced device characteristics across a range of device temperatures and thicknesses. From this, the zero-field, zero-carrier density mobility values, μ_0 and γ, as well as the width of the Gaussian disorder, σ, were extracted for the two polymers. These data are considered to be far more precise than the more generic values used in Chapter 5. The work also provided insight as to the nature of this disorder, i.e. the possible presence of energetic correlations and/or traps. Developing a clearer understanding of the exact nature of polymer disorder and how it influences device behaviour is particularly pertinent in organic semiconductor physics. Various different research groups have found success in

applying different approaches (which will be outlined presently), and a consensus is yet to emerge.

The intention of the present chapter is to continue and expand the work of Blakesley *et. al.* [62], using the KMC approach. It will be structured as follows:

In Section 6.2, the nature of the energetic disorder in polymers and its effect on mobility will first be explored and quantified. This will be done in the case of single charge mobility, where the effects of disorder on mobility are separated from any charge density dependent effects, which will be explored in Section 6.3 instead. This is the simplest type of system that can be explored, and therefore makes an excellent first step to building up a complete and quantitatively accurate device model. By exploring the effects of disorder on mobility, a path can be found to reproducing the values of μ_0 and γ for PFB and F8BT that were deduced by Blakesley. This will be attempted whilst simultaneously remaining within the σ range deduced in that work. If successful, this will show that the KMC model is not only capable of reproducing experimental mobilities, but it can achieve this is a manner consistent with entirely independent drift-diffusion modelling. Furthermore, to create even closer agreement with experiment, this will be attempted whilst simultaneously reproducing Poole-Frenkel behaviour (described in Section 6.2.1) down to the lowest fields simulated, as is usually seen in experiment, but not necessarily in modelling. Given that the disorder description deduced will have to fulfil all three criteria (reproducing μ_0 and γ, within the σ range specified, whilst also reproducing PF dependence across all fields), it is likely to provide real insight into the nature of the disorder in polymers.

Having achieved this, the goal of Section 6.3 is to reproduce the unipolar behaviour of single layers of PFB and F8BT using the disorder parameters deduced for single charge mobility in Section 6.2. An accurate reproduction of unilayer device behaviour will indicate that the KMC code contains an accurate injection algorithm, and is also capable of successfully 'scaling up' from single charge behaviour to that of multiple, interacting charges. If this can be achieved using the disorder parameters already deduced, it lends credence to their accuracy. Given that these values will already have been deduced, the injection barrier, ϕ_B, will be the only parameter that can be modified. To ensure the injection rates for the first and all subsequent carriers are calculated accuracy, the injection simulations used in

this chapter employ the full Monte Carlo technique of recalculating every event waiting time at each timestep, so that the present state of the local electric field at possible destination sites is always taken into account. Utilising this instead of the FRM is more sophisticated than the models employed by others, and also more computationally intensive, but test simulations (not shown) reveal it makes enough difference to be necessary.

Finally, in Section 6.4, the disorder description from Section 6.2, and the injection barrier from Section 6.3, will be combined with optical modelling in an attempt to reproduce the J-V and EQE characteristics of a PV device, created from the same polymers and electrodes. This represents the final step of building up the device model, and if it can be achieved without modification of the parameters already deduced for simpler systems, will show the work to be self-consistent. Furthermore, consistent agreement with the work of Blakesley will show the two independent approaches (KMC and drift-diffusion) to be consistent with each other, whilst also validating the KMC code, providing more detailed insight into the device physics, and confirming the necessity of accurate optical modelling. This marks a clear distinction between the work described here and the modelling of other research groups - here, the final results will be built up from results from the simpler systems, with the same parameters used for each system studied, whether it be single charges, single polymer layers or complete devices.

6.2 Disorder and single charge mobility

The room temperature parameters deduced by Blakesley *et. al.* are [62],

PFB: σ =110 $\pm$ 10 meV, where $\mu_0 \approx 4 \times 10^{-12}$ m^2(Vs)$^{-1}$ and $\gamma \approx 6.4 \times 10^{-4}$ m$^{0.5}$V$^{-0.5}$.
F8BT: σ =100 $\pm$ 10 meV, where $\mu_0 \approx 2 \times 10^{-12}$ m^2(Vs)$^{-1}$ and $\gamma \approx 8.4 \times 10^{-4}$ m$^{0.5}$V$^{-0.5}$.

Each description of material disorder will be quantified in terms of μ_0, γ, and the extent to which PF dependence is reproduced; and hence evaluated as to how close it is to reproducing the behaviour of PFB. Except where stated otherwise, the prefactor in the charge hopping rate will be kept constant throughout all simulations. At the end of the section, the results of following the same procedure will be outlined for F8BT.

Mobility simulations are performed in the manner described in Section 3.2.3, over the field range $F^{0.5} = 1000 : 10000$ $(\mathrm{V/m})^{0.5}$, a range consistent with the work of Blakesley and others [62, 126, 77]. The result at each field value is averaged over 100 charges $\times$ 500 configurations of disorder.

In all simulations, the hopping rate was calculated using Marcus theory. Although this breaks from the trend used in nearly all previous simulations that utilise either the Monte Carlo or Master Equation approaches [37, 56, 83], it is felt that this theory better represents the underlying physics and can easily be linked to real parameters derived either from experiment or atomistic modelling [39]. It has already been used successfully when modelling charge transport alone [58, 39, 126], especially in a multiscale approach, though never, to the author's knowledge, in full current and injection modelling.

6.2.1 Poole-Frenkel behaviour

When analysing the field response of charged carrier mobility in semiconducting polymers, Poole-Frenkel (PF) type behaviour, where $\mu = \mu_0 e^{\gamma F^{0.5}}$, appears to be almost ubiquitous [82, 30, 127, 128]. The field dependence of the mobility is encapsulated in the field-enhancement factor γ, which has units of $\mathrm{m}^{0.5}\mathrm{V}^{-0.5}$. The origin of this behaviour is controversial [82], and possibilities that have been suggested include the nature of the field-lowering of the barriers between sites, which follows a $\delta V \propto F^{0.5}$ relationship (where V is the potential barrier height) [82, 127]; the nature of hopping motion itself, which follows a $ln(\mu) \propto F^n$ law, the value of n being dependent on the width of the DOS [30]; and a weakening of the dipole-related change in activation energy, $\delta F_0 \propto F^{2/3}$ [128]. It would seem from these explanations that Poole-Frenkel behaviour is concomitant with a disordered, trapping landscape, as this produces both field-lowered barriers and hopping motion. The question of charge transport is then brought more clearly into focus: exactly what form of disordered energetic landscape would best account for the observed behaviour?

Given the usefulness of the PF description, it is this that will be used as the basis for analysing the mobility data. In the results that follow, the field:mobility data was fitted to an exponential distribution using Matlab, and the Poole-Frenkel fit values μ_0 and γ extracted, along with the adjusted R^2 measure of the goodness of the fit. The R^2 value

is a measure of how well the data fits the PF description. As will be seen, deviation from PF behaviour always takes the form of a divergence between the PF description and the modelling at lower fields, as shown in Figure 6.1. Therefore, given the low amount of noise in the data (due to averaging over 500 configurations of disorder), the R^2 value is an indication as to how far across the field range the Poole-Frenkel relationship holds, i.e. how far it extends into lower fields. For visual clarity, and following convention, where graphs are included in the results below, the plot is of $\ln(\mu)$ vs. $F^{0.5}$. Therefore the linear region of the plot is that over which the PF description holds.

6.2.2 Gaussian disorder

Following the discussion in Section 2.2, it seems reasonable to model the site energies in the polymers as being drawn randomly from a Gaussian distribution, a method that was pioneered by Bässler and co-workers as the 'Gaussian Disorder Model' (GDM) [30]. This approach has been highly successful in reproducing the experimental field, disorder and temperature dependence of the mobility in a wide range of systems [62, 82, 129]. Whether by direct experimental measurements, or by modelling to fit experimental data, the standard deviation (Gaussian width) of the distribution, σ, is reckoned to be in the range of 50 - 190 meV [21, 130, 131, 132, 133, 134, 36, 117]. The Gaussian distribution of site energies, $g(E)$, is described by Eq. 6.1. In the KMC code, this is implemented using the Box-Muller transformation [135].

$$g(E) = \frac{1}{\sqrt{2\pi\sigma}} \exp\left(-\frac{E^2}{2\sigma^2}\right) \tag{6.1}$$

In the work presented below, the first set of simulations take a Gaussian distribution of site energies, with σ varied between 60 and 160 meV. In terms of the dimensionless disorder parameter, $\hat{\sigma} = \frac{\sigma}{k_B T}$, this is equivalent to a range of approximately $\hat{\sigma} = 2.4$ to 6.4 at 295 K.

Results

As an introduction to these results, Figure 6.1 shows an example mobility-field plot for the GDM. In this case, $\sigma = 110$ meV, and the field is varied from 10^3 to 10^4 $(\mathrm{V/m})^{0.5}$. It is clear that in the GDM, the PF description holds, at best, only at high field. In this example, the adjusted R^2 measure of the goodness of fit is 0.9795, whereas a value > 0.99 is desirable (1.0 being a perfect fit). Both μ_0 and γ can be extracted from fitting the PF equation to these data; though clearly the lower the goodness of fit, the less reliable the extracted parameters are. For this reason, a second fit is performed at higher field values, with F $\geqslant$ 6000 $(\mathrm{V/m})^{0.5}$, where the match to the PF equation is closer. Both fits were performed for mobility:field simulations across the range of σ values, and the values are compared below.

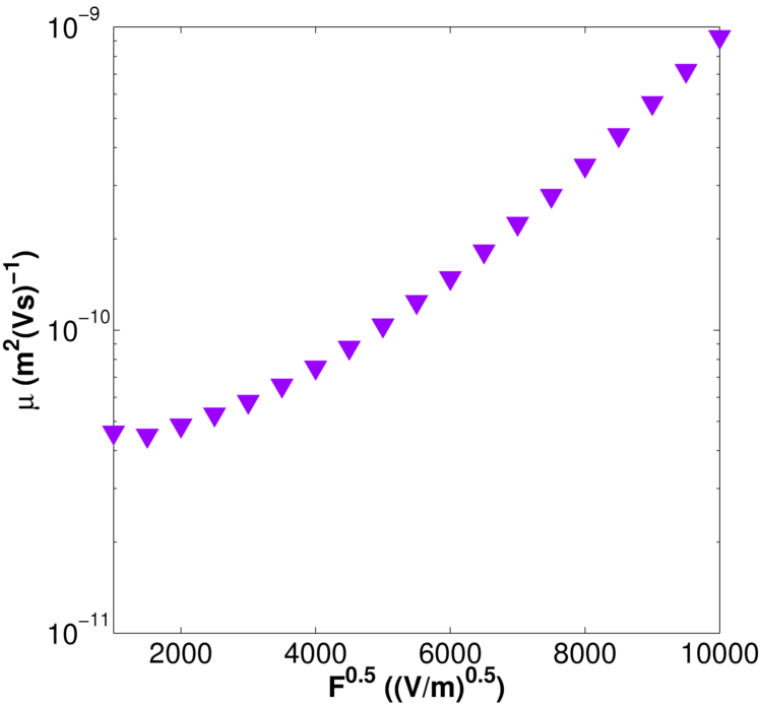

Figure 6.1: Mobility-field plot for the GDM, with $\sigma = 110$ meV.

Figure 6.2 shows $\mu_0(\sigma)$, extracted from fitting the PF equation across the entire field range and from fitting at high field (F $\geqslant$ 6000 $(\mathrm{V/m})^{0.5}$) alone. Both sets of data

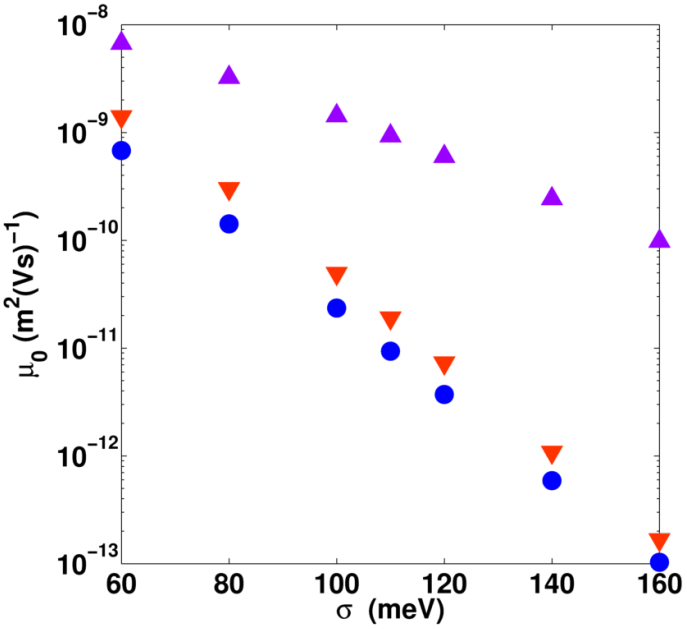

Figure 6.2: $\mu_0(\sigma)$ from fitting across the entire field range (▼), and from fitting at high field alone (●). Also shown is $\mu(\sigma)$ for F = 10000 $(\mathrm{V/m})^{0.5}$ (▲).

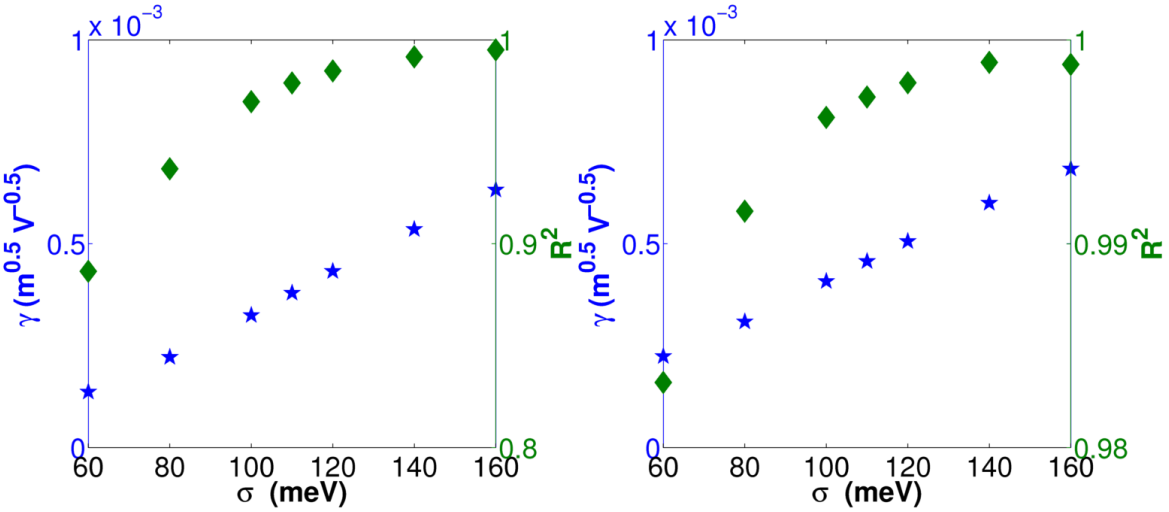

(a) (b)

Figure 6.3: $\gamma(\sigma)$ and $R^2(\sigma)$ for the GDM from fitting across the complete field range (a); and from fitting at high field only (b).

an exponential decrease in μ_0 with σ, with the values extracted from fitting above 6000 $(\mathrm{V/m})^{0.5}$ being slightly lower than those from fitting all the data points, due to extrapolating from the steeper part of the mobility-field curve. Expressed in terms of $\hat{\sigma}$, these data show the same Arrhenius type relationship of $\mu_0(T) = \mu_{00} \exp\left(-(a\hat{\sigma})^2\right)$ that was seen in the seminal work on the GDM by Bässler *et. al.* [30], with a = 0.55 when fitting across the entire field range. However, as in that work, in the present simulations it is actually σ that is being varied, not T. Bässler also found a deviation from Arrhenius behaviour at low $\hat{\sigma}$, perhaps not seen in the present work due to using higher values of $\hat{\sigma}$ (>2.4). Also shown is $\mu(\sigma)$ for F = 10000 $(\mathrm{V/m})^{0.5}$. At this higher field value, the σ dependence is reduced, due to the increased dominance of the field in determining the hopping rate. Therefore, $\mu(\sigma)$ is field dependent, creating a divergence between the high and low field values of μ as σ is increased.

This explains the linear dependence of the γ value on σ, which is essentially a measure of the difference between the high and low field mobility. Figure 6.3 (a) shows that γ increases linearly from 1.4×10^{-4} $(\mathrm{V/m})^{-0.5}$ to 6.3×10^{-4} $(\mathrm{V/m})^{-0.5}$ as σ is increased from 60 meV to 160 meV. This is in contrast to Tonezer and Freire [129], who found a quadratic dependence for the GDM. However, the model used in their publication implemented the Miller-Abrahams description of hopping rates instead of the Marcus description used here, and only allowed nearest neighbour hopping, which the present work shows to be inadequate (see Section 6.2.3). As stated above, the MA rate, although functional, is purely phenomenological, whereas the Marcus rate more accurately reflects the actual charge hopping process, which is why it is implemented in multiscale modelling. Therefore, the result presented here is believed to be closer to what would be observed in experiment if the σ value of a polymer could be modified independently of all other relevant parameters, such as the reorganisation energy. In practise, different energetic widths come from different polymers, so this could not be attempted.

When fitting at higher field only, γ maintains the same linear dependence on σ, although the values are slightly higher due to fitting to the steepest part of the mobility-field gradient. The R^2 goodness of fit exhibits almost exactly the same trend as before, but with values now much higher, as shown by the axis rescaling. This shows that, even at field values above 6000 $(\mathrm{V/m})^{0.5}$, the field dependence is still not fully PF-like, though it approaches it very closely at 160 meV (R^2 = 0.9988, and accepting some deviation from 1.0 due to noise).

It has so far been shown, from Fig 6.1, that PF dependence only holds at higher field values, with the mobility diverging from this trend at lower field. Comparison of Figures 6.3 (a) and (b) shows that the adjusted R^2 value increases at the higher field range, which is an alternative way of expressing the same result. Figure 6.3 also shows that the adjusted R^2 value increases with σ, saturating as it approaches 1.0. Therefore, the greatest divergence from the PF relationship occurs at both low field and low disorder. These two results are consistent with one another: increasing the field will increase the typical energetic spacing between sites, as will increasing the value of σ. Both create a closer match to the PF description. At low fields and/or low values of disorder, the typical inter-site energetic spacing decreases to the point where the PF description no longer holds, due to the barriers between sites being particularly low. This shows that the PF description does not result from the hopping motion alone, but is a result of the barrier size between sites.

Overall, as σ increases, the value of μ_o decreases exponentially; the value of γ increases linearly; and the goodness of fit also increases, approaching unity at σ = 160 meV ($\hat{\sigma}$ = 6.4) for the field range considered. Increasing the disorder increases not only the magnitude of the response to changing field, producing a larger range of mobility values as characterised by γ; but also the field range over which the response is exponential, following the PF description. At σ =110 meV, $\gamma = 3.78 \times 10^{-4}$ $m^{0.5}V^{-0.5}$ and R^2 = 0.9795, showing that the GDM is incapable of reproducing the Blakesley result. The desired γ value and goodness of fit are approached at σ =160 meV, where $\gamma = 6.33 \times 10^{-4}$ $m^{0.5}V^{-0.5}$ and R^2 = 0.9951. However, alternative means of achieving the mobility of PFB whilst still remaining within the range 110 $\pm$10 meV will now be investigated, based on other description of material disorder.

6.2.3 Correlated disorder

As has just been shown, the limitation of the GDM is that the PF description only holds at high field, whereas in experiment, such as TOF observations, PF dependence usually continues to much lower fields [62, 129, 136, 38, 37]. In 1995, Gartstein and Conwell reported that correlating the energy of proximal sites could extend the field range over which PF behaviour is observed, creating a closer agreement with experiment [82]. This 'correlated disorder model' (CDM) was subsequently applied by Dunlap [137] and later

Novikov [136], who extended the work to three dimensions. In this section, the CDM will be implemented, and its effect on the mobility quantified. Intuitively, as increasing the PF range extends the high field mobility dependence to low field as well, there should be a resulting increase in γ. Therefore, the CDM should produce mobility results closer to those desired for PFB, by extending both the PF range the γ value, both of which were insufficient in the GDM.

Spatial energetic correlation have been observed in some materials [117, 131], and as well as better reproducing the PF field dependence of the mobility, can also be used to account, in some materials, for the level of charge trapping at heterojunctions and hence geminate pair behaviour [89]. The origin of the energetic correlations has been attributed to various causes, such as the interaction of carriers with an ensemble of randomly oriented electric dipoles, or to thermal fluctuations of the molecular geometry, combined with steric restoring forces [129]. Although there exists a variety of physical explanations behind correlation, and hence different correlation functions with different distance dependencies of the correlation strength, in this present work the exact nature of the correlations are not the point of interest, simply that the principle of energetic correlation be implemented in a physically reasonable way. Hence, in the same manner as [89], the method applied here will follow the seminal method of Gartstein and Conwell.

To achieve this, all sites in the system are initially randomly assigned an energy from a Gaussian distribution, as with the GDM. The energy of each site, ε_i, is then recalculated by finding the mean energy of all the sites within a specified cutoff ξ_c. This value is then multiplied by the square root of the number of sites taking part in the average, n, to give the correlated site energy ε_c,

$$\varepsilon_c = n^{-\frac{1}{2}} \sum_{i=1}^{n} \varepsilon_i \tag{6.2}$$

This produces short-range correlations, with an inverse distance decay [129], but which retain an overall Gaussian distribution of site energies with the same width σ [82]. As with the origin and method of correlation, the correlation range is also debatable, but may be up to several multiples of the lattice constant a [138, 139, 140]. Blakesley *et. al.* [62] concluded that correlated disorder may very well be present in the conjugated polymers used in optoelectronic devices, although this conclusion is not necessarily sup-

ported by other work, where is has often proved unnecessary to include correlations in order to accurately reproduce device behaviour [36, 141, 37]. The question as to whether correlated disorder is present in devices and required in modelling therefore remains open.

In the following results, the impact of varying the correlation range ξ_c in the CDM will be evaluated in much the same way that the impact of varying σ in the GDM was evaluated in the previous section. Simulations have been run for ξ_c/a = 1,2,3,4,5, corresponding to n = 6, 32, 122, 256 and 514 neighbours respectively. Furthermore, the maximum hopping range of the charges, denoted ξ, will also be varied to investigate the extent to which variable range hopping is observed.

Results

Figure 6.4 shows that by adding energetic correlations, the R^2 goodness of fit first increases as predicted, peaking at a value of $\xi_c = 2$, before falling again. As PF dependence is already seen at higher fields in the absence of correlations, the increase in R^2 can only be attributed to the extension of this dependence to lower field values, as is illustrated in Figure 6.5. This also explains the increase in γ, as, when increasing the range of correlation, the low field mobility values are 'pulled down' into alignment with an ever-steeper PF dependence at high field. This results in a modest decrease in $\mu_0(\xi_c)$ (not shown for brevity). The intermediate peak in $R^2(\xi_c)$ is consistent with the work of others [82, 129]. Following Gartstein and Conwell, these trends may be explained as follows. Correlating the site energies creates a smoothing of the energetic landscape of the system, on the scale of ξ_c, as illustrated in Fig. 6.6. The result is that the energetic barriers that a charge must traverse now have a greater spatial extent. This renormalises the effect of the applied field by the same spatial extent. The result is that higher field effects, such as the closer match to the PF description of mobility, now have an onset at lower fields, thus explaining the initial increase in $R^2(\xi_c)$. It is speculated that the intermediate peak, and subsequent decrease in $R^2(\xi_c)$ are due to very high field effects, outside the range examined in the preceding section. At very high fields, much greater than those normally encountered in polymer electronic devices, the PF dependence is once again lost, and in fact PF dependence is only found in an intermediate field range overall, as illustrated in Figure 6.7. Therefore, as correlating the site energies shifts higher field effects to lower

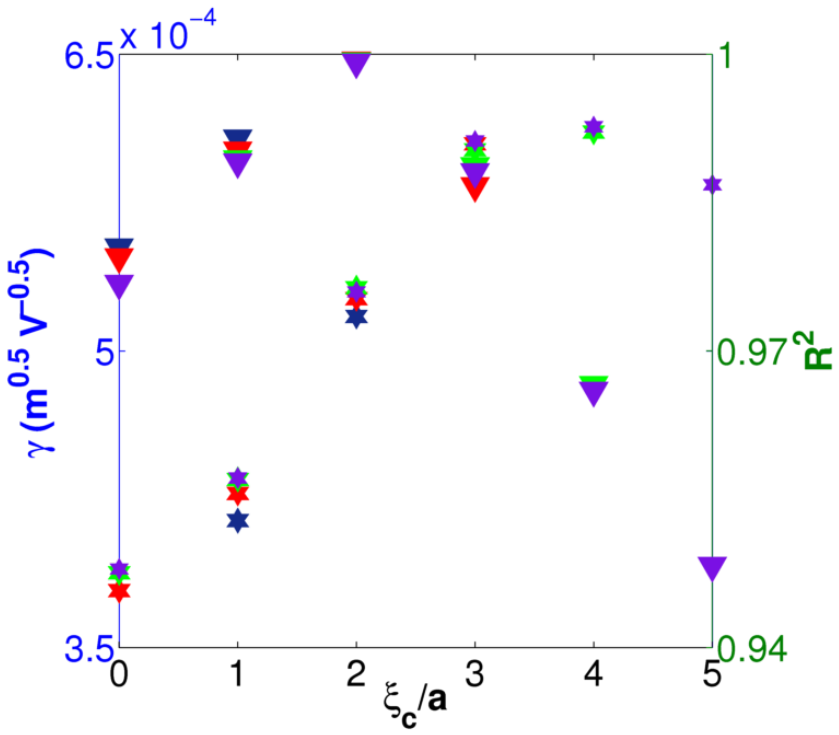

Figure 6.4: $\gamma(\xi_c)(*)$ and $R^2(\xi_c)(\blacktriangledown)$ for the CDM at σ =110 meV. Results are for ξ/a = 2 (navy blue), 3 (red), 4 (green) and 5 (purple).

fields, if the spatial extent of the correlations, and hence the renormalising of the field, is extended to a sufficient range, it is speculated that these very high field effects will eventually be seen at the field values examined in this study. This explains why the PF dependence decreases again at high ξ_c - it is simply reflecting effects seen at very high field.

In terms of ξ (variable range hopping), Figure 6.4 show that the values of γ and R^2 exhibit almost no variation with hopping range, with results from the different studies overlapping each other to within $\approx 5\%$ for any given value of ξ_c. The values of $\mu_0(\xi)$

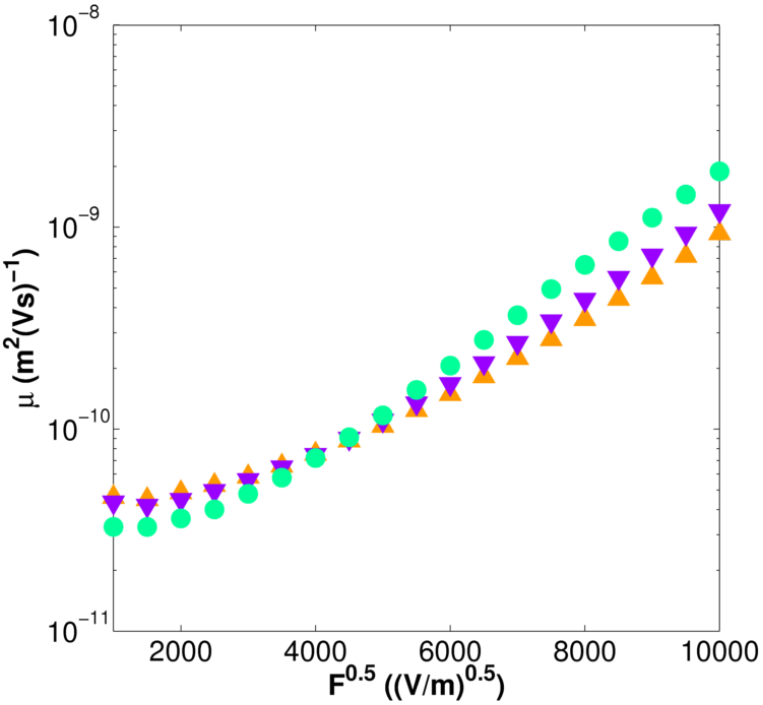

Figure 6.5: Mobility-field plot for the GDM (▲), CDM ($\xi_c = 1$) (▼) CDM ($\xi_c = 2$) (●) for $\sigma = 110$ meV.

for the same dataset (not shown for brevity), also exhibit virtually no variation with hopping range, for $\xi \geqslant 3a$. However, when the hopping range drops below $\xi = 3a$, there is a shift of 20-30% at each value of ξ_c. This suggests that, for these parameters and a pure morphology, variable range hopping up to $\xi = 3a$ is occurring, but not beyond this range. As a result, a maximum hopping range of $\xi = 3$ will be implemented for all future simulations in order to avoid wasting computing time.

Depending on the range of correlation, implementing the CDM can increase both the field range of the PF dependence and the value of γ, when compared to the GDM for the same level of disorder. At σ =110 meV, and the (optimum) correlation range of $\xi_c = 2$, $\gamma = 5.27 \times 10^{-4}$ $\mathrm{m}^{0.5}\mathrm{V}^{-0.5}$ and $R^2 = 0.9994$. However, the PF dependence still does not extend down to the very lowest fields, as it does in experiment, instead diverging below ≈ 6000 $(\mathrm{V/m})^{0.5}$ for this result. Furthermore, the values of γ achieved thus far are still too low to be consistent with the findings of Blakesley *et. al.* [62] for PFB. In all the results so far, the deviation of the mobility-field relationship from the exponential fit is pro-linear, i.e. when plotted in the form of Figure 6.5, the mobility values level off at

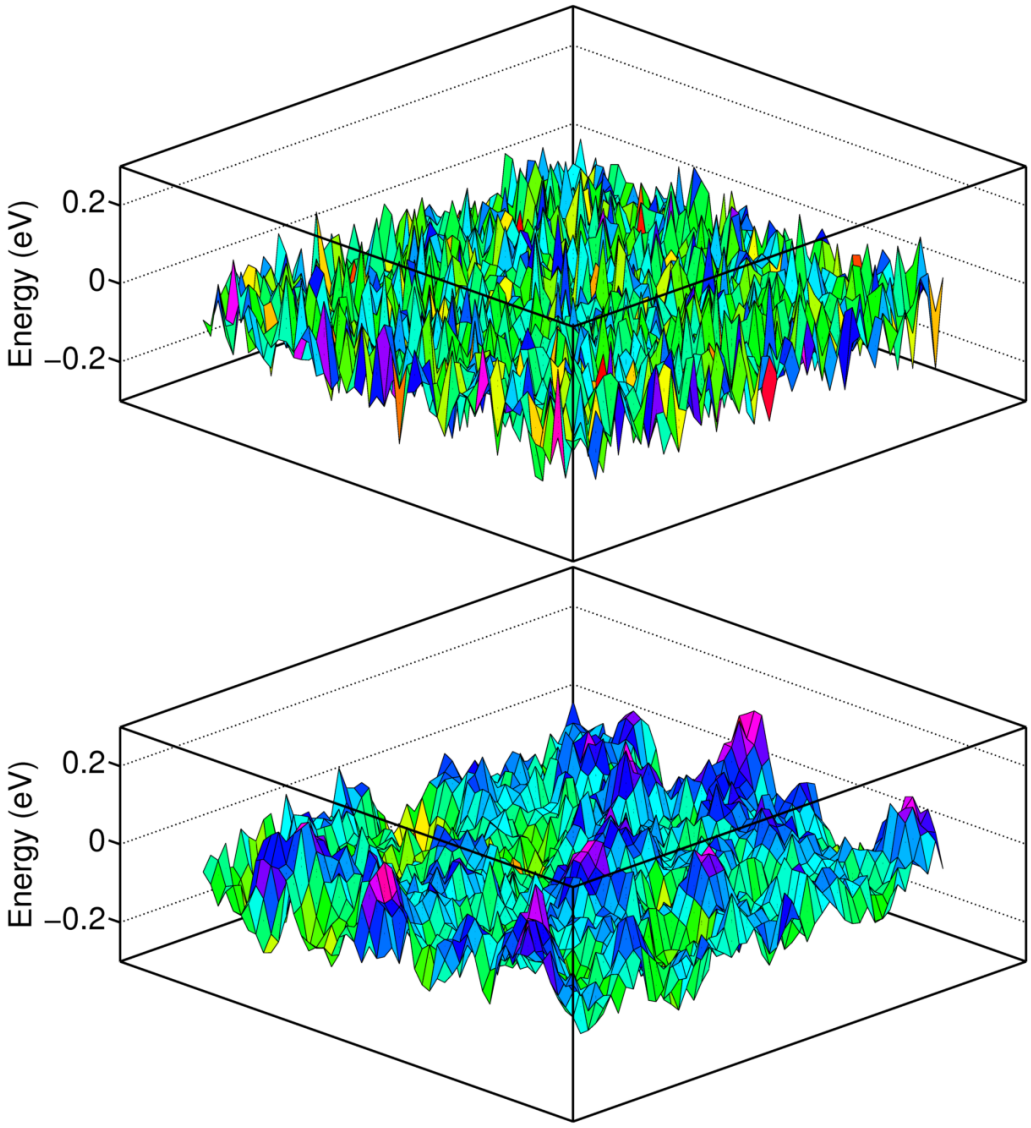

(b)

Figure 6.6: Energetic landscape in the GDM (a); and in the CDM with $\xi_c = 3$a (b).

low field instead of continuing to decrease linearly. Clearly, therefore, a variation on the disorder description must be found that extends the PF dependence, and hence γ, still further, in order to bring the mobility description into alignment with that of PFB.

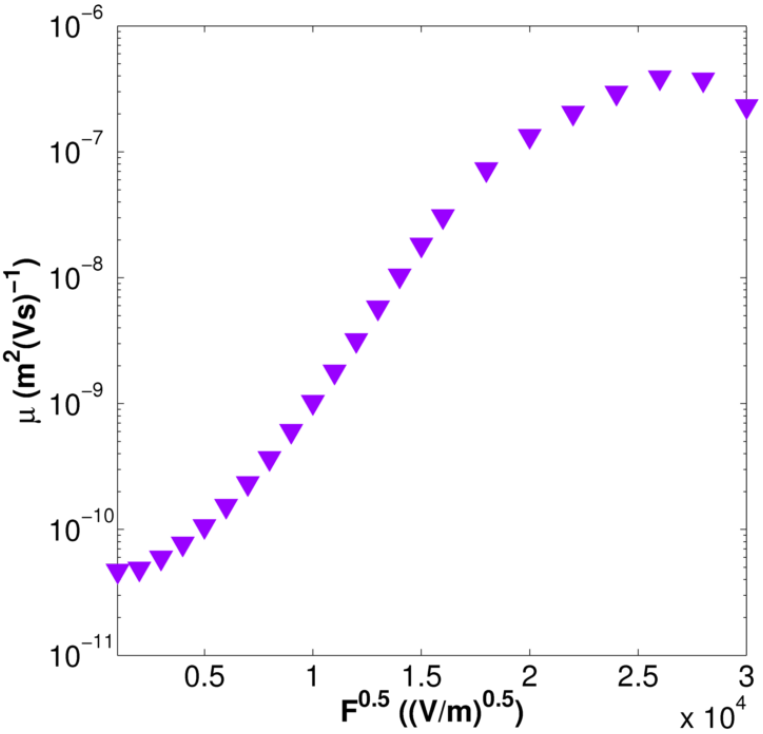

Figure 6.7: Mobility plot up to high field for the GDM, with $\sigma = 110$ meV.

6.2.4 Exponential trap distributions

When examining the charge transport characteristics of polymer devices, the possibility of an exponential distribution of trapping sites, in addition to or instead of the primary Gaussian disorder, has sometimes been suggested. Chatten *et. al.* [126] and Kaake *et. al.* [138] both suggest a bimodal distribution of the density of states, consisting of both Gaussian disorder and an exponential distribution of deeper traps within the bandgap. In Chatten, the use of this form of distribution is justified from the exponential dependence in transient optical data on films of MDMO-PPV:PCBM, and by assuming that the change in absorption in this data is proportional to the polaron density, implying an exponential density of trap states. It was found that this approach created a better agreement between the data and Monte Carlo modelling. Kaake attributes the physical origin of charge trapping to intrinsic minority charged defects, though never presents a mathematical description. Other groups [142, 143, 144, 132] use an exponential trap distribution alone, as a functional alternative to the GDM for reproducing the desired mobility-field results, without necessarily providing a physical justification for the math-

ematical form. Steyrleuthner *et. al.* states that electron-accepting defects can form during device synthesis and fabrication, and even as the result of oxidation, processes which are sensitive to the depth of the LUMO level [144]. Whatever the exact physical origin(s), the possible use of an exponential distribution of trapping sites seems to be widely justified, and will be explored here as a means of reproducing the desired mobility values.

The distribution of trap states has the generic form,

$$g(E) = \frac{1}{k_B T_0} \exp(\frac{E}{k_B T_0}), \tag{6.3}$$

where T_0 is the characteristic temperature of the trap distribution. Expectation values can be generated in the same way as for the solution to the Master Equation at the heart of the FRM (Section 3.1.2). That is,

$$E = \frac{-ln(U)}{\lambda} \tag{6.4}$$

where

$$\lambda = \frac{1}{k_B T_0} \tag{6.5}$$

Where the U is a random number, uniformly distributed between 0 and 1.

The trap density φ and the trap depth, parametrised in terms of the characteristic temperature T_0, constitute two material-dependent variables. As with the disorder width and the correlation range, it is essential to establish a realistic range within which these values may be varied. Chatten, modelling blends of MDMO-PPV with varying ratios of PCBM, found good fits to experiment for values of φ between 0.1% and 2%; and a characteristic temperature $T_0 = 750$ K. They note that, *'In general the degree of disorder in dispersive conjugated polymer films such as MDMO-PPV is very sensitive to processing conditions. Therefore we do not find it unreasonable that the density φ of localised states*

required in order to obtain agreement between the model and experiment varies by an order of magnitude between studies.' Kaake *et. al.*, in their discussion of intrinsic charge trapping, note that *'Coulomb traps are poorly screened, and trapping energies many times k_BT are to be expected.'* Montero *et. al.* [142], modelling an energetic landscape containing only an exponential trapping distribution, with no Gaussian disorder, used a value of $\varphi = 0.01\%$ and $T_0 = 1500$ K, although they do not model a specific polymer, use a much narrower field range when calculating mobility (5000 - 10000 $(\mathrm{V/m})^{0.5}$), and make use of an undefined 'trapping coefficient' of $\gamma = 1.1 - 2.2 \times 10^{-4}$. Steyrleuthner *et. al.* [143] successfully reproduce the characteristics of F8BT using a trap density of $\varphi = 0.1\%$ and characteristic temperature $T_0 = 1200$ K, which corresponds to a width of around 100 meV, similar to that suggested by Blakesley *et. al.* [62] when modelling F8BT using Gaussian disorder. Steyrleuthner assumes the Mark and Helfrich model of an exponential trap distribution [145], but does not try to justify its origin.

It therefore seems reasonable that values of φ up to 2% and T_0 up to several k_BT may be used to reproduce the mobility results for PFB and F8BT. In addition to the physical justification for a bimodal energy distribution that has already been outlined, its necessity is further suggested by the use of the CDM. Correlating disordered site energies significantly reduces charge trapping, which, as will be shown, is a prerequisite for carrier density dependent mobility (see Section 6.3.1). The creation of a two-tier electronic landscape, consisting of correlated disorder with a secondary layer of traps, restores the possibility of trap filling at higher current densities. This will become desirable in the following section for the modelling of unilayer devices which use the same polymers being explored in terms of single charge mobility in the present section.

In this section, φ and T_0 will be varied, and as in the previous sections, the aim is not only to quantify the effect on single charge mobility, but also to find a path towards reproducing the desired mobility-field characteristics for PFB.

Results

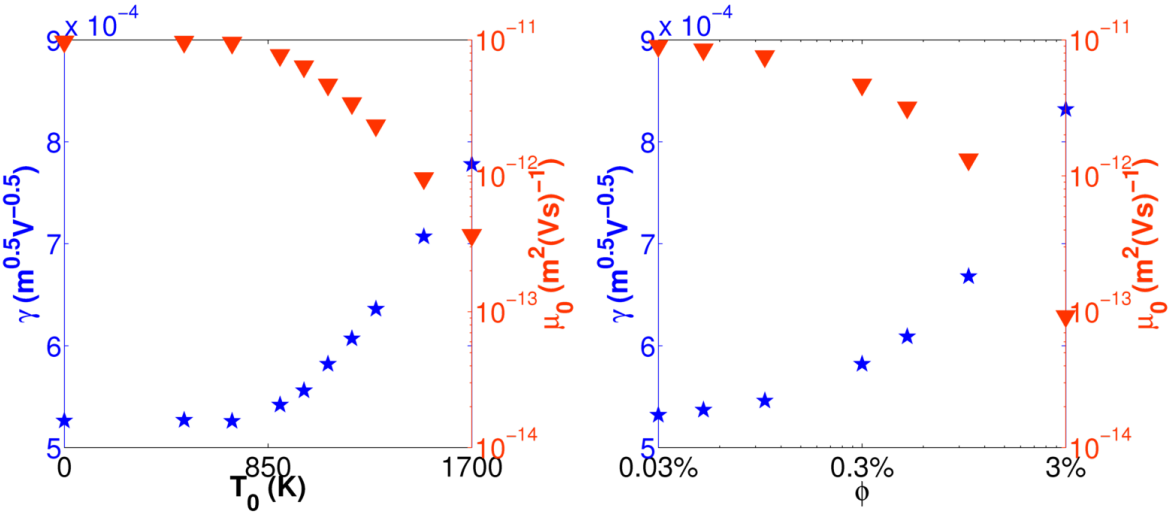

(a) (b)

Figure 6.8: Dependence of μ_0 and γ on (a) T_0 ($\varphi = 0.003$); and (b) φ ($T_0 = 1100$ K).

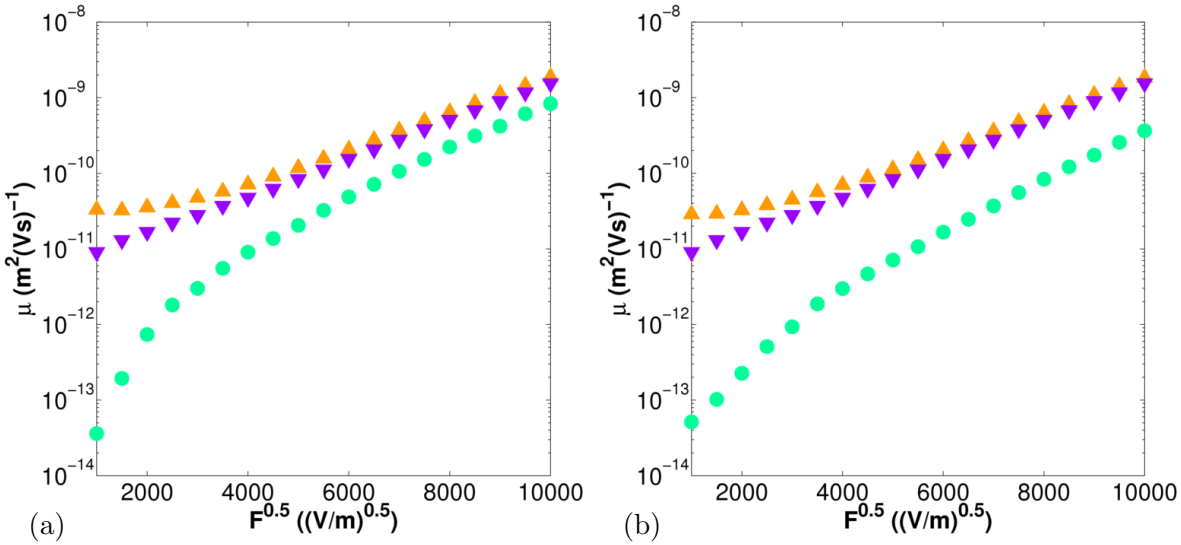

(a) (b)

Figure 6.9: Example plots of trap dependence of mobility-field relationship. (a) Shows results, holding $\varphi = 0.3\%$, for $T_0 = 500$ K (▲), 1100 K (▼) and 1700 K (•). (b) Shows results, holding $T_0 = 1100$ K, for $\varphi = 0.03\%$ (▲), 0.3% (▼) and 3% (•).

For all the results in this section, the variation in R^2 is too small to draw conclusions from in terms of the extent of the PF dependence, and so it is not shown. However, as will be seen, this can be done from the mobility-field plots themselves. Figure 6.8 (a)

shows $\mu_0(T_0)$ and $\gamma(T_0)$ for $\varphi = 0.3\%$. The results reveal that μ_0 is highly sensitive to trapping, decreasing by almost two orders of magnitude as T_0 is increased from 0 up to 1700 K. This result is further illustrated in Figure 6.9 (a), which shows how the shape of the mobility-field curve changes as T_0 is increased. As has already been seen, particularly in Section 6.2.2, the effect of trapping is clearly field dependent. At lower fields the trap depth is large, relative to the potential difference induced between sites by the field; and furthermore, charges within smaller fields are likely to have a greater number of trap encounters. Conveniently for the present purposes, these effects extend the PF range, because the lower, non-linear, end of the mobility-field plots are more greatly affected. As can be seen in Figure 6.9 (a), increasing T_0 pulls the low field mobility values down into the same PF trend as the higher field values, before pulling them down further, reducing the PF range again. An ideal intermediary is inevitable, where the PF range extends across all fields as desired, and for $\varphi = 0.3\%$, is found at $T_0 = 1100$ K. The greater sensitivity of the mobility to trapping at lower fields results in γ increasing with T_0, in much the same way it does with σ (see Section 6.2.2).

Holding T_0 at this optimum value of 1100 K, the trap density φ was then varied either side of the optimum value of 0.3%, the results of which are shown in Figure 6.8 (b). Varying φ has a similar effect to varying T_0, suggesting trap density and depth to be qualitatively equivalent in terms of their effect on single charge mobility, at least within the range explored. Figure 6.9 (b) illustrates this further, showing that increasing φ changes the shape of the mobility-field curve in much the same way as T_0 does. The equivalency of T_0 and φ can also be tested by searching for additional combinations of φ and T_0 that produce the same mobility-field curve (see Section 6.2.5).

For $\sigma = 110$ meV, the optimum trap combination, in terms of PF range, creates a γ value of 5.8 $\times 10^{-4}$ $m^{0.5}V^{-0.5}$. This is still short of the PFB value of 6.4 $\times 10^{-4}$ $m^{0.5}V^{-0.5}$. However, a similar procedure to that performed above can be followed for other values of σ, whilst remaining within the range of 110 $\pm$ 10 meV specified by Blakesley *et. al.* [62]. It was found that for 115 meV disorder, a trap combination of $\varphi = 0.3\%$ and $T_0 = 1225$ K produces not only the desired values of γ and μ_0, but also achieves these with the PF dependence extended down to the lowest fields, as desired.

Therefore, it has been shown that the mobility of PFB, as derived by Blakesley *et. al.* [62], can not only be reproduced using the Monte Carlo model, it can be reproduced within the disorder range specified, whilst simultaneously following the PF description

across the entire field range, as is usually encountered in experiment. This shows the two modelling approaches (the present KMC model and Blakesley's drift-diffusion model) to be consistent, at least for single particle simulations where density-dependent effects are not applicable. This result will be explored further before attempting to reproduce the experimental result for F8BT in Section 6.2.7.

6.2.5 Identifying different trapping combinations

Although a functional trapping distribution has been identified for reproducing the mobility-field relationship of PFB, there is no reason to think this particular combination of T_0 and φ is a unique solution. To this end, further simulations were carried out to see if these values could be modified and still produce the same mobility-field relationship. It was found that, for $\sigma = 115$ meV, trapping combinations of 0.1%, 1600 K and 0.9%, 1050 K could produce very similar mobility results to the trapping combination of 0.3%, 1225 K, discussed in the previous section. This suggests that the proportion of trapping sites and the trap depth are indeed equivalent, at least within a limited range. Whether these trap distributions, which produce nearly identical mobility-field relationships, produce different results for multiparticle, J-V behaviour, will be explored in Section 6.3.2. Additionally, further simulations showed that varying σ and ξ_c in the presence of traps reproduces the same *trends* as seen in Sections 6.2.2 and 6.2.3 in the absence of traps.

6.2.6 Using a trap distribution alone

Finally, in line with the work of [142] and [143], mobility simulations were run in the presence of an exponential trap distribution alone, with no Gaussian disorder. Simulations were run for $T_0 = 250$ K to 750 K, and the results are summarised in Figure 6.2.6.

It was found that, at $T_0 = 450$ K, this approach could reproduce the same quality of fit to the PFB data that was achieved using a bimodal energetic distribution, in Section 6.2.4. The prefactor in the Marcus hopping rate, ν (defined in Section 2.4.6), had to be scaled by a factor of ≈ 4, due to applying a completely different trapping distribution.

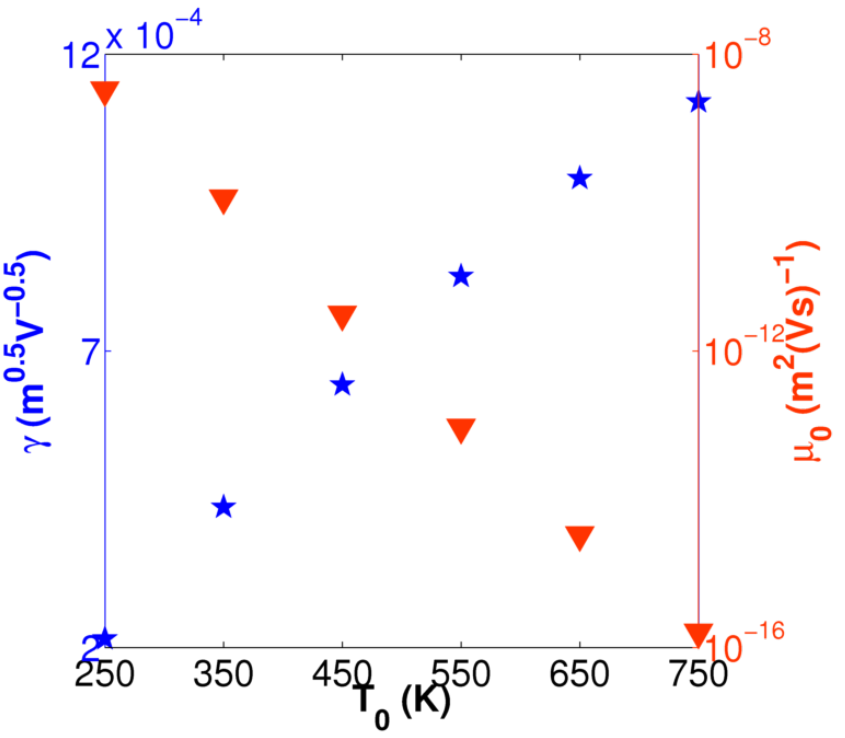

Figure 6.10: Dependence of γ and μ_0 on T_0, when using an exponential trap distribution alone.

However, as has been described earlier, this is simply a scalable constant, which does not affect the field *dependence* of the mobility, and has been kept constant in all the results so far. The equivalence of an energetic distribution based around the GDM, and a purely exponential distribution, was noted in the work of Blakesley *et. al.* [62], and the value of T_0 calculated in this present work is remarkably similar to those calculated by Tanase *et. al.* [132]. The results presented here would appear to support the idea that these two approaches to modelling the energetics are indeed equivalent, at least in the realm of single charge mobility. This idea will be explored further in Section 6.3, in the context of full J-V modelling.

6.2.7 F8BT

Following the procedure described above for PFB, an energetic distribution was sought that could reproduce the mobility of F8BT. This was deduced by Blakesley *et. al.* [62] to be $\mu_0 \approx 2 \times 10^{-12}$ $m^2(Vs)^{-1}$ and $\gamma \approx 8.4 \times 10^{-4}$ $m^{0.5}V^{-0.5}$, for a disorder width of σ =100 $\pm$ 10 meV. Compared to PFB, this constitutes achieving a higher γ value for a lower value of σ, which runs contrary to the findings so far, and the only way to achieve this is to compromise the extent of the PF dependence. A reasonable fit was found for φ = 3%, T_0 = 1100 K, although PF dependence is only reproduced at fields above ≈4000 $(V/m)^{0.5}$ for these parameters, as opposed to down to the lowest simulated value of 1000 $(V/m)^{0.5}$, which was achieved for PFB. Further simulations suggest a similar result can be obtained for φ = 0.3%, 1900 K $\leqslant T_0 \leqslant$ 2000 K, although high T_0 results are less clear due to high levels of noise, especially at low field.

In an effort to create the same quality of fit as was achieved for PFB, σ was varied outside the range specified by Blakesley *et. al.* [62], but still remaining within the range suggested in the literature (see Section 6.2.2), and keeping the same correlation range. Following this approach, an excellent fit can be achieved for σ = 160 meV, φ = 0.3%, T_0 = 1100 K. This trap distribution is near-identical to that of PFB, suggesting both may have the same origin, with only the overall disorder value increased. Alternatively, a close fit can be found when using a trap distribution alone, removing Gaussian disorder entirely, in the same manner as Section 6.2.6. In this case, an excellent fit can be found for a characteristic trap temperature of 560 K, again very consistent with the work of Tanase *et. al.* [132].

6.2.8 Conclusions from Section 6.2

This section has systematically investigated how mobility varies within the context of the GDM, CDM, and with the introduction of a trapping distribution, both with and without Gaussian or correlated disorder. Along with the conclusions drawn in each section which quantify and explain the role of the various applicable disorder parameters, disorder descriptions that can reproduce the mobility-field relationship of PFB and F8BT have been found. The criteria established at the beginning of the section was to reproduce the values of μ_0 and γ, as deduced by Blakesley *et. al.* [62] using drift-diffusion modelling,

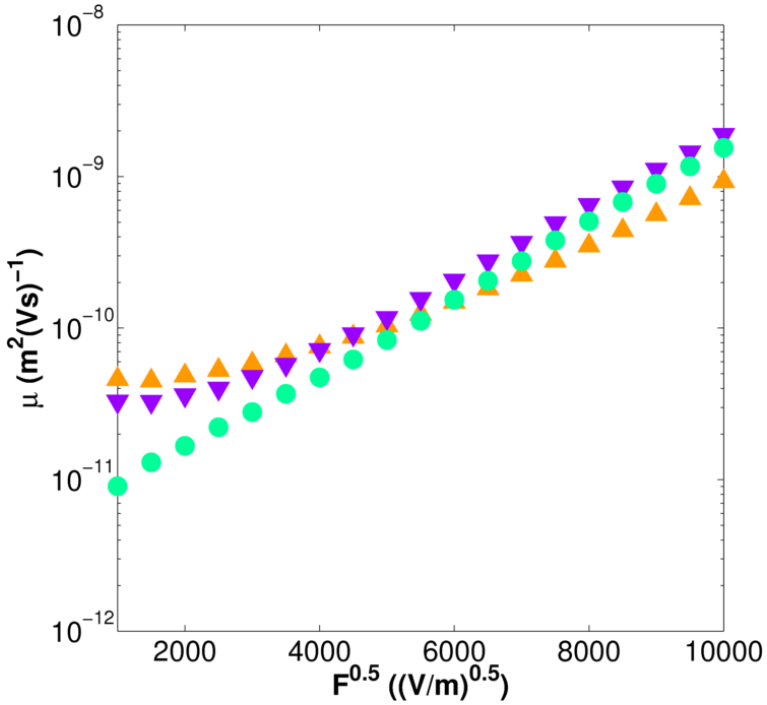

Figure 6.11: Example plots of the GDM (▲), CDM (▼) and CDM combined with traps (●) for σ = 110 meV. These examples highlight how the PF range can be extended by applying the different methodologies.

within the same σ range deduced in that work, whilst also reproducing PF dependence across the entire field range. These values were:

PFB: σ =110 ± 10 meV, where $\mu_0 \approx 4 \times 10^{-12}$ $m^2(Vs)^{-1}$ and $\gamma \approx 6.4 \times 10^{-4}$ $m^{0.5}V^{-0.5}$.
F8BT: σ =100 ± 10 meV, where $\mu_0 \approx 2 \times 10^{-12}$ $m^2(Vs)^{-1}$ and $\gamma \approx 8.4 \times 10^{-4}$ $m^{0.5}V^{-0.5}$.

For PFB, this was achieved for σ = 115 meV, a correlation range of ξ_c = 2, and a trapping distribution of T_0 = 0.3%, φ = 1225 K, although other functional trapping distributions were also found. The value of σ therefore falls within the range specified by Blakesley, whilst also containing correlations, which were suggested in the same work. In Blakesley's modelling, the need to include an explicit trap distribution is specifically denied, although the work does concede that the GDM and exponential trap distribution models might both describe similar underlying physics. This was suggested because the disorder width (σ) deduced by Blakesley for F8BT (100 ± 10 meV) is very similar to the characteristic energy of the trap-only distribution deduced by Steyrleuthner (≈ 100 meV)

for the same polymer [143]. Furthermore, in private correspondence with Blakesley, it was suggested that a distribution of trapping states might exist after all. Therefore, the two approaches, the present KMC model and Blakesley's drift-diffusion model, are seen as being extremely consistent with one other.

For F8BT, a reasonable fit can be found, whilst remaining within the range of σ specified by Blakesley. However, the quality of fit to the Poole-Frenkel relationship that could be achieved whilst contraining σ in this way was lower than was achieved for PFB. This was perhaps to be expected, as Blakesley deduced a higher γ value for F8BT, whilst simultaneously having a lower σ value, which runs contrary to the well-established trends of the GDM, both here and elsewhere [30]. In an attempt to create a closer fit, σ was varied outside the range specified by Blakesley, but the value was still constrained to what might be considered reasonable, based on other reports in the literature. An excellent fit to Blakesley's values for μ_0 and γ was achieved for σ = 160 meV, ξ_c = 2, φ = 0.3%, T_0 = 1100 K. The correlation range and trap distribution are near-identical to that of PFB, suggesting these two polyfluorenes to be innately similar.

It was also found that both of these fits could be reproduced using an energetic landscape consisting of a trap distribution alone, with no Gaussian or correlated disorder. Excellent fits could be found at T_0 = 450 K and 560 K for PFB and F8BT respectively, values very similar to those of Tanase *et. al.* [132].

It may be argued that, given the variety of correlation ranges and trapping distributions that can be applied to a particular width of Gaussian disorder, that there are, in fact, a wide variety of σ values that could be made to produce the desired mobility for PFB. This would suggest that there is nothing special in achieving this mobility whilst keeping σ within the range specified by Blakesley *et. al.* [62], that in fact the same result could be achieved for other, very different values. However, the process that has been followed must be remembered carefully. The target was not just to create the desired values of μ_0 and γ, it was to reproduce them whilst also reproducing PF dependence across the complete field range, down to 1000 $(\mathrm{V/m})^{0.5}$. The choice of correlation range was not arbitrary, the range of ξ_c = 2 extended the PF dependence the most, so this had to be chosen. Likewise, the amount of trapping could not be freely varied until the desired values of μ_0 and γ were produced, only trapping that produced PF dependence across the entire field range could be used. Although the trap percentage/depth combination was not unique, the resulting mobility values are. Therefore, for 115 meV disorder,

there are not an infinite number of linear mobility-field plots that can be created, only a single one, and this has unique values of μ_0 and γ. To test this further, simulations were run where the correlation was removed, to see if the desired result could be reproduced using just some combination of the GDM with traps. It was found that this was not possible, that correlations must be included in order to recreate the mobility of PFB whilst satisfying the three criteria (reproducing the correct μ_0 and γ for PFB, for the same value of σ, whilst also reproducing PF dependence across all fields). The results for F8BT clarify this, as it was not possible to fulfill all three criteria, whilst remaining within σ range specified by Blakesley. Although the μ_0 and γ could be reproduced for $\sigma = 100$ meV, PF dependence was not reproduced down to low field. In other words, there are clearly not a wide variety of parameter combinations that can fulfil all three criteria, and so the values that were deduced are likely to give some real insight into the nature of the disorder in these polymers.

The following section will investigate if these disorder descriptions for PFB and F8BT can also be used to quantitatively reproduce the J-V behaviour of unilayer devices.

6.3 Unilayer device modelling

Having established the various material parameters that describe the two polymers of interest, PFB and F8BT, in terms of single carrier mobility, these material parameters will now be used to reproduce the dark current in unilayer, unipolar devices created using the same polymers. Such devices represent the next logical step after single carrier behaviour, as the morphology is the simplest possible, allowing the injection barrier to be deduced with relatively little uncertainty. If successful, this will establish that the KMC code can correctly scale up from single to multiple, interacting charge behaviour, as well as containing an accurate injection algorithm. It will also go some way to validating the nature of the disorder deduced in the previous section, and continue to show consistency with the modelling performed by Blakesley *et. al.* [62]. Previous authors have had some success in reproducing injection currents, but this is usually achieved by fitting the simulation parameters to create the desired results, and is never rooted in parameters derived from single charge mobility in the manner performed here. Furthermore, there is usually a divergence between the theory and experiment, or theory and alternative modelling, across the voltage range of a factor of 2-3 or more [37, 146].

6.3.1 Charge density dependence of the mobility

An essential element of modelling high current densities, such as those seen in injection currents, is to incorporate the mechanisms that generate the dependence of the mobility on the carrier density. Although incorporated in some transport models since 1998 [147], this essential mechanism is still often neglected when describing current flow. Hence, the independent carrier assumption made by Bässler and co-workers [30, 83] is invalid for the present work [37]. Carrier density dependence arises because, at low fields where carrier densities are low, transport is dominated by deep traps which significantly impair hopping. As the carrier density increases, these traps become filled with carriers, allowing others to bypass them, significantly raising the mobility. The dominance of small numbers of traps on current flow has already been alluded to in Section 3.2.3. This mechanism has been incorporated into drift-diffusion models by means of an additional, density-dependent term in the mobility equation. Where this has been applied to the GDM, it is referred to as the extended or EGDM. This can also be applied to the CDM, leading to the ECDM.

The carrier density:site density ratio at which these effects become noticeable can be calculated from [37],

$$c_{crossover} = 0.5 \times \exp\left[-\frac{\hat{\sigma}^2}{2}\right] \tag{6.6}$$

which for $\sigma = 110$ meV at 295 K equals a site density $\approx 10^{-5}$ or a charge density of $\approx 10^{22}$ m^{-3} for $a = 1$ nm, as used here.

This 'crossover density' was confirmed experimentally in PPV by Tanase *et. al.* [132]. In PPV and polyfluorene based polymers, such as PFB and F8BT, the forward bias carrier density is typically 10^{-4} to 10^{-5} per site, except in a thin region near the anode interface, sometimes referred to as the charge accumulation layer [36]. This layer has a typical thickness of 10-20 nm [143], at which length scale filamentary behaviour may also become significant [37]. In PVs under normal operation, i.e. between SC and OC conditions, the carrier density is of the order of 10^{22} m^{-3} [53, 45, 55], placing them approximately at the crossover density itself, depending on the bias and the position in the device. This explains why the effects of density dependence are often neglected for PV models, perhaps assumed to be an unnecessary complication, and only necessary for modelling OLEDs and FETs. However, clearly this is not necessarily true, explaining why the importance of taking carrier density dependent mobility into account in these lower density devices has been emphasised in more recent years [36].

The seminal work of Pasveer *et. al.* [134] used the EGDM to successfully model PPV, work that was continued by Bouhassoune *et. al.* [36], who compared the EGDM with the ECDM for the same set of data, and found that good fits could be obtained with both, although the EGDM fit was for a more realistic lattice spacing a. Van der Holst *et. al.* [37] extended this work still further to three dimensions, using a Master Equation approach that included injection barrier lowering due to image potential, and used a Miller-Abrahams description of charge hopping (as has been almost ubiquitous in this type of device model, with a few notable exceptions, e.g. [58, 77, 60]). In that work, devices of 75 and 150 meV disorder and 22 and 103 nm length were modelled, although it is not clear exactly what the goodness of fit was. Furthermore, no comparison with experiment was carried out. None of these three authors concluded that site correlations were necessary to accurately model device behaviour. However, the work by Blakesley

et. al. [62] questioned this. Blakesley implemented both the Pasveer and Fishchuk [148] descriptions of carrier density dependence, and found fits to PFB and F8BT devices with both, although it was found necessary to replace Pasveer's description of the field dependence of the mobility with a PF dependence. The parameters of Blakesley's fits suggested charge correlations do exist [62].

Carrier concentration dependence should be an innate feature of the KMC description, and does not require an explicit implementation. This is because the full description of site energies is already included, and so charge trapping and the bypassing of filled traps by subsequent charges is innate in this type of device modelling. Zhou *et. al.* [149] confirmed this for a Monte Carlo model by directly measuring charge mobility as a function of the density of charges in a device. Here, density dependent mobility should be confirmed by a successful progression from single charge behaviour to full J-V simulations, using the same material disorder description.

In the work that follows, the disorder descriptions obtained for PFB and F8BT in the previous section have been applied to the modelling of unilayer, unipolar devices. Results from a PFB hole-only device (HOD) and an F8BT electron-only device (EOD) have been compared to experiment, and the injection barrier ϕ_B varied to see if a good fit could be achieved without changing the disorder parameters.

6.3.2 Results

PFB

Figure 6.12 shows the results for a 103 nm PFB HOD at 295 K. Four sets of material parameters have been modelled. The first three are based on the bimodal disorder distribution, with $\sigma = 115$ meV, $\xi_c = 2$, with with trap combinations (T_0, φ) of 0.1%,1600K; 0.3%, 1225K and 0.9%, 1050K. As can be seen from Figure 6.12, all three fit the experimental results excellently for an injection barrier of $\phi_B = 0.31$ eV. However, in order to attain this fit, the hopping rate prefactor ν, used in Section 6.2, had to be raised by one order of magnitude.

The fourth energetic distribution modelled is trap-only energetic landscape, with $T_0 =$

450 K. Here, an excellent fit can be found when $\phi_B = 0.47$ eV. In order to attain this fit, the hopping rate prefactor ν had to be raised by almost three orders of magnitude.

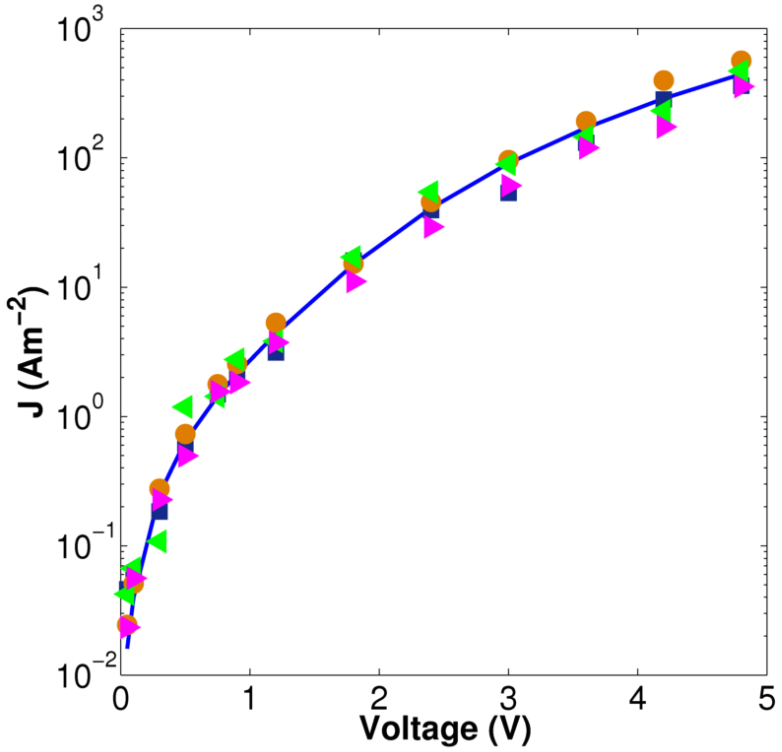

Figure 6.12: Experiment (solid line) and KMC modelling results for a unilayer PFB HOD. Datasets are for $\sigma = 115$ meV, $\xi_c = 2$, $\phi_B = 0.31$ eV, with trap combinations (T_0, φ) of 0.1% ,1600 K (◀); 0.3%, 1225 K (■) and 0.9%, 1050 K (▶). Also shown is result for a trap-only energetic landscape, with $T_0 = 450$ K, $\phi_B = 0.47$ eV (●).

F8BT

Figure 6.13 shows the results for a 107 nm F8BT unilayer, electron-only device (EOD) at 297 K. Again, the material parameters are those deduced in Section 6.2. The fit is for $\sigma = 160$ meV, $\xi_c = 2$, with with trap combinations (T_0, φ) of 0.3%, 1100 K, which was achieved for $\phi_B = 0.50$ eV. In order to attain this fit, the hopping rate prefactor ν, used in Section 6.2, had to be raised by almost three orders of magnitude.

A fit was also attempted for the equivalent trap-only distribution with $T_0 = 560$ K.

However, no injection barrier could be found that would produce a fit.

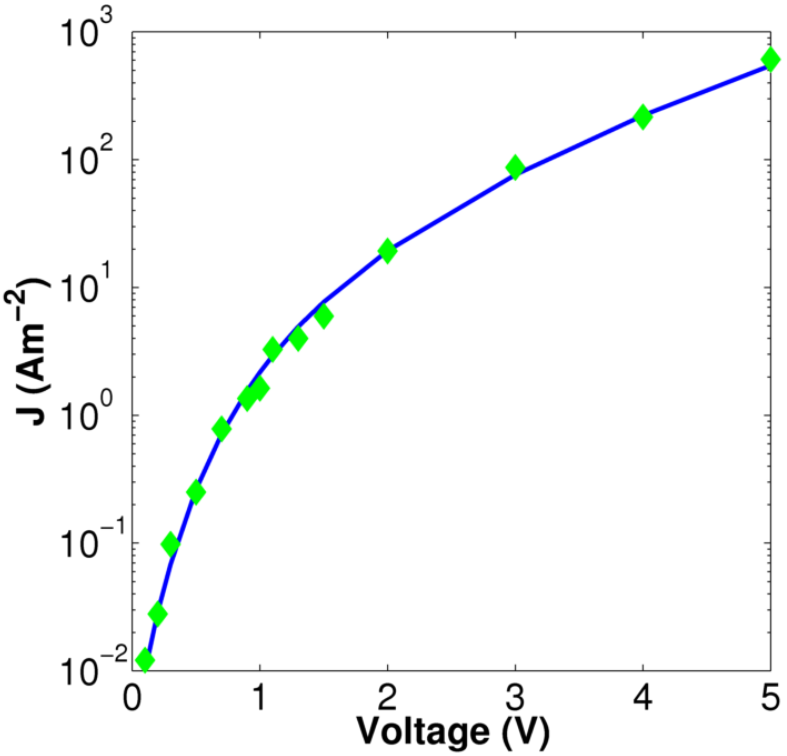

Figure 6.13: Experiment (solid line) and KMC modelling (♦) results for a unilayer F8BT EOD.

6.3.3 Discussion

The above results demonstrate mixed success with applying the disorder derived for individual charges to full current modelling in unilayer devices. A good fit can be obtained for the various disorder descriptions deduced in Section 6.2 for both devices. However, in order to achieve this, relatively high injection barriers between 0.31 and 0.50 eV had to be used. The result of this was that the hopping rate prefactor, ν, had to be increased to compensate.

Turning to the injection barriers first, these values are higher than those implemented in the drift-diffusion model of Blakesley *et. al.* [62], where Ohmic barriers and space-charge limited (SCL) behaviour was assumed. However, later work by the same author [144] has

suggested that injection barriers may commonly exist in metal-organic interfaces that are normally assumed to be Ohmic, and other modelling work has reached the same conclusion [150]. This may account for the necessity of including injection barriers in the KMC model, especially as it includes an explicit hopping description between discrete energy levels, which is not included in drift-diffusion modelling. It is therefore felt that the injection barriers deduced are not unreasonable, even if they are not consistent with the modelling of Blakesley.

The raising of the mobility prefactor, ν, means, strictly speaking, that the same mobility has not been used in the present set of simulations as was used in the single particle simulations. However, ν merely scales the mobility μ_0, it does nothing to the field dependence value, γ, which was reproduced meticulously by varying the material disorder. Therefore, it cannot account for the reproduction of the voltage dependence of the current, only the overall magnitude. Further modelling revealed that a fit for the devices cannot be achieved for any other combination of ϕ_B, ν and disorder description. Therefore, it is felt that the disorder description attained in Section 6.2 is indeed accurate, and that fitting to a unilayer device is a non-trivial result. The likely explanation in the discrepancy in ν values is an interfacial effect, not accounted for in the KMC model, perhaps creating extra resistance at the point of injection. A further test of the disorder description deduced in Section 6.2 comes in the following section, where it will be applied to a bilayer PV device, consisting of both polymers.

6.4 Photovoltaic device modelling

Having successfully identified both the nature of the energetic disorder necessary to model PFB and F8BT in terms of single particle mobility in Section 6.2; and the injection barrier required to quantitatively reproduce unilayer, unipolar behaviour in Section 6.3; full photovoltaic device modelling can now be attempted. The photovoltaic devices being modelled use the same polymers as the rest of the work in this chapter, and the results come from the same set of experiments. Therefore, if the KMC modelling methodology is accurate, and if the correct device parameters have been identified in the preceding sections, then quantitatively accurate photovoltaic modelling should be possible without adjustment of the parameters deduced thus far. In order to complete the work, quantitatively accurate energy transport will now need to be included in the device modelling. Specifically, the correct absorbed photon flux and distribution will need to be calculated, and the behaviour of the resultant excitons modelled accurately as well. As with all the work contained herein, these cannot simply be deduced by fitting to the experimental results, instead they will be deduced through detailed optical modelling.

The first preliminary stage is to calculate the correct absorbed photon flux, η_A and the optical absorption distribution (i.e. the distribution of exciton creation) within the device, Q(x). These concepts and their implementation in the device model were outlined in Section 2.1.2. Calculation of these values involves the creation of a full optical model of the photovoltaic device geometry and materials. This will calculate the internal optical field, |E|, from which η_A and Q(x) can be found. Implementing the exciton distribution, Q(x), within the KMC model is achieved by first loading it as a vector, normalised to its peak value. When an exciton creation event is added to the queue, the exciton subroutine first chooses a random location within the device, and then finds Q at this location. This number of then compared to a random number between 0 and 1, R. If $(R < Q)$, the location is accepted and chosen as the destination site for the next exciton. If not, the process is repeated with new sites until one is accepted. Subsequent exciton diffusion follows the description given in Section 2.3.3. It has been assumed that the material disorder encountered by excitons is identical to that deduced for charges, an approach which avoids introducing further unknowns into the KMC model, and maintains a consistent material description. Therefore the exciton diffusion length will be set from the combination of the parameters taken from

Athanasopolus *et. al.* [28] (see Section 2.3.3) and the disorder description derived in the preceding sections, without adjustment. This will provide a further test of the disorder description, alongside that of accurately reproducing the current.

The single remaining adjustable parameter in the KMC code is the charge recombination rate, k_r. As explained in Section 2.6, this is always modelled as a fixed rate constant due to the complexity and uncertainty over this process. As there is no way to derive this from the KMC model, it is a true fitting parameter, which can be calibrated until a good fit with experiment is achieved. However, it is still constrained to being of the same order as that used in other work. Furthermore it cannot, on its own, create a good fit to experiment unless all the other processes are modelled accurately. Preliminary modelling (not shown) showed that the ratio $k_r : \mu$ must be fixed in order to create the correct voltage dependency, and μ has been fixed by the previous sections of this chapter. The value of k_r must fulfil three criteria: consistency with previous work, correct voltage dependence of current and correct magnitude of current. Therefore it cannot be seen simply as an arbitrary fitting parameter. No other parameters will be adjusted, as each one finds its origin in previous work, and as such the result is self-consistent.

6.4.1 The need for full optical modelling

It has been frequently shown that full and accurate optical modelling is essential to understanding and predicting organic PV characteristics [151, 119, 152, 4]. Optical modelling reveals, for instance, why device absorption does not always increase linearly with active layer thickness, and can also be used to calculate the optimum thickness and device structure for any combination of device layers. This takes into account precisely how much light will be absorbed in any given device, and precisely where the light will be absorbed, allowing alignment of absorption peaks with heterojunctions.

Williams *et. al.* [55] combined finite element optical and electrical modelling to predict the efficiencies of PV devices with two-dimensional morphologies, and emphasised the difference in predicted efficiency when using a full optical model in comparison to a simple Lambertian optical profile. Although simpler optical calculations may be sufficient when making qualitative analysis of PV devices [32], full optical modelling is an essential step in the present work in order to create quantitative agreement with experiment. This

will also reduce the number of free parameters in the model, a core philosophy of the present chapter, deducing these parameters through rigorous investigation, rather than simply fitting them to results.

6.4.2 Details of the optical model

The essential physical principles behind accurate optical modelling will be laid out below, followed by the results for the bilayer device used in experiment. The definitions and derivations given here are based on [153] and [151].

Beginning with the complex index of refraction,

$$\tilde{n} = \eta + i\kappa \tag{6.7}$$

where the real part, η, is the ratio of the wave velocity in a vacuum (c) to that in the medium of interest (ν), which is dependent on the permittivity and permeability of the medium with respect to a vacuum,

$$\eta = \frac{c}{\nu} = \sqrt{\frac{\epsilon\mu}{\epsilon_0\mu_0}} = \sqrt{\epsilon_R\mu_R} \tag{6.8}$$

and the imaginary part, κ, also known as the extinction coefficient, accounts for absorption in the medium. The optical electric field of a light source, $\underline{\mathrm{E}}$, is exponentially attenuated by the medium. If I_0 is the irradiance of the light source at normal incidence on a medium ($\mathrm{I} = |\mathrm{E}|^2$), the irradiance of the light after passing through a distance x is,

$$I = I_0 e^{-\alpha x} \tag{6.9}$$

Where α is the wavelength-dependent attenuation coefficient, which is also defined as,

$$\alpha = \frac{4\pi\kappa}{\lambda} \tag{6.10}$$

It is clear that α, and hence κ, can easily be deduced from experiment by measuring I before and after light has passed through the medium of interest. In spectroscopy, the absorptance of a specific thickness x of a medium is defined as,

$$A_\lambda = -\ln\left(\frac{I}{I_0}\right) = \alpha x \tag{6.11}$$

therefore κ can alternatively be defined as,

$$\kappa = \frac{A_\lambda \lambda}{4\pi x} \tag{6.12}$$

Although the absorptance of a single layer can be calculated simply from the incident and transmitted optical power density, when there are multiple layers, there will be a refractive index change at each interface, and some light will be transmitted, and some reflected. Furthermore, the back electrode will also absorb and reflect some light. The reflectance of the complete optical stack can be calculated using a simple transfer matrix method [153].

However, in order to find Q(x), the full optical interference pattern within the optical stack needs to be calculated, a task which requires full optical modelling. This works by first calculating the optical electric field within the stack, and hence the absorption distribution Q(x). It can be shown that Q(x), defined as the time average of the energy dissipated per second at a depth x within the device, is given by [151, 154],

$$Q(x) = \frac{1}{2} c\epsilon_0 \alpha \eta E^2 \tag{6.13}$$

The optical model can also calculate η_A, which may be compared to the value calculated using the Transfer Matrix method as means of validating the method. η_A and Q(x) can then be input into the KMC model.

All the experimental work was performed with a monochromatic light source of $\lambda = 460$ nm. The necessary optical constants at this wavelength for the different layers of the optical stack have been taken from work published on the same materials, with the exception of the extinction coefficient of F8BT. This value was calculated directly from absorption data provided on the same experimental system modelled throughout this chapter, and was found to be $\kappa = 0.64$ using eq. 6.12. A summary of the optical constants used, and their sources, is given in Table 6.1.

	Thickness	η	κ	Reference
Glass		1.5	0	[155]
ITO	120 nm	1.9	3.8×10^{-3}	[151, 155], JB
PEDOT	120 nm	1.5	2.5×10^{-2}	[151, 155]
PFB	45 nm	1.8	1.2×10^{-2}	[156]
F8BT	90 nm	1.7	6.4×10^{-1}	[156], JB
Al	150 nm	0.6	5.2	[156]

Table 6.1: Optical constants for the layers in the bilayer PV device. 'JB' indicates specific data from Dr. James Blakesley

The optical modelling was based on the work of JHT Williams [55, 154], and was performed by Simon O'Kane using Comsol finite element software. As this work was not performed by the author, computational details will not be given, but can be found in the publications of JHT Williams. Throughout this work, it has been assumed that, in experiment, the thickness of the aluminium electrode is much greater than the skin depth of the light (defined as $x = \frac{1}{\alpha}$) , and as such there is no light transmittance through the device as a whole. Concomitantly, the total light absorptance of the device is 1-R, where R is the overall reflectance [151]. In the model, this is achieved simply by increasing the thickness of the aluminium layer until the electric field within it decays effectively to zero (to six decimal places), which was achieved when the thickness was in excess of 150 nm.

Bilayer optical results

The geometry of the optical stack used in the bilayer device is illustrated in Figure 6.14. The optical electric field for this device, |E|(x), normalised to its peak value, is shown in Figure 6.15. From this, the absorption distribution, Q(x), can be calculated using the

relevant values from Table 6.1, and this is shown in Figure 6.16. At 460 nm, the device absorptance, calculated by both the full optical model and the transfer matrix method, is 95.6%. Of this, 0.14% is absorbed in the PFB layer, and 87.3% is absorbed in the F8BT layer, making the total absorbed within the polymer layers to be 84.8% of the incident photon flux at 460 nm.

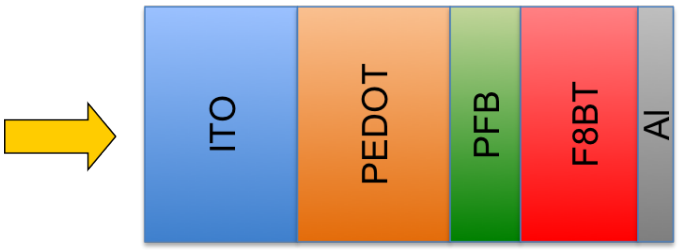

Figure 6.14: Diagrammatic optical stack for modelling of the bilayer device.

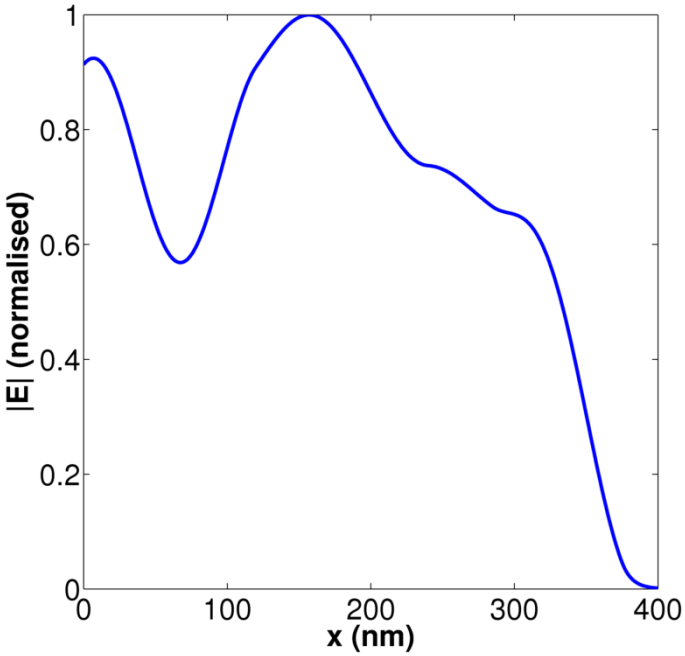

Figure 6.15: |E|(x) (normalised to its peak value) in the bilayer device.

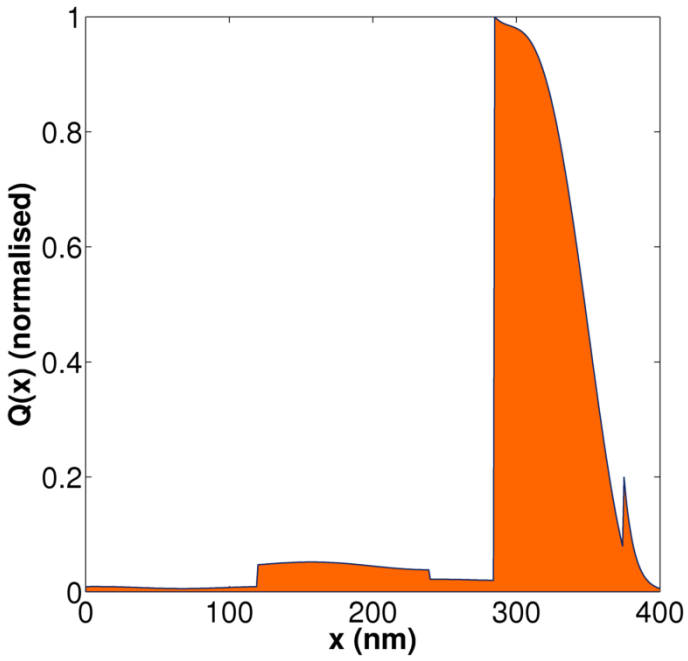

Figure 6.16: Q(x) (normalised to its peak value) in the bilayer device.

6.4.3 KMC modelling results

Figure 6.17 shows than excellent fit to both the experimental EQE and the current density J can be achieved for a recombination rate of $k_r = 1 \times 10^7$ s^{-1}. This is identical to the value used by Groves *et. al.* [89] for modelling geminate recombination in the same polymer combination, where it was also noted that this value is similar to the 40 ns lifetime measured for PFB:F8BT blends [157]. The modelling was not applied for voltages beyond the open-circuit voltage of 1.3 V, as the reasons for obtaining a forward bias current in a bilayer device are undefined. No other parameters were adjusted from those that were derived in the preceding sections.

6.4.4 Discussion

The fact that the experimental results for the bilayer device could be reproduced without adjustment of the material disorder parameters lends further credence to their accuracy.

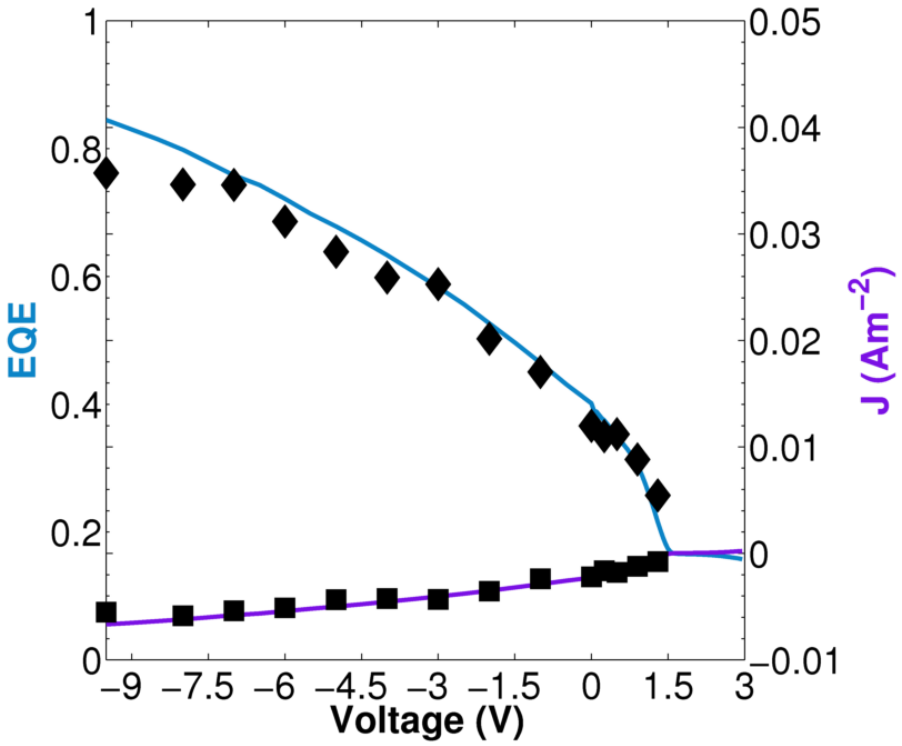

Figure 6.17: Experimental (solid lines) and KMC simulated EQE (♦) and J (■) for a bilayer device.

As discussed earlier, these disorder values influence not only the charge mobility, but the exciton diffusion length as well. Reproduction of both the EQE and current density of the device shows that, not only is the field dependency of the current being accurately reproduced, but the actual magnitude is correct as well. This goes a long way to validating each part of the method applied throughout this chapter. In a bilayer device, it is unclear as to why there should be a current at forward bias, as both of the layers are unipolar. Possibilities include imperfections in the device structure or impurities in the polymers. As the origin of this forward bias current is unknown, it has not been modelled. Therefore, this section has been unable to test the injection barriers deduced in Section 6.3.

6.5 Summary and conclusions

In Section 6.2, the GDM, CDM and trapping models were evaluated in terms of their effect on the mobility of individual charges. It was identified that in order to reproduce a Poole-Frenkel mobility-field relationship across a field range of $F^{0.5} = 1000 : 10000$ $(\mathrm{V/m})^{0.5}$ (which is typical of organic polymer experiments and simulations), that it is necessary to model the energetic disorder either as a bimodal energetic landscape, consisting of both correlated disorder and a minority trapping distribution; or using an exponential trapping distribution alone. Both of these forms of disorder have a solid experimental and theoretical basis. In terms of the specific mobility of charges in PFB and F8BT, disorder distributions were identified that could reproduce the values of μ_0 and γ, as deduced by Blakesley *et. al.* using drift-diffusion modelling [62]. For both polymers, the mobility values could be reproduced for the same level of energetic disorder, σ, as used by Blakesley (within the margin of error stated in that work), although a better fit could be found by using a higher, but not unreasonable, value of σ for F8BT. The two polymers were found to have the same range of energetic correlation, and very similar trapping distributions. In both cases, it was possible to reproduce the mobility values whilst also reproducing a PF relationship across the entire field range examined. This work goes some way to quantifying different disorder descriptions used in modelling charge transport, which is currently a topic with no real consensus in the literature. It also shows a good consistency between the modelling performed here, and independent drift-diffusion modelling.

This disorder description was applied to unilayer devices in Section 6.3, and PV devices in Section 6.4 with great success. However, reproduction of accurate injection behaviour in Section 6.3 required modification of the hopping rate constant used in Section 6.2. This is not felt to be a terminal flaw in the methodology, but simply attributable to an uncharacterised interfacial effect, which affects the injection description used. Furthermore, modification of the hop rate constant merely scales the resulting current. The fact that the correct voltage dependence of the current could still be reproduced is seen as a non-trivial achievement, and goes some way to validating both the disorder description, and the KMC model. The excellent reproduction of bilayer PV behaviour in Section 6.4 provides further validation of the findings of this chapter, and also of the necessity of full optical modelling.

Aside from providing validation of the methodology used in this thesis, justification of using a KMC model for these data lies in the advantages it has over drift-diffusion modelling. KMC modelling inevitably provides insight into the nanoscopic descriptions of charge and energy transport in nanoscale landscapes, as this is the scale on which it operates. For instance, in the drift-diffusion model, a PF relationship was assumed [62], whereas in the KMC model, disorder descriptions that produce this relationship in the first place must first be found. Therefore, the KMC model can give some insight as to the nanoscopic origin of the PF relationship. It is also a means of testing various different descriptions of the disorder on the scale of the conjugated segments.

Perhaps most importantly, having now validated the approach used here, it can then be applies to scenarios that the KMC is uniquely able to deal with. The method used in this chapter is highly applicable to complex, three-dimensional morphologies, which drift-diffusion modelling is unable to accurately represent. Just as the work in Chapter 5 showed the unique capabilities of the KMC to assess the role of morphology in determining device efficiency, and the work in Chapters 4 and 5 revealed unique insight into geminate dissociation dynamics, so the KMC, with a working quantitative methodology, is now capable of providing real insight into other experimental results. The fact that charge injection and high current densities have been successfully simulated suggests it is also capable of OLED simulation. A consistent fit to the Blakesley data suggests that the approach used here is transferable, as well as the actual parameters deduced.

Chapter 7

Further work

The work contained within this thesis naturally lends itself to further avenues of exploration.

Chapter 4 showed that the First Reaction Method is applicable to OPV simulations, as it accurately models geminate separation dynamics within the range of field and disorder values encountered in devices. However, in Chapter 6, this approximation was not used, as its validity under forward bias, which involves injection and higher current densities than are encountered in photovoltaics, has not been confirmed. Therefore, a natural extension of the work on the FRM would be to quantify its validity as a function of current density. It could then be established if, and under which parameters, the FRM approximation might still be used in order to reduce the computing resources demanded by KMC simulations of non-OPV devices.

Chapter 6 concerned quantitative modelling of PFB:F8BT devices. However, due to time constraints, all of the modelling was performed at room temperature, and only one thickness of each device was examined. Before the methodology contained within that chapter can be confirmed to be fully accurate and applicable to other devices, it must be able to consistently reproduce the temperature and thickness dependence of the mobility and current seen in experimental devices. Although investigating thickness dependence is trivial, temperature dependence is far more complicated, as the temperature can affect the morphology, as well the reorganisation energy and electronic coupling for charge

transfer, none of which are calculable using the KMC model. However, investigations of this nature might still provide a useful extension of this work. The obvious future application of this work, should its general validity be confirmed, is to model devices with morphological variations, an area of investigation that the KMC model is uniquely able to deal with.

References

[1] David JC MacKay. *Sustainable Energy - Without the Hot Air*. UIT, Cambridge. (Provided in complete form on www.withoutthehotair.com), 2009.

[2] Mary .D. Archer and Robert. Hill, editors. *Clean electricity from photovoltaics*. Imperial College Press, London, 2001.

[3] J. Nelson. *The Physics of Solar Cells*. Imperial College Press, London, 2003.

[4] B. Kippelen and J.L. Brédas. Organic photovoltaics. *Energy Environ. Sci.*, 2(3):251–261, 2009.

[5] J. Hirokane, T. Saga, T. Muramatsu, and I. Shirakawa. History of contribution of photovoltaic cells to telecommunications. In *Telecommunications Conference (HISTELCON), 2010 Second IEEE Region 8 Conference on the History of*, pages 1 –6, nov. 2010.

[6] CW Tang. Two-layer organic photovoltaic cell. *Applied Physics Letters*, 48(2):183–185, 1986.

[7] CW Tang and SA VanSlyke. Organic electroluminescent diodes. *Applied Physics Letters*, 51(12):913–915, 1987.

[8] V. Shrotriya. Organic photovoltaics: Polymer power. *Nature Photonics*, 3(8):447–449, 2009.

[9] M.A. Green, K. Emery, Y. Hishikawa, and W. Warta. Solar cell efficiency tables (version 37). *Progress in Photovoltaics: Research and Applications*, 19(1):84–92, 2011.

[10] MA; Watt ME Wenham, SR; Green and R Corkish. *Applied Photovoltaics*. Earthscan, London, 2007.

[11] M.A. Green, K. Emery, D.L. King, and S. Igari. Solar cell efficiency tables (version 15). *Progress in photovoltaics: research and applications*, 8(1):187–195, 2000.

[12] M.A. Green, K. Emery, D.L. King, Y. Hishikawa, and W. Warta. Solar cell efficiency tables (version 28). *Progress in Photovoltaics: Research and Applications*, 14(5):455–461, 2006.

[13] NREL. American society for testing and materials (astm) terrestrial reference spectra for photovoltaic performance evaluation (http://rredc.nrel.gov/solar/spectra/am1.5/).

[14] Pete Watkins. *Modelling of Charge and Exciton Dynamics in Organic Solar Cells*. PhD thesis, University of Bath, 2005.

[15] G.L. Araújo and A. Martí. Absolute limiting efficiencies for photovoltaic energy conversion. *Solar Energy Materials and Solar Cells*, 33(2):213–240, 1994.

[16] P. Atkins and J. de Paula. *Atkins' Physical Chemistry, 8th Edition*. Oxford University Press New York, 2006.

[17] M. Jaiswal and R. Menon. Polymer electronic materials: a review of charge transport. *Polymer International*, 55(12):1371–1384, 2006.

[18] S. Athanasopoulos, E. Hennebicq, D. Beljonne, and A.B. Walker. Trap Limited Exciton Transport in Conjugated Polymers. *The Journal of Physical Chemistry C*, 112(30):11532–11538, 2008.

[19] AB Walker, A. Kambili, SJ Martin, et al. Electrical transport modelling in organic electroluminescent devices. *Journal of Physics-Condensed Matter*, 14(42):9825–9876, 2002.

[20] K.(Klaus) Mullen and U. Scherf. *Organic light emitting devices*. WILEY-VCH Verl. GmbH & Co. KGaA Weinheim, 2006.

[21] I. N. Hulea, H. B. Brom, A. J. Houtepen, D. Vanmaekelbergh, J. J. Kelly, and E. A. Meulenkamp. Wide energy-window view on the density of states and hole mobility in poly(*p*-phenylene vinylene). *Phys. Rev. Lett.*, 93(16):166601, 2004.

[22] M. Berggren, P. Bergman, J. Fagerström, O. Inganäs, M. Andersson, H. Weman, M. Granström, S. Stafström, O. Wennerström, and T. Hjertberg. Controlling inter-chain and intra-chain excitations of a poly (thiophene) derivative in thin films. *Chemical Physics Letters*, 304(1-2):84–90, 1999.

[23] D. Micha, I. Burghardt, and MyiLibrary. *Quantum dynamics of complex molecular systems*. Springer, 2007.

[24] N.J. Turro. *Molecular photochemistry*. WA Benjamin, 1965.

[25] James Guillet. *Polymer photophysics and photochemistry : an introduction to the study of photo processes in macromolecules.* Cambridge University Press, Cambridge, 1985. ISBN: 0521235065.

[26] J.F. Rabek. *Mechanisms of photophysical processes and photochemical reactions in polymers: Theory and Applications*, volume 285. Wiley, 1987.

[27] JL Bredas, D. Beljonne, V. Coropceanu, and J. Cornil. Charge-transfer and energy-transfer processes in pi-conjugated oligomers and polymers: a molecular picture. *Chem Rev*, 104(11):4971–5004, 2004.

[28] S. Athanasopoulos, E.V. Emelianova, A.B. Walker, and D. Beljonne. Exciton diffusion in energetically disordered organic materials. *Physical Review B*, 80(19):195209, 2009.

[29] A. Miller and E. Abrahams. Impurity conduction at low concentrations. *Physical Review*, 120(3):745–755, 1960.

[30] H. Bassler. Charge transport in disordered organic photoconductors: A Monte Carlo simulation study. *Physica status solidi. B. Basic research*, 175(1):15–56, 1993.

[31] S.C.J. Meskers, J. Hubner, M. Oestreich, and H. Bassler. Dispersive relaxation dynamics of photoexcitations in a polyfluorene film involving energy transfer: experiment and Monte Carlo simulations. *J. Phys. Chem. B*, 105(38):9139–9149, 2001.

[32] P.K. Watkins, A.B. Walker, and G.L.B. Verschoor. Dynamical Monte Carlo modelling of organic solar cells: The dependence of internal quantum efficiency on morphology. *Nano Lett*, 5(9):1814–1818, 2005.

[33] R.A. Marcus. Electron transfer reactions in chemistry. Theory and experiment. *Reviews of Modern Physics*, 65(3):599–610, 1993.

[34] R.A. Marcus. Theory of Electron Transfer Reactions. Technical report, California Institute of Technology, Pasadena, 1994.

[35] M. Scheidler, U. Lemmer, R. Kersting, S. Karg, W. Riess, B. Cleve, RF Mahrt, H. Kurz, H. Bässler, EO Göbel, et al. Monte Carlo study of picosecond exciton relaxation and dissociation in poly (phenylenevinylene). *Physical Review B*, 54(8):5536–5544, 1996.

[36] M. Bouhassoune, S.L.M. Mensfoort, PA Bobbert, and R. Coehoorn. Carrier-density and field-dependent charge-carrier mobility in organic semiconductors with correlated Gaussian disorder. *Organic Electronics*, 10(3):437–445, 2009.

[37] JJM van der Holst, MA Uijttewaal, B. Ramachandhran, R. Coehoorn, PA Bobbert, GA de Wijs, and RA de Groot. Modeling and analysis of the three-dimensional current density in sandwich-type single-carrier devices of disordered organic semiconductors. *Physical Review B*, 79(8):85203, 2009.

[38] V. Coropceanu, J. Cornil, D.A. da Silva Filho, Y. Olivier, R. Silbey, and J.L. Bredas. Charge transport in organic semiconductors. *Chem. Rev*, 107(4):926–952, 2007.

[39] S. Athanasopoulos, J. Kirkpatrick, D. Martinez, JM Frost, CM Foden, AB Walker, and J. Nelson. Predictive study of charge transport in disordered semiconducting polymers. *Nano letters*, 7(6):1785, 2007.

[40] G. Grampp. The Marcus inverted region from theory to experiment. *Angewandte Chemie International Edition in English*, 32(5):691–693, 1993.

[41] C. Groves, RA Marsh, and NC Greenham. Monte Carlo modeling of geminate recombination in polymer-polymer photovoltaic devices. *The Journal of Chemical Physics*, 129:114903, 2008.

[42] S.M. Sze. *Semiconductor devices: physics and technology*. John Wiley & Sons, 2001.

[43] R.W. Hockney and J.W. Eastwood. *Computer simulation using particles*. Institute of Physics, 1992.

[44] VD Mihailetchi, LJA Koster, and PWM Blom. Effect of metal electrodes on the performance of polymer: fullerene bulk heterojunction solar cells. *Applied Physics Letters*, 85:970, 2004.

[45] LJA Koster, ECP Smits, VD Mihailetchi, and PWM Blom. Device model for the operation of polymer/fullerene bulk heterojunction solar cells. *Physical Review B*, 72(8):85205, 2005.

[46] P. Piromreun, H.S. Oh, Y. Shen, G.G. Malliaras, J.C. Scott, and P.J. Brock. Role of CsF on electron injection into a conjugated polymer. *Applied Physics Letters*, 77:2403, 2000.

[47] EM Conwell and MW Wu. Contact injection into polymer light-emitting diodes. *Applied Physics Letters*, 70:1867, 1997.

[48] A.C. Morteani, P. Sreearunothai, L.M. Herz, R.H. Friend, and C. Silva. Exciton regeneration at polymeric semiconductor heterojunctions. *Physical review letters*, 92(24):247402, 2004.

[49] C.R. McNeill, A. Abrusci, J. Zaumseil, R. Wilson, M.J. McKiernan, J.H. Burroughes, J.J.M. Halls, N.C. Greenham, and R.H. Friend. Dual electron donor/electron acceptor character of a conjugated polymer in efficient photovoltaic diodes. *Applied Physics Letters*, 90:193506, 2007.

[50] E. Moons. Conjugated polymer blends: linking film morphology to performance of light emitting diodes and photodiodes. *Journal of Physics: Condensed Matter*, 14:12235, 2002.

[51] J. Nelson, J. Kirkpatrick, and P. Ravirajan. Factors limiting the efficiency of molecular photovoltaic devices. *Physical Review B*, 69(3):035337, 2004.

[52] H.J. Snaith, H. Kenrick, M. Chiesa, and R.H. Friend. Morphological and electronic consequences of modifications to the polymer anode pedot:pss. *Polymer*, 46(8):2573–2578, 2005.

[53] JA Barker, CM Ramsdale, and NC Greenham. Modeling the current-voltage characteristics of bilayer polymer photovoltaic devices. *Physical Review B*, 67(7):75205, 2003.

[54] CM Martin, VM Burlakov, HE Assender, and DAR Barkhouse. A numerical model for explaining the role of the interface morphology in composite solar cells. *Journal of Applied Physics*, 102:104506, 2007.

[55] J. Williams and A.B. Walker. Two-dimensional simulations of bulk heterojunction solar cell characteristics. *Nanotechnology*, 19(42):424011, 2008.

[56] LJA Koster. Charge carrier mobility in disordered organic blends for photovoltaics. *Physical Review B*, 81(20):205318, 2010.

[57] ZG Yu, DL Smith, A. Saxena, RL Martin, and AR Bishop. Molecular geometry fluctuation model for the mobility of conjugated polymers. *Physical review letters*, 84(4):721–724, 2000.

[58] J. Nelson, J.J. Kwiatkowski, J. Kirkpatrick, and J.M. Frost. Modeling Charge Transport in Organic Photovoltaic Materials. *Accounts of chemical research*, pages 2373–2380, 2009.

[59] D.T. Gillespie. A general method for numerically simulating the stochastic time evolution of coupled chemical reactions. *Journal of computational physics*, 22(4):403–434, 1976.

[60] C. Groves, LJA Koster, and NC Greenham. The effect of morphology upon mobility: Implications for bulk heterojunction solar cells with nonuniform blend morphology. *Journal of Applied Physics*, 105:094510, 2009.

[61] A.B. Walker. Multiscale Modeling of Charge and Energy Transport in Organic Light-Emitting Diodes and Photovoltaics. *Proceedings of the IEEE*, 97(9):1587–1596, 2009.

[62] J. C. Blakesley, H. S. Clubb, and N. C. Greenham. Temperature-dependent electron and hole transport in disordered semiconducting polymers: Analysis of energetic disorder. *Phys. Rev. B*, 81(4):045210, Jan 2010.

[63] S.S. Sun, C. Zhang, A. Ledbetter, S. Choi, K. Seo, C.E. Bonner Jr, M. Drees, and N.S. Sariciftci. Photovoltaic enhancement of organic solar cells by a bridged donor-acceptor block copolymer approach. *Applied Physics Letters*, 90:043117, 2007.

[64] C.R. McNeill, S. Westenhoff, C. Groves, R.H. Friend, and N.C. Greenham. Influence of nanoscale phase separation on the charge generation dynamics and photovoltaic performance of conjugated polymer blends: Balancing charge generation and separation. *J. Phys. Chem. C*, 111:1915319160, 2007.

[65] B.C. Thompson and J.M.J. Frechet. Polymer-fullerene composite solar cells. *Angewandte Chemie International Edition*, 47(1):58–77, 2008.

[66] JJ Halls, CA Walsh, NC Greenham, EA Marseglia, RH Friend, SC Moratti, and AB Holmes. Efficient photodiodes from interpenetrating polymer networks. *Nature*, 376(6540):498–500, 1995.

[67] G. Yu, J. Gao, JC Hummelen, F. Wudl, and AJ Heeger. Polymer photovoltaic cells: enhanced efficiencies via a network of internal donor-acceptor heterojunctions. *Science*, 270(5243):1789, 1995.

[68] CD Adams, DJ Srolovitz, and M. Atzmon. Monte Carlo simulation of phase separation during thin-film codeposition. *Journal of Applied Physics*, 74(3):1707–1715, 1993.

[69] P. Peumans, S. Uchida, and S.R. Forrest. Efficient bulk heterojunction photovoltaic cells using small-molecular-weight organic thin films. *Nature*, 425(6954):158–162, 2003.

[70] Kyozi Kawasaki. *Phase Transitions and Critical Phenomena, Volume 2*. Academic Press, 1972.

[71] J. C.C. Nitsche. *Vorlesungen über Minimalflächen*. Springer-Verlag, Berlin, 1975.

[72] F.C. Chen, Y.K. Lin, and C.J. Ko. Submicron-scale manipulation of phase separation in organic solar cells. *Applied Physics Letters*, 92:023307, 2008.

[73] M.S. Kim, J.S. Kim, J.C. Cho, M. Shtein, L.J. Guo, and J. Kim. Flexible conjugated polymer photovoltaic cells with controlled heterojunctions fabricated using nanoimprint lithography. *Applied Physics Letters*, 90:123113, 2007.

[74] Y. Kang, N.G. Park, and D. Kim. Hybrid solar cells with vertically aligned CdTe nanorods and a conjugated polymer. *Applied Physics Letters*, 86:113101, 2005.

[75] G.K. Mor, K. Shankar, M. Paulose, O.K. Varghese, and C.A. Grimes. High efficiency double heterojunction polymer photovoltaic cells using highly ordered TiO nanotube arrays. *Applied Physics Letters*, 91:152111, 2007.

[76] C.J. Brabec, N.S. Sariciftci, J.C. Hummelen, et al. Plastic solar cells. *Advanced Functional Materials*, 11(1):15–26, 2001.

[77] RA Marsh, C. Groves, and NC Greenham. A microscopic model for the behavior of nanostructured organic photovoltaic devices. *Journal of Applied Physics*, 101:083509, 2007.

[78] F. Yang and S.R. Forrest. Photocurrent generation in nanostructured organic solar cells. *ACS Nano*, 2(5):1022–1032, 2008.

[79] L. Meng, Y. Shang, Q. Li, Y. Li, X. Zhan, Z. Shuai, R.G.E. Kimber, and A.B. Walker. Dynamic Monte Carlo simulation for highly efficient polymer blend photovoltaics. *The Journal of Physical Chemistry B*, 114:36–41, 2009.

[80] L. Meng, D. Wang, Q. Li, Y. Yi, J.L. Brédas, and Z. Shuai. An improved dynamic Monte Carlo model coupled with Poisson equation to simulate the performance of organic photovoltaic devices. *The Journal of Chemical Physics*, 134:124102, 2011.

[81] M. Casalegno, G. Raos, and R. Po. Methodological assessment of kinetic Monte Carlo simulations of organic photovoltaic devices: The treatment of electrostatic interactions. *The Journal of Chemical Physics*, 132:094705, 2010.

[82] Y.N. Gartstein and EM Conwell. High-field hopping mobility in molecular systems with spatially correlated energetic disorder. *Chemical Physics Letters*, 245(4-5):351–358, 1995.

[83] U. Wolf, VI Arkhipov, and H. Bässler. Current injection from a metal to a disordered hopping system. I. Monte Carlo simulation. *Physical Review B*, 59(11):7507–7513, 1999.

[84] APJ Jansen. Monte Carlo simulations of chemical reactions on a surface with time-dependent reaction-rate constants. *Computer physics communications*, 86(1-2):1–12, 1995.

[85] APJ Jansen. An introduction to Monte Carlo simulations of surface reactions. *Arxiv preprint cond-mat/0303028*, 2003.

[86] C. Groves and NC Greenham. Bimolecular recombination in polymer electronic devices. *Physical Review B*, 78(15):155205, 2008.

[87] C.L. Braun. Electric field assisted dissociation of charge transfer states as a mechanism of photocarrier production. *The Journal of Chemical Physics*, 80:4157, 1984.

[88] LJA Koster, VD Mihailetchi, and PWM Blom. Ultimate efficiency of polymer/fullerene bulk heterojunction solar cells. *Applied physics letters*, 88:093511, 2006.

[89] C. Groves, J.C. Blakesley, and N.C. Greenham. Effect of Charge Trapping on Geminate Recombination and Polymer Solar Cell Performance. *Nano letters*, 10:1063–1069, 2010.

[90] W. Shockley and H.J. Queisser. Detailed Balance Limit of Efficiency of p-n Junction Solar Cells. *Journal of Applied Physics*, 32:510, 1961.

[91] B. Walker, A.B. Tamayo, X.D. Dang, P. Zalar, J.H. Seo, A. Garcia, M. Tantiwiwat, and T.Q. Nguyen. Nanoscale Phase Separation and High Photovoltaic Efficiency in Solution-Processed, Small-Molecule Bulk Heterojunction Solar Cells. *Advanced Functional Materials*, 19(19):3063–3069, 2009.

[92] S.S. Sun. Polymer photovoltaic optimizations from exciton level. *Journal of Materials Science: Materials in Electronics*, 18(11):1143–1146, 2007.

[93] J.A. Thorpe. *Elementary topics in differential geometry*. Springer, 1979.

[94] Gerd Elmar Schröder. *Skeletons in the labyrinth*. PhD thesis, The Australian National University, Canberra, 2005.

[95] V. Luzzati, A. Tardieu, T. Gulik-Krzywicki, E. Rivas, and F. Reiss-Husson. Structure of the cubic phases of lipid–water systems. 1968.

[96] M. Impéror-Clerc. Thermotropic cubic mesophases. *Current Opinion in Colloid & Interface Science*, 9(6):370–376, 2005.

[97] LJ Ellison, DJ Michel, F. Barmes, and DJ Cleaver. Entropy-driven formation of the gyroid cubic phase. *Physical review letters*, 97(23):237801, 2006.

[98] F.S. Bates and G.H. Fredrickson. Block copolymers–designer soft materials. *Physics today*, 52:32–38, 1999.

[99] F.S. Bates. Network phases in block copolymer melts. *MRS bulletin*, 30:525, 2005.

[100] S.T. Hyde, M. O'Keeffe, and D.M. Proserpio. A Short History of an Elusive Yet Ubiquitous Structure in Chemistry, Materials, and Mathematics. *Angewandte Chemie International Edition*, 47(42):7996–8000, 2008.

[101] A.H. Schoen. Infinite periodic minimal surfaces without self-intersections. *Technical Note TN D-5541, NASA*, 1970.

[102] D.A. Hajduk, P.E. Harper, S.M. Gruner, C.C. Honeker, G. Kim, E.L. Thomas, and L.J. Fetters. The gyroid: a new equilibrium morphology in weakly segregated diblock copolymers. *Macromolecules*, 27(15):4063–4075, 1994.

[103] V.N. Urade, T.C. Wei, M.P. Tate, J.D. Kowalski, and H.W. Hillhouse. Nanofabrication of double-gyroid thin films. *Chem. Mater*, 19(4):768–777, 2007.

[104] CC Oey, AB Djurišić, H. Wang, KKY Man, WK Chan, MH Xie, YH Leung, A. Pandey, JM Nunzi, and PC Chui. Polymer–TiO2 solar cells: TiO2 interconnected network for improved cell performance. *Nanotechnology*, 17:706, 2006.

[105] E.J.W. Crossland, M. Nedelcu, C. Ducati, S. Ludwigs, M.A. Hillmyer, U. Steiner, and H.J. Snaith. Block Copolymer Morphologies in Dye-Sensitized Solar Cells: Probing the Photovoltaic Structure- Function Relation. *Nano Lett*, 9(8):2813–2819, 2009.

[106] E.J.W. Crossland, M. Kamperman, M. Nedelcu, C. Ducati, U. Wiesner, D.M. Smilgies, G.E.S. Toombes, M.A. Hillmyer, S. Ludwigs, U. Steiner, et al. A Bicontinuous Double Gyroid Hybrid Solar Cell. *Nano Lett*, 9(8):2807–2812, 2009.

[107] Y. Chiba, A. Islam, Y. Watanabe, R. Komiya, N. Koide, and L. Han. Dye-sensitized Solar Cells with Conversion Efficiency of 11.1%. *Japanese Journal of Applied Physics*, 45(24/28):638, 2006.

[108] Y. Zhang, K. Tajima, K. Hirota, and K. Hashimoto. Synthesis of all-conjugated diblock copolymers by quasi-living polymerization and observation of their microphase separation. *J. Am. Chem. Soc*, 130(25):7812–7813, 2008.

[109] H. Xin, O.G. Reid, G. Ren, F.S. Kim, D.S. Ginger, and S.A. Jenekhe. Polymer Nanowire/Fullerene Bulk Heterojunction Solar Cells: How Nanostructure Determines Photovoltaic Properties. *ACS nano*, 4(4):1861–1872, 2010.

[110] M. W. Matsen and M. Schick. Stable and unstable phases of a diblock copolymer melt. *Phys. Rev. Lett.*, 72(16):2660–2663, 1994.

[111] E. L. Thomas, D. M. Anderson, C. S. Henkee, and D. Hoffman. Periodic area-minimizing surfaces in block copolymers. *Nature*, 334:598–601, 1988.

[112] T. H. Epps, E. W. Cochran, T. S. Bailey, R. S. Waletzko, C. M. Hardy, and F. S. Bates. Ordered network phases in linear poly(isoprene-b-styrene-b-ethylene oxide) triblock copolymers. *Macromolecules*, 37:8325–8341, 2004.

[113] S.S. Sun. Design of a block copolymer solar cell. *Solar energy materials and solar cells*, 79(2):257–264, 2003.

[114] S. Sun, Z. Fan, Y. Wang, and J. Haliburton. Organic solar cell optimizations. *Journal of Materials Science*, 40(6):1429–1443, 2005.

[115] A.J. Campbell, D.D.C. Bradley, and H. Antoniadis. Dispersive electron transport in an electroluminescent polyfluorene copolymer measured by the current integration time-of-flight method. *Applied Physics Letters*, 79:2133, 2001.

[116] R.U.A. Khan, C. Hunziker, and P. Günter. Perspectives on organic light-emitting diodes for display applications. *Journal of Materials Science: Materials in Electronics*, 17(6):467–474, 2006.

[117] RUA Khan, D. Poplavskyy, T. Kreouzis, and DDC Bradley. Hole mobility within arylamine-containing polyfluorene copolymers: A time-of-flight transient-photocurrent study. *Physical Review B*, 75(3):35215, 2007.

[118] RA Marsh, CR McNeill, A. Abrusci, AR Campbell, and R.H. Friend. A unified description of current-voltage characteristics in organic and hybrid photovoltaics under low light intensity. *Nano letters*, 8(5):1393–1398, 2008.

[119] H. Hoppe, N. Arnold, D. Meissner, and NS Sariciftci. Modeling of optical absorption in conjugated polymer/fullerene bulk-heterojunction plastic solar cells. *Thin Solid Films*, 451:589–592, 2004.

[120] J.K.J. van Duren, X. Yang, J. Loos, C.W.T. Bulle-Lieuwma, A.B. Sieval, J.C. Hummelen, and R.A.J. Janssen. Relating the morphology of poly (p-phenylene vinylene)/methanofullerene blends to solar-cell performance. *Advanced Functional Materials*, 14(5):425–434, 2004.

[121] W. Ma, C. Yang, X. Gong, K. Lee, and A.J. Heeger. Thermally stable, efficient polymer solar cells with nanoscale control of the interpenetrating network morphology. *Advanced Functional Materials*, 15(10):1617–1622, 2005.

[122] Y. Huang, S. Westenhoff, I. Avilov, P. Sreearunothai, J.M. Hodgkiss, C. Deleener, R.H. Friend, and D. Beljonne. Electronic structures of interfacial states formed at polymeric semiconductor heterojunctions. *Nature Materials*, 7(6):483–489, 2008.

[123] T. Kietzke, D. Neher, M. Kumke, O. Ghazy, U. Ziener, and K. Landfester. Phase separation of binary blends in polymer nanoparticles. *Small*, 3(6):1041–1048, 2007.

[124] C.R. McNeill, B. Watts, L. Thomsen, H. Ade, N.C. Greenham, and P.C. Dastoor. X-ray microscopy of photovoltaic polyfluorene blends: relating nanomorphology to device performance. *Macromolecules*, 40(9):3263–3270, 2007.

[125] B.A. Gregg. Excitonic solar cells. *J. Phys. Chem. B*, 107(20):4688–4698, 2003.

[126] A.J. Chatten, S.M. Tuladhar, S.A. Choulis, D.D.C. Bradley, and J. Nelson. Monte Carlo modelling of hole transport in MDMO-PPV: PCBM blends. *Journal of Materials Science*, 40(6):1393–1398, 2005.

[127] LB Schein, A. Peled, and D. Glatz. The electric field dependence of the mobility in molecularly doped polymers. *Journal of Applied Physics*, 66(2):686–692, 1989.

[128] SV Novikov and AV Vannikov. Dipole-trap model and non-dispersive charge-carrier transport in polymers of various structures. *Journal of Physics: Condensed Matter*, 6:10519, 1994.

[129] C. Tonezer and J.A. Freire. The role of short-ranged energetic correlations in the mobility field dependence of disordered organic materials. *The Journal of Chemical Physics*, 128:014703, 2008.

[130] J.K. Grey, D.Y. Kim, C.L. Donley, W.L. Miller, J.S. Kim, C. Silva, R.H. Friend, and P.F. Barbara. Effect of Temperature and Chain Length on the Bimodal Emission Properties of Single Polyfluorene Copolymer Molecules. *J. Phys. Chem. B*, 110(38):18898–18903, 2006.

[131] T. Kreouzis, D. Poplavskyy, SM Tuladhar, M. Campoy-Quiles, J. Nelson, AJ Campbell, and DDC Bradley. Temperature and field dependence of hole mobility in poly (9, 9-dioctylfluorene). *Physical Review B*, 73(23):235201, 2006.

[132] C. Tanase, EJ Meijer, PWM Blom, and DM De Leeuw. Unification of the hole transport in polymeric field-effect transistors and light-emitting diodes. *Physical review letters*, 91(21):216601, 2003.

[133] A.J. Mozer and N.S. Sariciftci. Negative electric field dependence of charge carrier drift mobility in conjugated, semiconducting polymers. *Chemical physics letters*, 389(4-6):438–442, 2004.

[134] WF Pasveer, J. Cottaar, C. Tanase, R. Coehoorn, PA Bobbert, PWM Blom, DM De Leeuw, and MAJ Michels. Unified description of charge-carrier mobilities in disordered semiconducting polymers. *Physical review letters*, 94(20):206601, 2005.

[135] G.E.P. Box and M.E. Muller. A note on the generation of random normal deviates. *The Annals of Mathematical Statistics*, 29(2):610–611, 1958.

[136] SV Novikov, DH Dunlap, VM Kenkre, PE Parris, and AV Vannikov. Essential role of correlations in governing charge transport in disordered organic materials. *Physical Review Letters*, 81(20):4472–4475, 1998.

[137] D. H. Dunlap, P. E. Parris, and V. M. Kenkre. Charge-dipole model for the universal field dependence of mobilities in molecularly doped polymers. *Phys. Rev. Lett.*, 77(3):542–545, 1996.

[138] LG Kaake, PF Barbara, and X.Y. Zhu. Intrinsic Charge Trapping in Organic and Polymeric Semiconductors: A Physical Chemistry Perspective. *The Journal of Physical Chemistry Letters*, 1:628–635, 2010.

[139] F.C. Spano. Modeling disorder in polymer aggregates: The optical spectroscopy of regioregular poly (3-hexylthiophene) thin films. *The Journal of chemical physics*, 122:234701, 2005.

[140] F.C. Spano, S.C.J. Meskers, E. Hennebicq, and D. Beljonne. Probing excitation delocalization in supramolecular chiral stacks by means of circularly polarized light: experiment and modeling. *Journal of the American Chemical Society*, 129(22):7044–7054, 2007.

[141] RJ De Vries, SLM Van Mensfoort, V. Shabro, SIE Vulto, RAJ Janssen, and R. Coehoorn. Analysis of hole transport in a polyfluorene-based copolymerevidence for the absence of correlated disorder. *Applied Physics Letters*, 94(16):163307, 2009.

[142] J.M. Montero and J. Bisquert. Trap origin of field-dependent mobility of the carrier transport in organic layers. *Solid-State Electronics*, 2010.

[143] R. Steyrleuthner, S. Bange, and D. Neher. Reliable electron-only devices and electron transport in n-type polymers. *Journal of Applied Physics*, 105(6):064509, 2009.

[144] R. Steyrleuthner, M. Schubert, F. Jaiser, J.C. Blakesley, Z. Chen, A. Facchetti, and D. Neher. Bulk Electron Transport and Charge Injection in a High Mobility n-Type Semiconducting Polymer. *Advanced Materials*, 22(25):2799–2803, 2010.

[145] P. Mark and W. Helfrich. Space-Charge-Limited Currents in Organic Crystals. *Journal of Applied Physics*, 33(1):205–215, 1962.

[146] VI Arkhipov, U. Wolf, and H. Bässler. Current injection from a metal to a disordered hopping system. II. Comparison between analytic theory and simulation. *Physical Review B*, 59(11):7514–7520, 1999.

[147] M. Vissenberg and M. Matters. Theory of the field-effect mobility in amorphous organic transistors. *Physical Review B*, 57(20):12964–12967, 1998.

[148] II Fishchuk, D. Hertel, H. Bässler, and AK Kadashchuk. Effective-medium theory of hopping charge-carrier transport in weakly disordered organic solids. *Physical Review B*, 65(12):125201, 2002.

[149] J. Zhou, YC Zhou, JM Zhao, CQ Wu, XM Ding, and XY Hou. Carrier density dependence of mobility in organic solids: A Monte Carlo simulation. *Physical Review B*, 75(15):153201, 2007.

[150] S G Stevenson, I D W Samuel, S V Staton, K A Knights, P L Burn, J H T Williams, and Alison B Walker. Current-voltage characteristics of dendrimer light-emitting diodes. *Journal of Physics D: Applied Physics*, 43(38):385106, 2010.

[151] L.A.A. Pettersson, L.S. Roman, and O. Inganäs. Modeling photocurrent action spectra of photovoltaic devices based on organic thin films. *Journal of Applied Physics*, 86:487, 1999.

[152] R. Shikler and R.H. Friend. Modeling the effect of the structure of polymer photocells on their absorption spectrum. *Journal of Applied Physics*, 102:013105, 2007.

[153] E. Hecht. *Optics, 4th edition.* Addison Wesley, San Francisco, 2001.

[154] J. H. T. Williams. *Finite Element Simulations Of Excitonic Solar Cells And Organic Light Emitting Diodes.* PhD thesis, University of Bath, 2008.

[155] H. Hoppe, NS Sariciftci, and D. Meissner. Optical constants of conjugated polymer/fullerene based bulk-heterojunction organic solar cells. *Molecular Crystals and Liquid Crystals*, 385(1):113–119, 2002.

[156] CM Ramsdale and NC Greenham. The optical constants of emitter and electrode materials in polymer light-emitting diodes. *Journal of Physics D: Applied Physics*, 36(4):29–34, 2003.

[157] S. Westenhoff, I.A. Howard, J.M. Hodgkiss, K.R. Kirov, H.A. Bronstein, C.K. Williams, N.C. Greenham, and R.H. Friend. Charge recombination in organic photovoltaic devices with high open-circuit voltages. *Journal of the American Chemical Society*, 130(41):13653–13658, 2008.